Thermal inertia and surface heterogeneity on Mars

by

Nathaniel E. Putzig

Bachelor of Science

Geophysical Engineering, Colorado School of Mines, 1986

Master of Arts

Geophysics, Rice University, 1988

A dissertation submitted to the

Faculty of the Graduate School of the

University of Colorado in partial fulfillment

of the requirements for the degree of

Doctor of Philosophy

Geophysics Program

Department of Geological Sciences

2006

This dissertation entitled:
Thermal inertia and surface heterogeneity on Mars
written by Nathaniel E. Putzig
has been approved for the Geophysics Program
Department of Geological Sciences

_____

Dr. Michael T. Mellon

_____

Dr. Bruce M. Jakosky

_____

Dr. Larry W. Esposito

_____

Dr. Brian M. Hynek

_____

Dr. Joshua E. Colwell

Date _____

The final copy of this dissertation has been examined by the signatories, and we find that both the content and the form meet acceptable presentation standards of scholarly work in the above mentioned discipline.

Putzig, Nathaniel E. (Ph.D., Geophysics)

Thermal inertia and surface heterogeneity on Mars

Dissertation directed by Dr. Michael T. Mellon

Abstract

Thermal inertia derived from temperature observations is critical for understanding surface geology and assessing potential landing sites on Mars. Derivation methods generally assume uniform surface properties for any given observation. Consequently, horizontal heterogeneity and near-surface layering may yield apparent thermal inertia that varies with time of day and season. To evaluate the effects of horizontal heterogeneity, I modeled the thermal behavior of surfaces containing idealized material mixtures (dust, sand, duricrust, and rocks) and differing slope facets. These surfaces exhibit diurnal and seasonal variability in apparent thermal inertia of several 100 tiu,[1] even for components with moderately contrasting thermal properties. To isolate surface effects on the derived thermal inertia of Mars, I mapped inter-annual and seasonal changes in albedo and atmospheric dust opacity, accounting for their effects in a modified derivation algorithm. Global analysis of three Mars years of MGS-TES[2] data reveals diurnal and seasonal variations of $\sim$200 tiu in the mid-latitudes and 600 tiu or greater in the polar regions. Correlation of TES results and modeled apparent thermal inertia of heterogeneous surfaces indicates pervasive surface heterogeneity on Mars. At TES resolution, the near-surface thermal response is broadly dominated by layering and is consistent with the presence of duricrusts over fines in the mid-latitudes and dry soils over ground ice in the polar regions. Horizontal surface mixtures also play a role and may dominate at higher resolution. In general, thermal inertia obtained from single observations or annually averaged maps may misrepresent surface properties. In lieu of a robust heterogeneous-surface derivation technique, repeat coverage can be used together with forward-modeling results to constrain the near-surface heterogeneity of Mars.

---

[1] tiu $\equiv \mathrm{J\,m^{-2}\,K^{-1}\,s^{-\frac{1}{2}}}$

[2] Mars Global Surveyor Thermal Emission Spectrometer

For two exceptional teachers:

Frances

to whom I, with diplomas drying, exclaimed,
"Mom, I still don't know what I want to be when I grow up!"
to which she, with retirement looming, replied,
"Well, Than, neither do I."

Mary

who, many years ago, declared,
"I see you getting your doctorate one day,"
to which I responded,
"Grandma, I am *so* done with graduate school."

Acknowledgments

First and foremost, I wish to express my appreciation to Mike Mellon, my research advisor and co-author of the three central chapters. His depth of knowledge, attention to detail, and superior mentoring have been invaluable. Bruce Jakosky has been a constant source of expert knowledge and his academic advice always well-considered and sound. Brian Hynek has been a font of practical skills and advice, a willing sounding board, and a good friend. Other committee members and instructors who have offered unfailing, insightful advice include Larry Esposito, Josh Colwell, Bob Pappalardo, Steve Mojzsis, and Fran Bagenal. Critical elements of these studies were provided by Katherine Kretke, Ray Arvidson, Matt Golombek, Shannon Pelkey, Ashwin Vasavada, Sara Martínez-Alonso, and Nate Murphy. For helpful discussions, manuscript reviews, and general moral support, I am indebted to Matt Golombek, Marsha Presley, Hanna Sizemore, Ben Brown, Jen Heldmann, Shawn Brooks, Amy Barr, Brennan Gantner, Licia Ray, and Matt Chojnacki. Many other close friends have helped me along the way, including Mike Riehle, Tom Botts, Fritz Foss, and Doug Paul, who provided glowing recommendations which landed me back in graduate school. A very warm thanks goes out to my family, who have been staunchly supportive over the years and remarkably tolerant of my expressions of abundant enthusiasm for this field of study. Finally, I am extremely grateful to the U.S. taxpayers, who funded this research through NASA's Mars Data Analysis Program.

Contents

Chapter

Tables

Table

Figures

Figure

Chapter 1

Introduction

> Heat penetrates, like gravity, all the substances of the universe, its rays occupy all the parts of space. The goal of our work is to expose the mathematical laws which this element follows.
>
> — Jean Baptiste Joseph Fourier, 1822

It is the very complexity of the universe in which we find ourselves that drives us to explore it. The heterogeneous nature of our surroundings is at once a source of fascination and a great challenge to our understanding. It is thus rather ironic that our ability to expose the mathematical laws which describe that complexity are rooted in the concept of homogeneity.

Isaac Newton is frequently credited for founding the field of heat transfer with his 'Law of Cooling', which states that the rate of cooling q of a body is proportional to the temperature difference ΔT between the body and its surroundings:

$$q \propto \Delta T \,. \tag{1.1}$$

But as Adiutori (2005) points out in an argument for the primacy of Fourier's contributions, neither Newton, his contemporaries, nor their predecessors ever attributed anything resembling our modern concept of dimensionality to the properties represented in this or the other physical laws which they discovered. It wasn't until over 100 years later, when Fourier (1822) parameterized the "constants" of proportionality through his introduction of the concept of dimensional homogeneity, that such physical laws were transformed into true mathematical equations

as we know them today. The missing element in Eq. 1.1 that was introduced by Fourier is the coefficient of heat transfer, h:

$$q = h\,\Delta T\,. \tag{1.2}$$

In hindsight, this substitution of a parameter for a nebulous constant of proportionality may seem almost trivial, but in Fourier's day, it was revolutionary. Previously, performing mathematical operations on dimensional properties such as heat or temperature was anathema. As Adiutori (2005) puts it:

> Galileo's view of homogeneity is reflected in the following:
>
> > If two particles are carried at a uniform rate, the ratio of their speeds will be the product of the ratio of the distances traversed by the inverse ratio of the time-intervals occupied.
>
> In Galileo's view, distance and time are necessary to quantify speed, but speed has nothing to do with dividing distance by time. Galileo divided distance by distance and time by time, but he would not divide distance by time. In his view, and in the view of his colleagues, dividing distance by time was irrational.

In Fourier's view, an equation such as 1.2 is only valid when each term has the same dimensionality. Over the objections of history and his fellows, he divided heat flux by a change in temperature and declared it be the parameter h, with the value and dimensions of $q/\Delta T$ (Adiutori 2005). With a stroke, a bridge is built between science and mathematics, and the quantitative analysis of natural laws becomes drastically more tractable; 100 years later, we're taking the temperature of Mars (Pettit and Nicholson 1924, Coblentz and Lampland 1924).

1.1 Radiance, temperature, and thermal inertia

Radiometric observations aimed at taking the temperature of a remote celestial object actually measure its radiance.[1] One may obtain a temperature estimate

[1] Radiance is power per solid angle per projected source area.

from the radiance R using the Stefan–Boltzmann Law and assuming that the body is a perfect radiator, or black body:[2]

$$\pi\, R = \sigma\, {T_{\rm B}}^4\,, \tag{1.3}$$

where σ is the Stefan–Boltzmann constant and $T_{\rm B}$ is the brightness[3] temperature. For an imperfect emitter, or 'gray' body, the right-hand term may be multiplied by the fractional emissivity ϵ.

If the ultimate goal is to characterize the surface materials of the object, a thermal model of its atmosphere (if it has one) and shallow subsurface will allow the determination of the surface kinetic[4] temperature and physical properties such as thermal inertia. Given no prior knowledge, one may proceed with the basic assumption that the subsurface materials are isotropic and homogeneous. In this case, their temperature T at time t and depth Z is governed by the heat conduction equation:[5]

$$\frac{\partial T}{\partial t} = \frac{k}{\rho\, c}\, \frac{\partial^2 T}{\partial Z^2}\,, \tag{1.4}$$

where the material properties of thermal conductivity k, density ρ, and specific heat capacity c are constants. Fourier (1822) derived this equation and a means of solving it by the use of boundary conditions and the representation of temperature as an infinite series of trigonometric functions.

In an effort to explain lunar temperature observations, Wesselink (1948) demonstrated the application of the heat equation to planetary surfaces, where heat flux at the surface provides one boundary condition and the presumption of no heat flow horizontally or at great depths provides the others. Thus, heat

[2] A black body absorbs all incident radiation and emits radiation at wavelengths dependent upon its temperature as given by the Planck function (Rybicki and Lightman 1979).

[3] In this context, "brightness" is a misnomer for "radiance" (U.S. Dept. of Commerce 1996), but the term "brightness temperature" is still widely used in the atmospheric and space sciences.

[4] Kinetic temperature is independent of wavelength whereas brightness temperature and radiance may vary with wavelength for non-unit emissivity.

[5] Equation 1.4 is also known as the thermal diffusion equation.

radiating to space from a surface at temperature T_S is balanced by the sum of incident solar radiation and subsurface conduction:

$$\epsilon \sigma {T_S}^4 = S\,(1 - A)\,\cos i + k \left.\frac{\partial T}{\partial Z}\right|_{Z=0}, \tag{1.5}$$

where S is the solar insolation at the planet's orbit, A is the surface albedo, and i is the solar incidence angle. For planets with atmospheres, additional terms such as downwelling atmospheric radiation and the latent heat of volatile condensation may be included. Given the periodic nature of insolation for rotating bodies, subsurface heat flow is also periodic and generally diminishes rapidly with depth. Thus, it is convenient to introduce the concept of a thermal skin depth δ for insolation of period P (cf. Wesselink 1948, Turcotte and Schubert 2002):

$$\delta^2 = \frac{k}{\rho\, c}\,\frac{P}{\pi}\,. \tag{1.6}$$

At $Z = \delta$, the amplitude of the heat wave relative to that at the surface is reduced by a factor of e^{-1} and its phase is delayed by 1 radian (57.3 °). If one then normalizes the depth dimension as $Z' = Z/\delta$, Eq. 1.5 becomes

$$\epsilon \sigma {T_S}^4 = S\,(1 - A)\,\cos i + \sqrt{\frac{k\,\rho\,c\,\pi}{P}}\left.\frac{\partial T}{\partial Z'}\right|_{Z'=0}. \tag{1.7}$$

The normalization to thermal skin depth isolates the surface material properties, and it is this combination of conductivity, density, and heat capacity which defines thermal inertia:

$$I \equiv \sqrt{k\,\rho\,c}\,. \tag{1.8}$$

From Eqs. 1.7 and 1.8, it is clear that thermal inertia is the key material property controlling the insolation-driven periodic variations of surface temperature. As Eq. 1.8 and its name implies, thermal inertia is a measure of a material's resistance to changes in temperature and of the rate at which that material conducts and stores heat. Given the scale of remote observations and the nature of

geologic materials, thermal inertia is generally treated as a bulk material property representing surfaces that may contain varying quantities of cemented or uncemented granular materials, rocks, or volatile condensates.

Laboratory studies of conductivity, density, and specific heat capacity under various conditions of temperature and pressure are an important part of understanding how each of these components may influence the derived thermal inertia of planetary surfaces. Presley and Christensen (1997a) presented a review of laboratory techniques in use throughout the latter half of the twentieth century, with a focus on conductivity measurements. Driven predominantly by the lunar exploration effort surrounding the Apollo program, early studies focused on materials of silicate composition under near-vacuum conditions. Based on prior studies of lunar temperature variations, the Moon's surface was believed to be dominated by low-density particulates or highly porous materials. Wechsler et al. (1972) provided a summary of relevant laboratory studies from this time period, some of which included conditions applicable to the martian environment (e.g., Fountain and West 1970). In general, specific heat capacity varies with composition in typical planetary surface temperature ranges by no more than a factor of 2–3. Density of geologic materials ranging from loosely packed powders to solid crystalline materials can vary by a factor of $\sim$2–6. In contrast, thermal conductivity of particulates has been found to vary with interstitial gas pressure, particle size, and pore geometry by several orders of magnitude. Thus, thermal inertia depends primarily on thermal conductivity, although, as will be discussed below and in Chapter 2, density may also play an important role.

Since granular materials are more or less ubiquitous on planetary surfaces, an understanding of the physics of heat transfer in particulates is critical to the interpretation of data derived from planetary radiance observations. Presley and Christensen (1997a) summarized theoretical and laboratory results for the effective

conductivity in particulates as determined in many previous studies (Schotte 1960, Woodside and Messmer 1961, Masamune and Smith 1963, Wechsler and Glaser 1965, Wechsler et al. 1972, and references therein). Heat flow in particulates occurs by a combination of conduction and radiation and is complicated by complex geometrical relationships between the particles and their pore spaces and by the generally large contrast between the thermal properties of the solid and interstitial portions of the matrix. Theoretical treatments generally employ simplifications such as assuming that heat flow is unidirectional and representing it as some combination of series and parallel paths. The approach taken varies, depending on the conditions being modeled and the level of detail desired (cf. Masamune and Smith 1963, Wechsler et al. 1972, Presley and Christensen 1997a, Mellon et al. 1997). A common technique is to model heat flow through a bed of fine particles and gas with three heat transfer mechanisms operating in parallel:

$$k = k_{\mathrm{g}} + k_{\mathrm{s}} + k_{\mathrm{r}} \,. \tag{1.9}$$

These mechanisms are conduction through the gas-filled pore spaces (k_{g}), conduction through solid paths only via particle contact areas (k_{s}), and thermal radiation within the particles, across the pore spaces between the particle surfaces, and between the pore spaces (k_{r}) (Wechsler et al. 1972; see Fig. 1.1). With this approach, the solid and radiative paths may be represented with series components (e.g., solid conduction through a particle, across a contact, and through the next particle). Note that each term as presented here may vary with the scale and geometry of the matrix and is generally not equivalent to the conductivity of a bulk sample of the gas or solid material alone. Other representations may break down series and parallel paths differently, such as focusing on the transfer of heat energy between two grains as a model of the bulk material (e.g., Mellon et al. 1997).

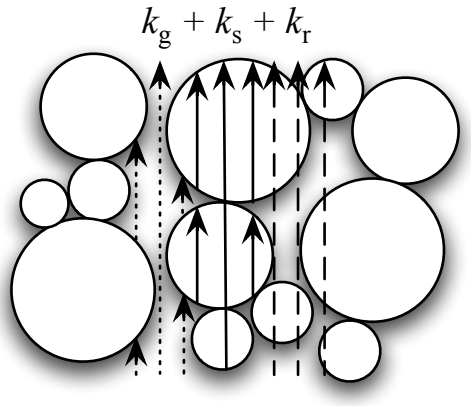

Figure 1.1 Typical simplified schematic model of conductivity in particulates. Heat flow is presumed to be unidirectional and components representing gas-path conduction (k_g; dotted lines), solid-path conduction (k_s; solid lines), and radiation (k_r; dashed lines) are treated as operating in parallel, with series sub-components.

In a vacuum, the bulk conductivity k_v is dominated by the solid-path and radiative terms, which may have material-specific temperature dependence and are commonly approximated as (e.g., Fountain and West 1970, Wechsler et al. 1972, Presley and Christensen 1997a):

$$k_v = k_s + k_r = C_{s_1} + C_{s_2}\,T + C_{s_3}/T + C_r\,T^3\,, \tag{1.10}$$

where the solid-conduction constants C_{s_i} depend on how particle contact area and conduction for a given material may vary with temperature, and the radiative-conduction constant C_r depends on the particle composition and geometric factors such as porosity, contact area, and particle surface characteristics.

In the presence of an atmosphere, the k_g term becomes important. The contribution to bulk conductivity by the gas is directly proportional to its mean free path within the pore spaces and inversely proportional to its density (Presley and Christensen 1997a). At very low pressures ($<\sim 0.01$ mbar), the solid-path and radiative terms continue to dominate and the effective conductivity is relatively independent of pressure and particle size (Masamune and Smith 1963; see

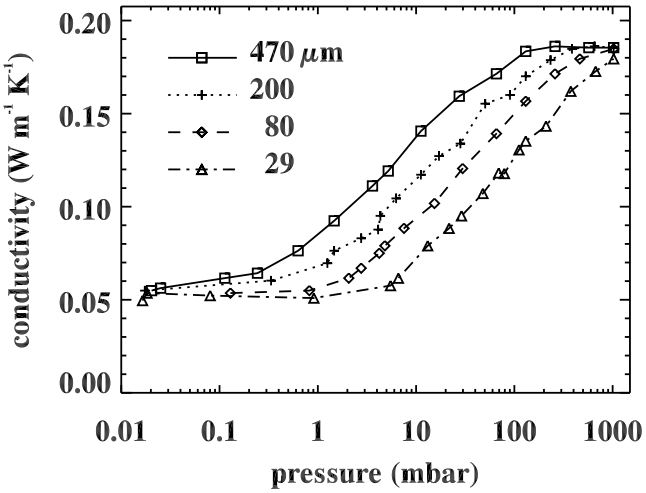

Figure 1.2 Conductivity as a function of pressure. Laboratory data are from Masamune and Smith (1963) for beds of glass beads at four different diameters. Note the increase of conductivity with particle size at intermediate pressures.

Fig. 1.2) . Because the inherent conductivity of the particles is much higher than that of the gas, heat will build up around the particle contacts, the size of which is dependent on the particle size (Woodside and Messmer 1961, Presley and Christensen 1997a). Consequently, most of the heat-transfer in the gas will occur near the contacts and thereby establish an effective heat transfer path for the gas which is directly related to the particle size and porosity. As gas pressure increases, its density increases, but the effective heat-transfer path length will remain constant as long as the mean free path is longer. Thus, the conductivity in the gas increases with its density, and the effective conductivity along the gas path will increase with pressure and particle size in this pressure range, with gas conduction overwhelming the solid-path and radiative terms at pressures greater than ~ 0.1 mbar (Masamune and Smith 1963, Wechsler and Glaser 1965, Presley and Christensen 1997a,b; see Fig. 1.2). At much higher pressures ($> \sim 1$ bar) where the mean free path becomes much shorter than the effective heat transfer path, small changes in pressure cause offsetting changes in gas density and mean free path, and the effective conductivity is again relatively independent of pressure and particle size.

In the intermediate pressure range where gas conduction is dominant, the effects on conductivity of temperature and composition are relatively minor, but conductivity appears to increase with density (Fountain and West 1970, Wechsler et al. 1972). Presley and Christensen (1997c) found a near-linear relationship between density and conductivity for a broad range of pressures, attributing the effect to an increase in particle contact area and a reduction of effective heat-transfer path with increase in density. When this conductivity effect is combined with that of density itself, large changes in density may be expected to affect thermal inertia (Eq. 1.8; see also Chapter 2).

While most of the laboratory studies have focused on narrow ranges of particle size in any given sample, a few have considered particle mixtures (Woodside and Messmer 1961, Presley and Christensen 1997c, Presley and Craddock 2006). Woodside and Messmer (1961) found an increase in conductivity for a bimodal mixture over that of either constituent, but as Presley and Christensen (1997c) point out, there were large differences in density between their samples which may have contributed to the observed effect. In other examinations of mixtures using glass beads and natural samples, Presley and Christensen (1997c) and Presley and Craddock (2006) found that the conductivity of the mixtures was nearly identical to that of the larger particles alone, even for samples with relatively small fractions ($< \sim 10\%$) of the larger particle sizes. They suggested that heat conduction via the contact areas of the larger particles may be dominating, essentially bypassing the smaller particles that occupy their effective pore spaces.

With atmospheric pressures of 0.68–13.7 mbar, the martian surface is predominantly in the intermediate pressure range where the bulk conductivity of granular materials varies directly with pressure and particle size. Thus, thermal inertia may be expected to show a similar relationship, and it is often used to infer effective particle sizes on the surface of Mars, assuming granular materials (e.g.,

Kieffer et al. 1973, 1977, Christensen 1986b, Presley and Christensen 1997a), with some consideration warranted for pressure changes due to elevation (e.g., Bridges 1994).

1.2 Thermal inertia SI unit proposal

Historically, thermal inertia has been given in units of $\mathrm{cal\,cm^{-2}\,K^{-1}\,s^{-\frac{1}{2}}}$, 10^{-3} $\mathrm{cal\,cm^{-2}\,K^{-1}\,s^{-\frac{1}{2}}}$, and more recently in SI units of $\mathrm{J\,m^{-2}\,K^{-1}\,s^{-\frac{1}{2}}}$. Regardless of the base system, these units are typographically cumbersome and can be visually distracting. They are nearly always either abbreviated (e.g., as 'IU' by Presley and Christensen 1997b and 'SI Units' by Golombek et al. 2003), or, more commonly, given once and thereafter "assumed" and left off altogether (e.g., by Kieffer et al. 1977, Jakosky 1979, Palluconi and Kieffer 1981, Christensen 1986b, Hayashi et al. 1995, Mellon et al. 2000, and Putzig et al. 2005). Neither solution is ideal. In one case, we have a varying set of ad hoc units; in the other, bare numbers whose units are only ascertained upon a close examination of the early portions of the text. This situation suggests the introduction of a new standard derived SI unit. To that end, I hereby propose a new SI unit designation of 'tiu' such that:

$$\mathrm{tiu} \equiv \mathrm{J\,m^{-2}\,K^{-1}\,s^{-\frac{1}{2}}}\,. \tag{1.11}$$

While 'tiu' may be viewed as an acronym for 'thermal inertia units', it is also the name for Mars in Old English (e.g., Tiu Vallis) and incidentally serves as the root word for 'Tuesday' (Pickett et al. 2000). Naming this unit after Mars is appropriate because conditions on the surface of Mars are uniquely "tuned" to take greatest advantage of thermal inertia as a measure of surface physical properties (Wechsler et al. 1972, Jakosky 1986, Presley and Christensen 1997a). Furthermore, 'tiu' is terse enough to encourage its inclusion throughout a journal paper, yet unique

enough to avoid confusion with other units or English words. Henceforward, I will employ this provisional new unit, and I encourage its adoption by others.

1.3 Previous thermal inertia results

Sinton and Strong (1960) found significant diurnal temperature variations in telescopic scans of martian brightness temperature, but were unable to provide a satisfactory fit to the variations using fixed material properties that neglected the atmosphere. They obtained estimates of thermal inertia of 170 and 420 tiu, depending on whether they matched the phase or the amplitude of the temperature variations. A better fit to the same data was obtained by Leovy (1966) using a simplified atmospheric model based on Newton's law of cooling. He obtained much lower estimates of thermal inertia (63 and 100 tiu), which suggested that atmospheric effects are substantial. In another analysis of these observations, Morrison et al. (1969) chose an alternative model of the atmosphere, with a constant greenhouse back-radiation to the surface equal to 1% of the peak insolation, and they estimated thermal inertia at 210 tiu. This same assumption of constant downward radiative flux from the atmosphere was used by Neugebauer et al. (1971) in their analysis of brightness temperature observations from the flyby missions Mariner 6 and 7. They estimated a mean thermal inertia of 250 tiu for regions in Margaritifer Sinus, Meridiani Sinus, and Deucalionis Regio, and values of 375 and 420 tiu in Syrtis Major and Hellas, with areas of low albedo having higher thermal inertia. A similar atmospheric model was again employed for analyses of Mariner 9 (Kieffer et al. 1973) and Viking observations (Kieffer et al. 1977, Palluconi and Kieffer 1981), with the assumed back-radiation raised to 2% of the peak insolation. Kieffer et al. (1973) found thermal inertia in the range 170–710 tiu from Mariner 9 results. For Viking, Kieffer et al. (1977) derived thermal inertia of 67–460 tiu, expanding this range to 42–630 tiu with the addition of more data

(Palluconi and Kieffer 1981). These Viking studies found bimodal distributions of both thermal inertia and albedo which were anti-correlated (see also Fig. 2.4). Mismatches of temperature variations between the observed values and values modeled using fixed material properties were noted, with the largest differences occurring in the afternoon (the so-called "afternoon cooling" phenomenon).

The simplified atmospheric models used in these early studies did not include effects such as the attenuation of insolation, temporal variability of the downward radiative flux, convection, or sensible heat exchange with the surface. To assess the impact of including these factors, Haberle and Jakosky (1991) developed a thermal model which included both a subsurface model and a more rigorous treatment of the atmosphere. In their model, temporal changes in atmospheric temperature T_{A} are governed by changes in the upward net flux of total radiation F and sensible heat flux H with pressure p:

$$\frac{\partial T_{\mathrm{A}}}{\partial t} = \frac{g}{c_{\mathrm{p}}} \frac{\partial}{\partial p} (F + H) + CA \,, \tag{1.12}$$

where g is the acceleration of gravity, c_{p} is the specific heat of CO_2 at constant pressure, and CA is a temperature change due to convective adjustment when the lapse rate becomes unstable. The inclusion of these terms demonstrated that the atmospheric contribution on Mars is generally larger than had been previously thought. Consequently, the simpler models had led to estimates of thermal inertia which were substantially higher than the more complex model suggests. Haberle and Jakosky (1991) found that the atmospheric effects could account for about half of the anomalously low afternoon temperature values.

Hayashi et al. (1995) reanalyzed the Viking data, incorporating a dusty radiative-convective atmosphere, and produced values of thermal inertia generally about 25–70 tiu lower than those of Palluconi and Kieffer (1981), with larger differences at higher values (see Fig. 1.3) . A comparison of thermal inertia derived

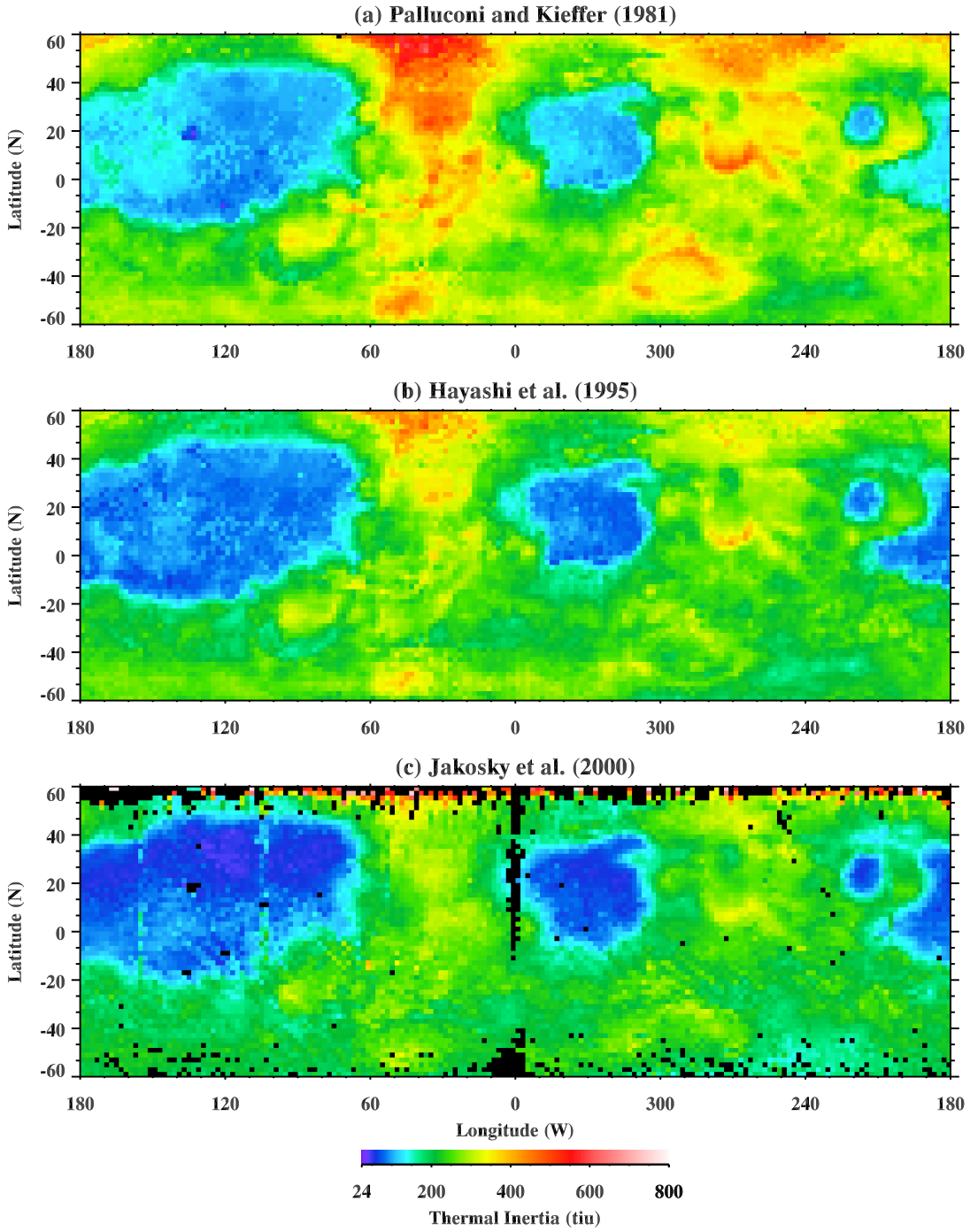

Figure 1.3 Maps of thermal inertia derived from Viking IRTM spectral brightness temperatures. (a) Palluconi and Kieffer (1981) fit observations from multiple times of day to temperatures from a model that assumed 2% back-radiation from the atmosphere. (b) Hayashi et al. (1995) also used a multi-point fitting algorithm, but incorporated a radiative-conductive atmosphere. (c) Jakosky et al. (2000) fit single observations of nighttime temperatures to model temperatures that also incorporated a radiative-conductive atmosphere. Compare also to TES results shown in Figs. 2.1 and 4.6.

from Viking data in the polar regions by Paige et al. (1994) and Paige and Keegan (1994) using the 2% assumption with that of a later reanalysis of the same data by Vasavada et al. (2000) that incorporated a radiative-convective atmospheric model shows similar differences. With each increase in the mapped resolution of thermal inertia from Viking (Christensen and Moore 1992) and from Mars Global Surveyor (MGS) Thermal Emission Spectrometer (TES) (Mellon et al. 2000; Chapters 2 and 4), the range of values has increased, and it presently stands at 5–5000 tiu, which is the full range of allowed values in the latest derivation algorithm (Chapter 4). However, a comparison of mapping results (cf. Figs. 1.3, 2.1, 4.6, and 4.8) shows that the mean thermal inertia has generally decreased as more sophisticated techniques have reduced or eliminated sources of error.

Estimates of thermal inertia are obtained from brightness temperature using numerical thermal models. Early work with telescopic observations matched diurnal curves by calculating temperature for limited ranges of albedo and thermal inertia (Wesselink 1948, Sinton and Strong 1960, Leovy 1966, Morrison et al. 1969, Neugebauer et al. 1971). With the advent of orbital spacecraft at Mars, data volume increased dramatically and more elaborate modeling techniques were developed which involved the production of lookup tables of modeled diurnal temperature for broader ranges of season, local time, latitude, albedo, and thermal inertia (Kieffer et al. 1973, 1977). For specific locations, temperature observations from different times of day were fit to modeled temperature curves by adjusting both albedo—to fit the mean diurnal temperature—and thermal inertia—to fit the amplitude of diurnal temperature variations. Later workers employed the same or similar techniques (Palluconi and Kieffer 1981, Paige et al. 1994, Paige and Keegan 1994, Hayashi et al. 1995, Vasavada et al. 2000), adding dust opacity as a parameter when more accurate atmospheric models were introduced. These multi-point curve-fitting techniques produced thermal-model albedo which was

noted to differ substantially from albedo derived independently from visible-band spectra.

With a fixed-local-time orbit and a spatial resolution of $\sim$3 km, MGS-TES has sparse diurnal sampling and infrequently repeated coverage of the surface. Thus, the multi-point technique is not appropriate for obtaining thermal inertia from TES observations, and a new single-point method was developed (Jakosky et al. 2000, Mellon et al. 2000). Greater accuracy for modeled temperature was needed, so finer increments were chosen for the subsurface and atmospheric models and for the lookup table, which was also expanded to include atmospheric surface pressure and dust opacity. Albedo is taken from visible bolometer observations and no thermal-model albedo is produced. As a result of these changes, apparent thermal inertia is calculated for each observation without the need for repeat coverage. Where there is repeat coverage, this new method has the additional advantage of allowing diurnal and seasonal variation in apparent thermal inertia, which may be indicative of heterogeneities in the near-surface (see Chapters 3 and 4). Upon development of this new single-point technique, Jakosky et al. (2000) recalculated thermal inertia from Viking nighttime observations and found values generally 0–60 tiu lower than those of Hayashi et al. (1995), with the exception of a few regions of low thermal inertia where some values are higher by 0–20 tiu (see Fig. 1.3).

An important distinction between methods of deriving thermal inertia is the use of spectral vs. bolometric temperature. Mellon et al. (2000) compared nighttime thermal inertia derived from TES spectral and bolometric temperature and found a close correspondence, with about a 10% relative reduction in the spectral results at higher values of thermal inertia. They attributed this reduction to low surface emissivity in locations with higher thermal inertia. However, surface heterogeneity may also play a role. For example, consider a surface containing a

mixture of rocks and fines, where each component has a different, fixed value of thermal inertia. The radiance of the components will combine in a manner which will deviate substantially from a Planck function, even if the components have unit emissivity (see Fig. 1.4a). The values of surface temperature for such a mixture as determined from observations in different, limited spectral bands (e.g., Viking IRTM 7- and 20-μm observations) will differ from each other and from broadband measurements (e.g., TES thermal bolometer observations). These differences will vary with the mixing ratio of the components, as shown in Fig. 1.4b. Apparent thermal inertia as derived from the effective temperature will also vary with the mixing ratio and with the spectral band employed (see Fig. 1.4c). Thus, the reduction of TES spectral thermal inertia—which was determined from a Viking-IRTM 20-μm-equivalent temperature—relative to TES bolometric thermal inertia may be an indication of surface heterogeneity.

Christensen (1986b) exploited the temperature difference in the IRTM 7- and 20-μm bands to estimate and map rock abundance on Mars. The relationship between heterogeneity and thermal inertia can also be exploited to relate surface properties observed by landed spacecraft to remote-sensing observations. Similarly to the preceding example, Golombek et al. (2003) used the numerical thermal model of Mellon et al. (2000) to generate 20-μm temperature and derived apparent thermal inertia for mixtures of rocks and fines. They presented a figure (Golombek et al. 2003, Fig. 16) of bulk thermal inertia as a function of rock abundance. Using the rock abundance observed at a landing site and the apparent thermal inertia derived from remote observations, one may estimate the fine-component thermal inertia for that site using this relationship. The figure of Golombek et al. (2003) is applicable to thermal inertia derived from 20-μm spectral temperature; a complementary relationship for use with bolometric data is provided in Fig. 3.13

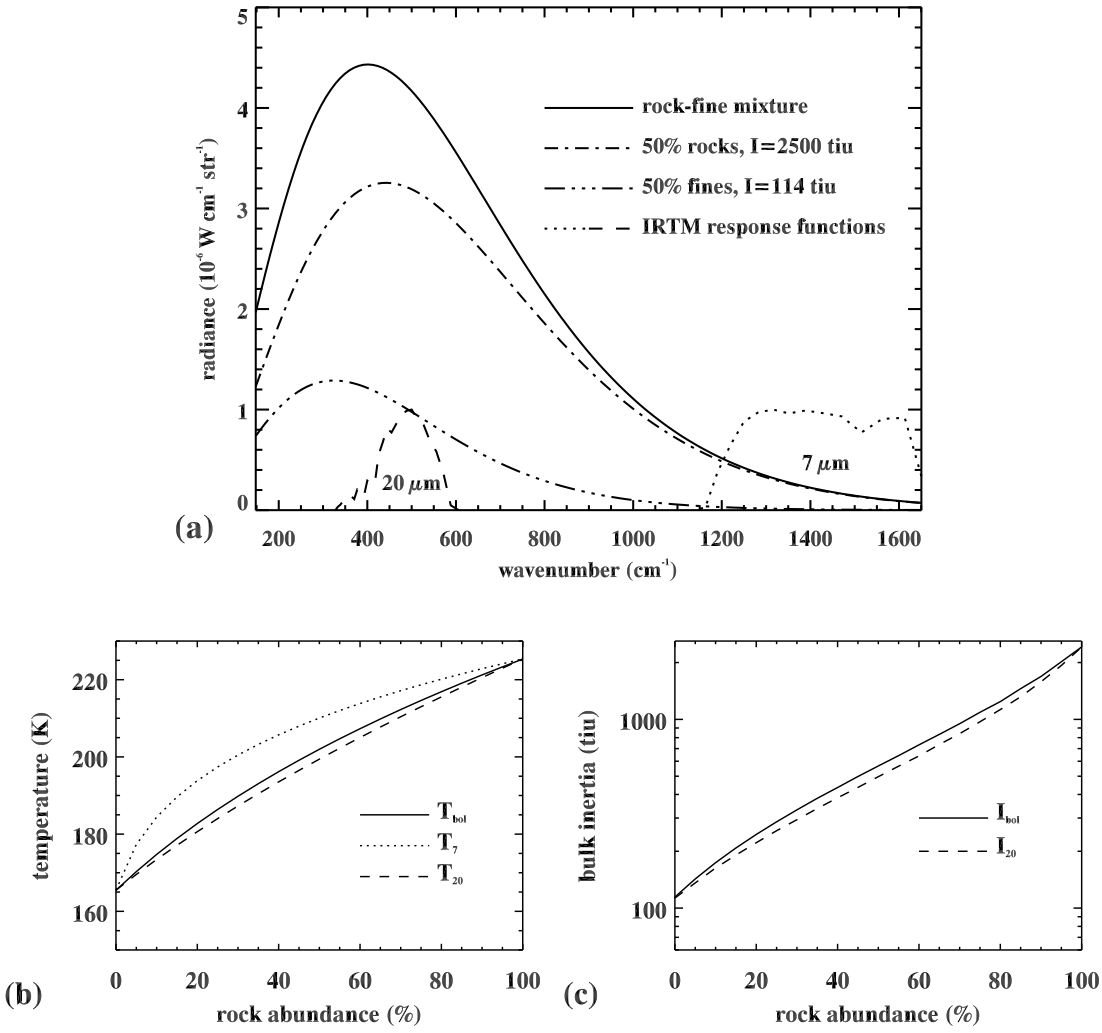

Figure 1.4 Model results for mixtures of rock and fine materials represented by fixed values of thermal inertia ($I_{\rm rock}$ = 2500 tiu, $I_{\rm fine}$ = 114 tiu) and albedo ($A_{\rm rock}$ = 0.10, $A_{\rm fine}$ = 0.25). Models are run at 05:00 local time, 10 °N, $L_{\rm S}$=127, and 6 mbar, with a visible dust opacity of 0.2. (a) Model radiances for a 50:50 mixture and Planck functions for each component. Response functions for the Viking IRTM 7- and 20-μm bands are scaled to 1. Note the deviation from Planck behavior of the mixture and the relative amplitudes of each component in the IRTM bands. (b) Surface temperatures for mixtures from pure rock (left) to pure fines (right) as computed bolometrically (solid curve) and using the IRTM response functions. The IRTM T_7–T_{20} contrast was used by Christensen (1986b) to map rock abundance. (c) Apparent thermal inertia for rock–fine mixtures derived from bolometric temperatures (solid curve) and from T_{20} temperatures (dashed curve) using the method presented in Chapter 4.

1.4 Summary of subsequent chapters

Chapter 2 was published previously under the title "Global thermal inertia and surface properties of Mars from the MGS mapping mission" (Putzig et al. 2005). In this work, we summarize the TES thermal inertia derivation procedures as developed by Mellon et al. (2000) and present a global map of thermal inertia at $\frac{1}{20}^\circ$ resolution, which includes observations taken throughout the primary MGS mission. The results are analyzed in similar fashion to that of previous workers, with emphasis on comparing thermal inertia to albedo and elevation. Surface unit maps for these cross-comparisons include the delineation of minor units not previously mapped. A noteworthy minor unit of low albedo and low thermal inertia that surrounds the south polar region is consistent with the presence of a low density surface mantle (Paige and Keegan 1994, Vasavada et al. 2000, Mustard et al. 2001), which is likely to be the product of desiccation at the top of an ice-rich subsurface (Mellon and Jakosky 1995, Boynton et al. 2002, Mellon et al. 2004). An analysis of the thermal inertia and surface units at the Viking and Pathfinder landing sites in context with observations from the surface is included.

In Chapter 3, which has been submitted for publication under the title "Thermal behavior of horizontally mixed surfaces on Mars" (Putzig and Mellon 2006a), I describe our technique for obtaining apparent thermal inertia from modeled horizontal mixtures of materials or sloped surfaces by performing an area-weighted linear mix of the Stefan–Boltzmann function (Eq. 1.3). We use modeled effective temperature to derive apparent thermal inertia with the same algorithm that is used for processing TES observations in Chapter 4. To characterize the effects of mixed surfaces on diurnal and seasonal variations in apparent thermal inertia, we examined a suite of mixtures representing dust, sand, duricrust, rocks, and various slope facets. TES local times (02:00 and 14:00; local times given

throughout in Mars hours and minutes, with 24:00 per sol, or Mars day) are used to illustrate the seasonal effects. To complement a graphical representation of the relationship between rock abundance and spectral thermal inertia which was presented by Golombek et al. (2003), we provide a similar figure for bolometric thermal inertia, extended to 100% rock abundance.

Chapter 4 has been submitted for publication as "Apparent thermal inertia and the surface heterogeneity of Mars" (Putzig and Mellon 2006b) and begins with a description of enhancements we made to the thermal model and lookup-table interpolation algorithm of Mellon et al. (2000). The changes allow broader ranges of thermal inertia and pressure and the incorporation of time-variant opacity measurements, an approximate correction for slope effects, and higher-resolution elevation and annual albedo maps. We processed three Mars years of TES observations with the enhanced algorithm and mapped apparent thermal inertia every 10° of L_S for both 02:00 and 14:00 local-time observations. From these seasonal maps, we produced global median nightside and dayside maps to 87° latitude in each hemisphere. The mapping results show large, systematic seasonal and diurnal variations in apparent thermal inertia. Modeling of simple two-component heterogeneous surfaces was undertaken at 10° intervals of latitude using materials representative of dust, sand, duricrust, and rocks and for a range of slopes. We compare the TES seasonal maps and heterogeneity modeling results at past lander sites and other areas of interest. To identify and map best-fitting horizontally mixed and layered material models, we developed a customized simultaneous curve-matching algorithm, yielding new maps of Mars surface heterogeneity at 5° resolution.

In Chapter 5, I provide a synthesis of the major conclusions reached in the preceding chapters and discuss their broader implications for the Mars exploration effort. The time-variable nature of the apparent thermal inertia results presented

in Chapter 4 suggests new opportunities and challenges for interpretation. While the constraints on the MGS mission fortuitously led to the development of a single-point derivation method, which in turn facilitated our analysis of diurnal and seasonal thermal inertia variations, the restriction to two local times limits the ability to fully characterize the diurnal variations. Future missions carrying thermal-band spectrometers should consider finer diurnal sampling. Although computational resources have thus far made it impractical to incorporate heterogeneity into an interpolation algorithm, such features have already been implemented in thermal models. With computational capabilities inexorably expanding, the derivation of global thermal inertia using multi-layered and horizontally mixed surface models may soon be carried out. Such a development promises to dramatically improve our understanding of Mars.

Chapter 2

Nighttime thermal inertia and surface properties of Mars

> To know that we know what we know, and to know that we do not know what we do not know, that is true knowledge.
>
> — Nicolaus Copernicus

2.1 Introduction

Thermal inertia is the key property controlling diurnal temperature variations at the surface of Mars. It depends on particle size, degree of induration, rock abundance, and exposure of bedrock within the top few centimeters of the subsurface (i.e., the thermal skin depth) and provides a measure of the subsurface's ability to store heat during the day and to re-radiate it during the night. Thermal inertia I is defined as the combination of bulk thermal conductivity k, bulk density ρ, and specific heat capacity c of the surface layer, such that

$$I \equiv \sqrt{k\,\rho\,c}\,. \tag{2.1}$$

The thermal skin depth δ is the e-folding depth of the subsurface thermal wave of period P given by

$$\delta \equiv \sqrt{\frac{k}{\rho\,c}\frac{P}{\pi}} = \frac{I}{\rho\,c}\sqrt{\frac{P}{\pi}}\,. \tag{2.2}$$

For granular materials under Mars surface conditions, the bulk conductivity dominates the thermal inertia and is driven by the conductivity of the gas in pore spaces (Wechsler et al. 1972, Jakosky 1986). Another important consideration is

that bulk conductivity also depends on bulk density (Fountain and West 1970, Presley and Christensen 1997c) and thus a large change in bulk density (i.e., porosity) may cause a significant change in thermal inertia. Laboratory data on the conductivity of 11–900 μm fines (Wechsler and Glaser 1965, Presley and Christensen 1997b) indicate that conductivity varies directly with grain size under Mars surface conditions, though the behavior outside this size range is uncertain (cf. Jakosky 1986, Presley and Christensen 1997b). Thus, thermal inertia is often used to estimate effective grain sizes (e.g., Kieffer et al. 1973, 1977, Christensen 1986b, Presley and Christensen 1997b). For material of a given particle size, conductivity may be increased by physically bonding the grains (Kieffer 1976). Such bonding was observed to form a 'case-hardened' crust (duricrust) at the Viking and Pathfinder landing sites (Binder et al. 1977, Mutch et al. 1977, Moore et al. 1999), and an analysis of radar, radio, and thermal remote-sensing data by Jakosky and Christensen (1986) suggested the presence of a near-global layer of duricrust with a variable degree of induration.

In general, unconsolidated fines (i.e., dust) will have low values of thermal inertia, indurated fines and sand-sized particles will have intermediate values, and rocks and exposed bedrock will have high values. In the context of spacecraft observations, the thermal inertia of any given location on the martian surface is controlled by a variable mixture of such materials on the scale of an observational footprint. By considering thermal inertia together with other observed surface properties, insight can be gained into the physical characteristics of the surface and the geological processes which have affected that surface.

Maps of thermal inertia derived from Viking Infrared Thermal Mapper (IRTM) data provided global coverage of Mars at 1° to 2° per pixel resolution (Kieffer et al. 1977, Palluconi and Kieffer 1981, Paige et al. 1994, Paige and Keegan 1994, Jakosky et al. 2000). Prior to the present work, Mellon et al. (2000)

provided the highest resolution thermal inertia map at $\frac{1}{4}^\circ$ per pixel for 50 °S to 70 °N based on Thermal Emission Spectrometer (TES) data from the early portion of the Mars Global Surveyor (MGS) mapping mission ($L_s = 103^\circ$ to 196°). They developed the thermal model and methodology used here, and their analysis identified three major thermophysical surface units. In this work, we include TES data from more than one Mars year, which allows us to increase the mapping resolution to $\frac{1}{20}^\circ$ per pixel and expand coverage to near-global extents. These improvements allow a more detailed analysis of Mars' thermophysical properties, enabling the characterization of additional regional surface units with distinct properties.

In subsequent sections, we discuss the TES observations included in our analysis and review the instrument characteristics and the methods used to determine thermal inertia as developed by Mellon et al. (2000). Next, we present new mapping results and our global and regional analyses thereof, including a discussion of thermophysical units. Here we focus on the comparison of thermal inertia with albedo, considering a range of physical explanations for each unit identified. We also examine the relationship between thermal inertia and elevation and its implications for the interaction of the atmosphere with surface materials. Finally, we report revised TES thermal inertia values for the Viking and Pathfinder landing sites, which provide a tie between surface properties as observed from the ground and those inferred from analysis of thermal inertia and other remote-sensing data.

2.2 TES thermal inertia derivation

The MGS mapping mission began on February 28, 1999, upon completion of aerobraking of the spacecraft when it entered a near-circular, near-polar orbit at about 400 km altitude with equator crossings at approximately 02:00 and 14:00 local Mars time. The mapping mission officially ended January 31, 2001,

extending slightly over one full Mars year (368 ° of L_s, starting from 103 °). An additional 3 months of data (42 ° of L_s) from the continuing extended mission was incorporated in the present mapping project, which thus includes TES orbits 1583–11254 obtained from February 28, 1999, through April 28, 2001. The TES instrument, which observes the martian surface every 2 s, consists of six 8.3 mrad-IFOV detectors arranged in a 2 × 3 array, each of which provides a nominal 3 × 3 km surface resolution. However, orbital insertion difficulties resulted in a direction of orbit opposite to the original design, making the disabling of the TES image motion compensation necessary and thereby causing a downtrack smear of 5.4 km (full-width at half-maximum) in the field of view for each detector. The TES platform includes three bore-sighted instruments: a 6- to 50-μm spectrometer, a 0.3- to 2.7-μm visible broadband channel (for albedo), and a 5.5- to 100-μm thermal bolometer. See Christensen et al. (1992) for a complete description of the TES instrument and Christensen et al. (2001) for a general overview of the mapping mission results.

Thermal inertia is derived for each TES observation from spectral and bolometric brightness temperatures as described by Mellon et al. (2000). In summary, a thermal model was used to generate a lookup table of temperatures for intervals of season (L_s), time of day, latitude, surface pressure, dust opacity, albedo, and thermal inertia (Jakosky 1979, Haberle and Jakosky 1991, Mellon et al. 2000). Each observed brightness temperature is correlated with other data and interpolated through the lookup table to find the best-fitting thermal inertia. Measurements of geographic and temporal opacity variations were not available at the time of processing, so the current algorithm assumes a constant infrared dust opacity of 0.1 at 6.1 mbar and scaled to the local elevation, consistent with average TES spectral observations during much of the mapping mission (Mellon et al. 2000, Smith et al. 2001b, Smith 2004). Water-ice-cloud opacities were not expected to

be available and are not taken into account by the thermal model.

Although a thermal inertia value is calculated for each temperature observation, the quality of the result is limited by the range and sampling interval of conditions included in the lookup table and thermal model. Therefore, to select thermal inertia values for mapping, we employed a series of filters to remove the adverse effects of temporal variations in the atmosphere which are not presently accounted for in the thermal model. Specifically, we rejected values from periods and locations of high opacity due to atmospheric dust and water-ice clouds (see Smith et al. 2001b, Smith 2004). For each of 36 'seasons' (10 ° intervals of L_s), we mapped TES daytime dust and water-ice-cloud opacity data at $\frac{1}{8}$ ° per pixel, filled these maps by interpolation, and then applied threshold opacities to create seasonal 'masks'. We then selected thermal inertia values for each season, masking out those values in geographic regions where the opacity thresholds were exceeded. The remaining thermal inertia values from all 36 seasons were binned into a global map with a grid size of $\frac{1}{20}$ ° in latitude and longitude ($\sim 3 \times 3$ km at the equator), which is approximately equivalent to the intrinsic resolution of the TES instrument. We compensated for the shrinking of the map-pixel scale with latitude due to converging lines of longitude by binning each thermal inertia value into all the longitudinal bins covered by its nominal observational footprint at each latitude. However, the downtrack smear of 5.4 km and the longitudinal variation within each observation ensure that any given TES observation does not fall entirely within a single map pixel even at low latitudes. Moreover, multiple observations of any particular location are only partially coincident with each other and the thermal inertia values calculated from them are not linearly related to the fluxes measured. Despite these concerns, we performed only a simple averaging of thermal inertia within each bin. Thus, the values within any given pixel throughout the map are actually representative of a somewhat larger area.

For most of the planet, we chose an infrared dust opacity threshold of 0.2, which is twice the opacity assumed in the model and proved to be optimal for eliminating most anomalously high thermal-inertia streaks without adversely affecting data coverage. In the Hellas impact basin, dust opacities are persistently high, and increasing the threshold to 0.3 became necessary for that region (28 °S to 56 °S, 265 °W to 317 °W) in order to retain sufficient data coverage for mapping. Frequent water-ice clouds in the low thermal-inertia ($I < 100$ tiu) regions near Tharsis resulted in the persistence of high thermal-inertia streaks after dust filtering, so we used a water-ice-cloud opacity threshold of 0.09 for that region (17 °S to 41 °N, 69 °W to 180 °W). To avoid including data from those times when CO_2 frost may be present, the data was further restricted to periods where surface temperatures are greater than 160 K. For the present work, we confined our mapping and analysis to thermal inertia values from nighttime thermal bolometer observations because their uncertainties ($< 6\%$) are lower than those from daytime and spectrometer observations ($< 17\%$) and are therefore more likely to be representative of the thermophysical properties of surface materials. These values include uncertainties in the instrument measurements, the thermal model, and the interpolation scheme employed to derive thermal inertia. They do not include uncertainties in ancillary data (most notably, dust opacity and albedo), which are difficult to quantify but may be as high as 10% or more. The filters described above are intended to minimize the effects due to high dust opacities. See Mellon et al. (2000) for a complete discussion of uncertainties associated with the methods employed here to calculate thermal inertia.

2.3 Results and analysis

In this section, we present results of the thermal inertia derivation from TES bolometer observations of nighttime brightness temperatures. A global map is

presented and discussed in relation to previous results and correlated with albedo, elevation, and other surface properties. We delineate global thermophysical units, highlight regional features, and analyze high-resolution results for past landing sites.

2.3.1 Global thermal inertia map

Figure 2.1 shows the global map of thermal inertia derived from nighttime TES bolometer observations of the brightness temperature of Mars as described in the previous section. At the mapped resolution ($\frac{1}{20}^\circ$ per pixel), approximately 60% coverage was obtained using mapping mission data (see Fig. 2.2), and the remaining locations have been filled by interpolation between 80 °S and 80 °N latitudes for display purposes. Due to the orbital inclination of the MGS spacecraft, only sparse data exist polewards to about 87° latitude, above which no usable data are available. Gaps in geographic coverage occur during calibration and limb observations and when temperatures exceed the bounds in the lookup table, indicative of thermal inertia outside the range allowed in the present model (24–800 tiu). For example, relatively large gaps in coverage exist in the Tharsis region where certain areas exhibit nighttime surface temperatures consistent with thermal inertia lower than 24 tiu. Smaller areas with surface temperatures indicative of thermal inertia higher than 800 tiu are also present, in locations such as the floor of Valles Marineris and on the rims of Hellas and Isidis basins.

This map incorporates about 3 times more data than the previous TES thermal inertia map (Mellon et al. 2000) and includes observations from more than a full martian year, thus allowing us to improve resolution 5-fold and expand the coverage to near-global extents. Our results are broadly consistent with previous IRTM and TES results (cf. Palluconi and Kieffer 1981, Paige et al. 1994, Paige and Keegan 1994, Vasavada et al. 2000, Jakosky et al. 2000, Mellon et al. 2000). How-

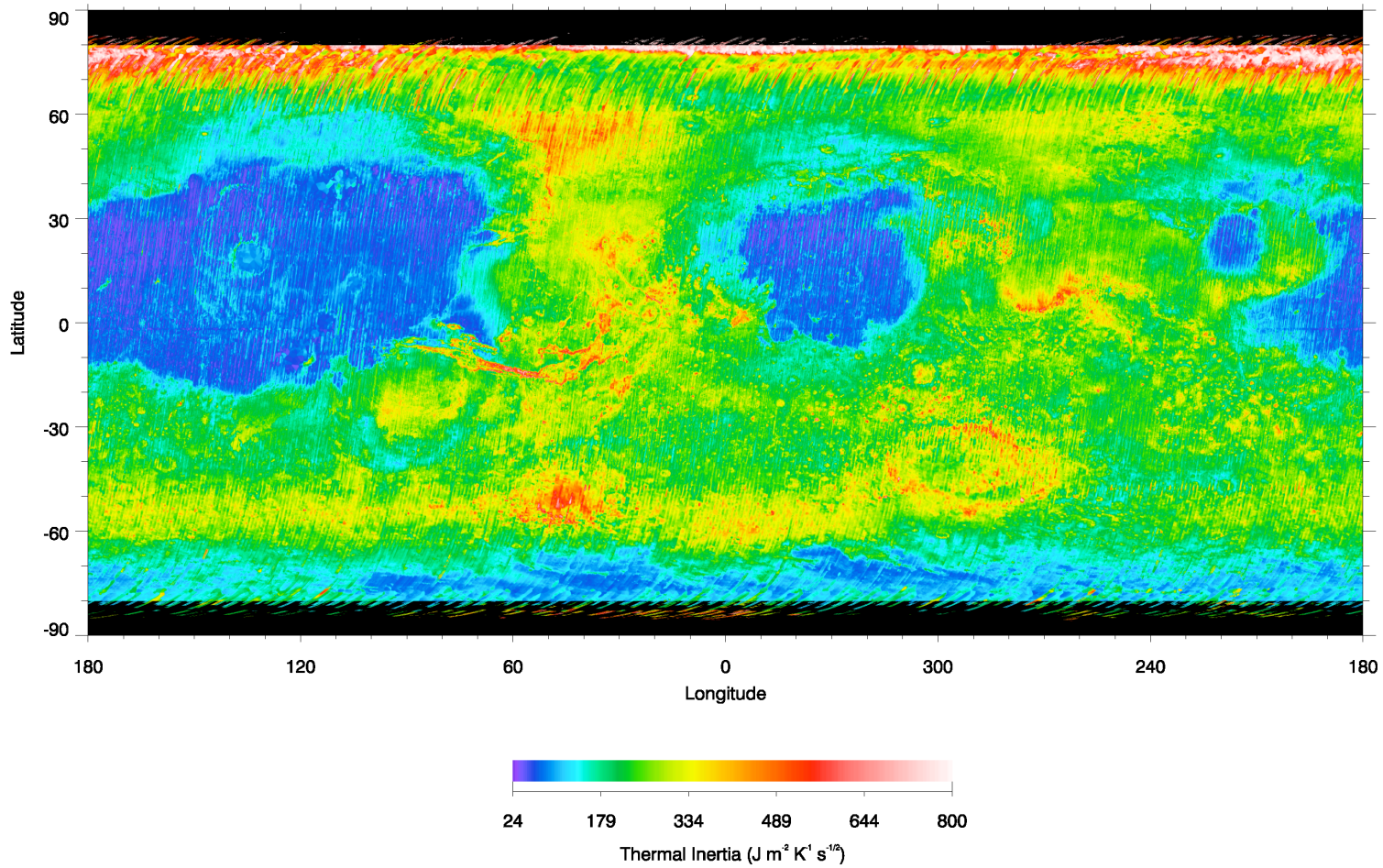

Figure 2.1 Nighttime bolometric thermal inertia map of Mars. Thermal inertia is mapped at a resolution of $\frac{1}{20}^\circ$ per pixel from TES orbits 1583–11254. Interpolation is used to fill missing data between TES ground tracks for latitudes 80°S to 80°N. See text for discussion.

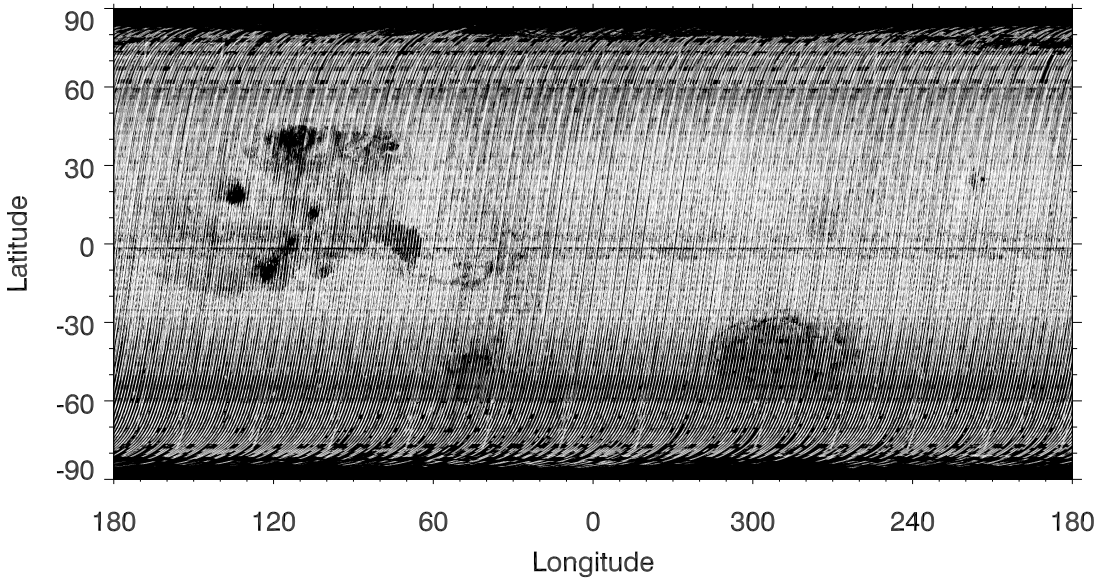

Figure 2.2 Coverage (in white) of data in Fig. 2.1 prior to filling by interpolation. Approximately 60% of the map contains TES-derived thermal inertia values between 80 °S and 80 °N latitudes. See text for discussion.

ever, several processing artifacts are observable in Fig. 2.1. The roughly north–south trending streaks, which become more pronounced polewards of 60 °N, are largely due to variations in atmospheric dust loading which violate the assumption of constant infrared dust opacity (0.1) used here in the calculation of thermal inertia. The high thermal inertia areas polewards of 65 °N show greater occurrence and magnitude of streaking which are not consistent with results from IRTM (cf. Vasavada et al. 2000, Paige et al. 1994). These high thermal inertia values cannot be entirely attributed to dust or water-ice clouds, since the associated observations were made during a period of generally low opacity (Smith 2004) and we filtered out thermal inertia values for times and locations of unusually high opacities. Seasonal restrictions and the MGS orbit path are such that most of the data from the north polar region are taken in close proximity to polar dawn.[1] Temperatures change rapidly near dawn and sampling limitations of the lookup

[1] In the publication associated with this chapter (Putzig et al. 2005), this statement was

table may yield anomalously high thermal inertia. This effect is not an issue for the south polar region, where the orbit path is generally further from the polar dawn during equivalent seasons.[2]

Our new TES thermal inertia results are generally consistent with those from IRTM throughout the south polar region (cf. Vasavada et al. 2000, Paige and Keegan 1994). Figure 2.3 shows a comparison between our results and those of Vasavada et al. (2000) for 60 °S to 80 °S and demonstrates a close correspondence, particularly for lower thermal inertia values. We attribute the range of TES values for any given IRTM value to differences in spatial resolution between the two instruments (i.e., TES may detect smaller-scale surfaces of higher and lower thermal inertia). Differences in the atmospheric models used for each dataset are likely to be responsible for the divergence of the histogram peak from the 1:1 line at higher thermal inertia, where the TES results are systematically higher than those from IRTM.

2.3.2 Global and regional analysis

Comparison of thermal inertia and other data sets can provide greater insight into the characteristics of martian surface materials than is achievable by examining each property independently. We used global maps of albedo and elevation binned at the same resolution ($\frac{1}{20}$ ° per pixel) for comparison to the thermal inertia map. TES visible bolometer Lambert albedo observations covering the same time period as was included in the thermal inertia map were incorporated into an albedo map (Pelkey and Jakosky 2002), and we used the entire MOLA

originally preceded by the phrase, "Although the local time of these observations is nominally 02:00," but these observations are 'nighttime', i.e., with solar incidence angles > 90 °, and they include nominal 14:00 (as well as 02:00) observations.

[2] While the effects discussed here may be contributing factors, subsequent analysis indicates that the observed streaking, both at mid-latitudes and in the polar regions, is largely due to seasonal and diurnal variations in apparent thermal inertia that may be attributable to surface heterogeneity (see Chapter 4).

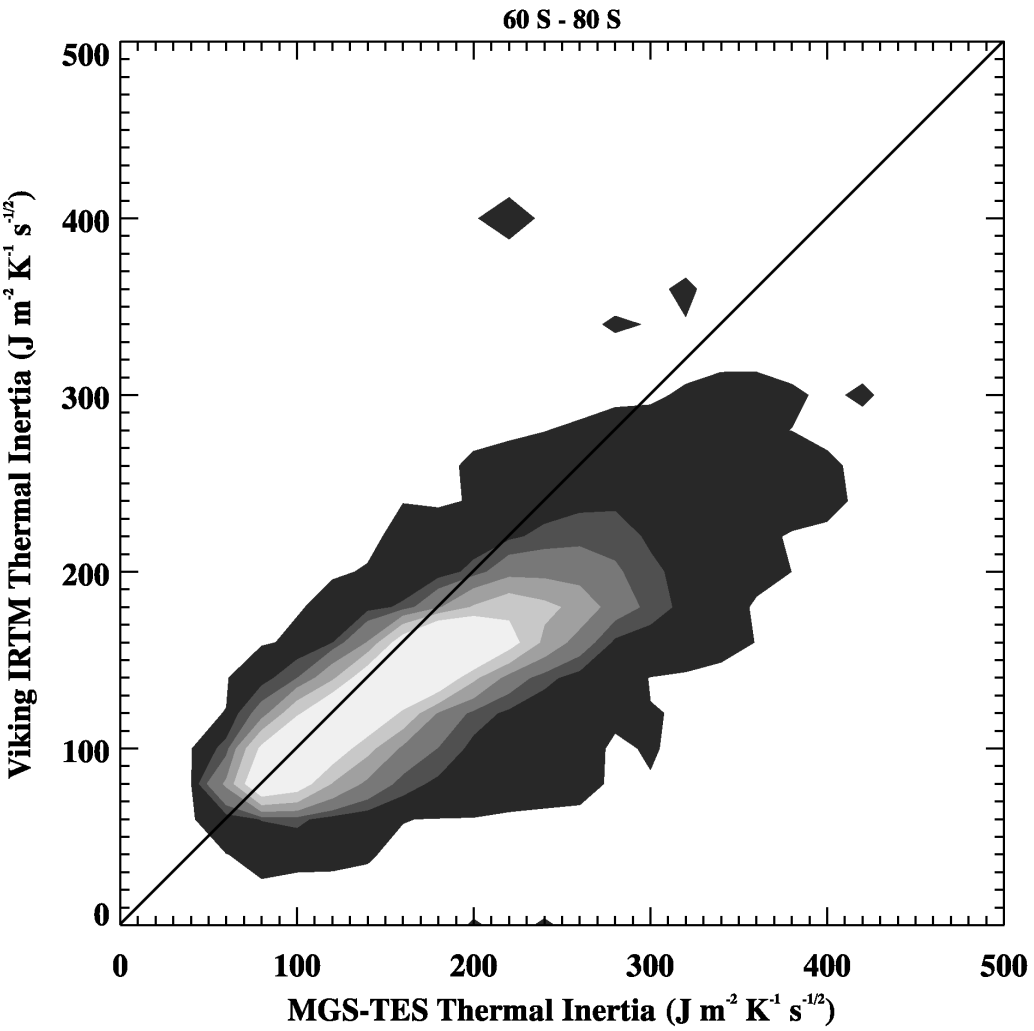

Figure 2.3 Cross-plot of thermal inertia values derived from MGS-TES with those from Viking IRTM (Vasavada et al. 2000) for 60 °S to 80 °S. Both datasets are mapped at $\frac{1}{2}^\circ$ per pixel and binned at 20 tiu. Diagonal line is 1:1.

dataset to create an elevation map. Mars Orbiter Camera (MOC) images and Viking MDIM 2.0 mosaics were also used in our analysis of surface features. We correlated maps and created two-dimensional histograms between datasets to delineate areas with common features and to assign thermophysical mapping units. These units were then mapped back to their surface locations to create unit maps.

2.3.2.1 Thermal inertia–albedo units

We begin by considering the quantitative comparison of thermal inertia and albedo, which is used to delineate thermophysical surface units. In a previous analysis of TES-derived thermal inertia, Mellon et al. (2000) identified three major units of distinct albedo and thermal inertia characteristics. These are regions of (A) low thermal inertia and high albedo, interpreted as surfaces dominated by unconsolidated fines (dust with grain sizes less than about 40 μm); (B) high thermal inertia and low albedo, interpreted as surfaces composed of coarser-grained sediments, rocks, bedrock exposures, and some duricrust; and (C) high thermal inertia and intermediate albedo, interpreted as surfaces dominated by duricrust with some rocks and/or bedrock exposures. These interpretations were based on consideration of physical properties appropriate to the observed albedo and thermal characteristics of the surface, and were supported by previous studies of surface properties based on Viking IRTM data and lander observations (Kieffer et al. 1977, Palluconi and Kieffer 1981, Christensen 1986b, Christensen and Moore 1992).

Figure 2.4 shows a global 2D histogram of thermal inertia and albedo using our unfilled maps, with each occurrence weighted by the surface area of its $\frac{1}{20}^\circ$ pixel so as not to falsely emphasize the high latitudes. Our results are similar to those of Mellon et al. (2000) and include further subdivision of the thermal inertia–albedo parameter space. For this study, the major unit boundaries were modified to encompass the three peaks of the global histogram while excluding the second-lowest histogram frequency level ($<$ 1669 points per bin) in order to provide a separation between each major unit and between the major units and their outliers. The outliers were subdivided into regions of (D) low thermal inertia and low-to-intermediate albedo; (E) very low albedo; (F) very high thermal

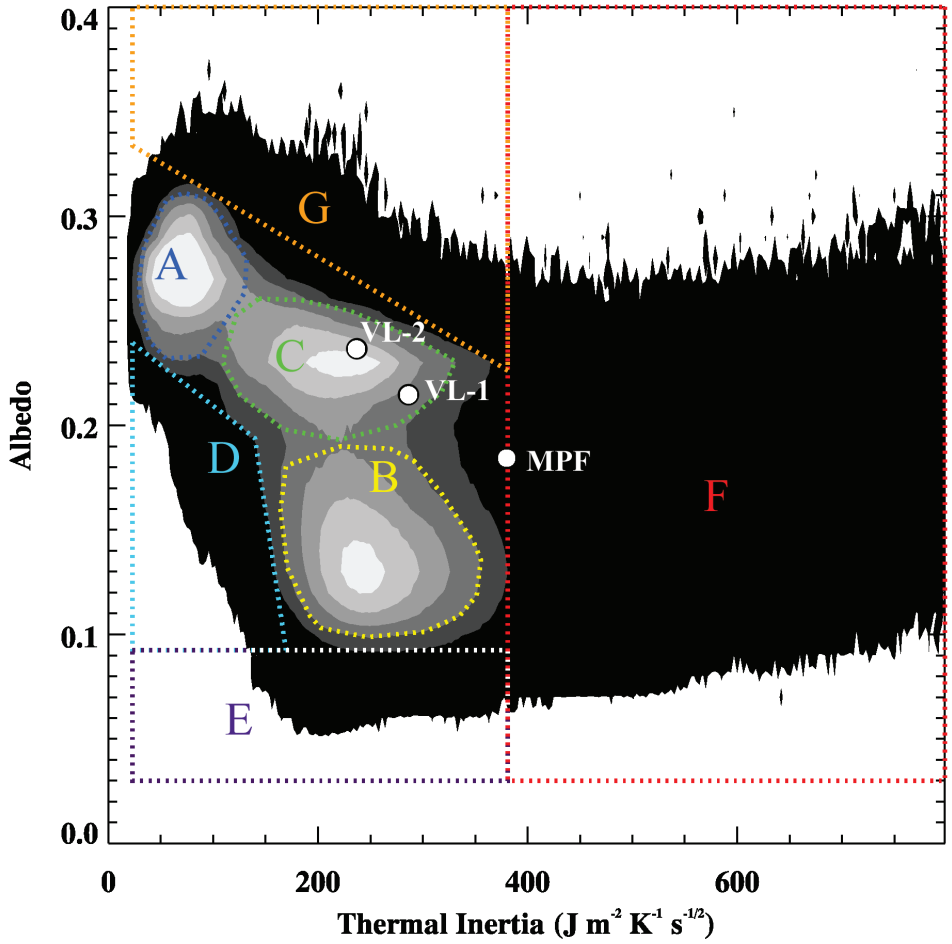

Figure 2.4 Two-dimensional histogram showing global correlation between TES nighttime bolometric thermal inertia and visible bolometric albedo, from unfilled maps. Thermal inertia bin size is 3 tiu. Albedo bin size is 0.01. White areas represent no occurrences. Filled contour levels are 1, n/20, n/10, n/5, n/3, and n/2, where n = 16691.6 is the maximum in a single bin wherein each occurrence is weighted by the cosine of its latitude to account for the represented surface area. Three modes of frequent correlation are assigned as Units A, B, and C, with outliers assigned to Units D, E, F, and G. Unit letters correspond to those in Fig. 2.5 and Table 2.1.

inertia; and (G) very high albedo. A global map of all units (Fig. 2.5) shows their spatial distribution on the surface of Mars. The previously identified units (A–C)

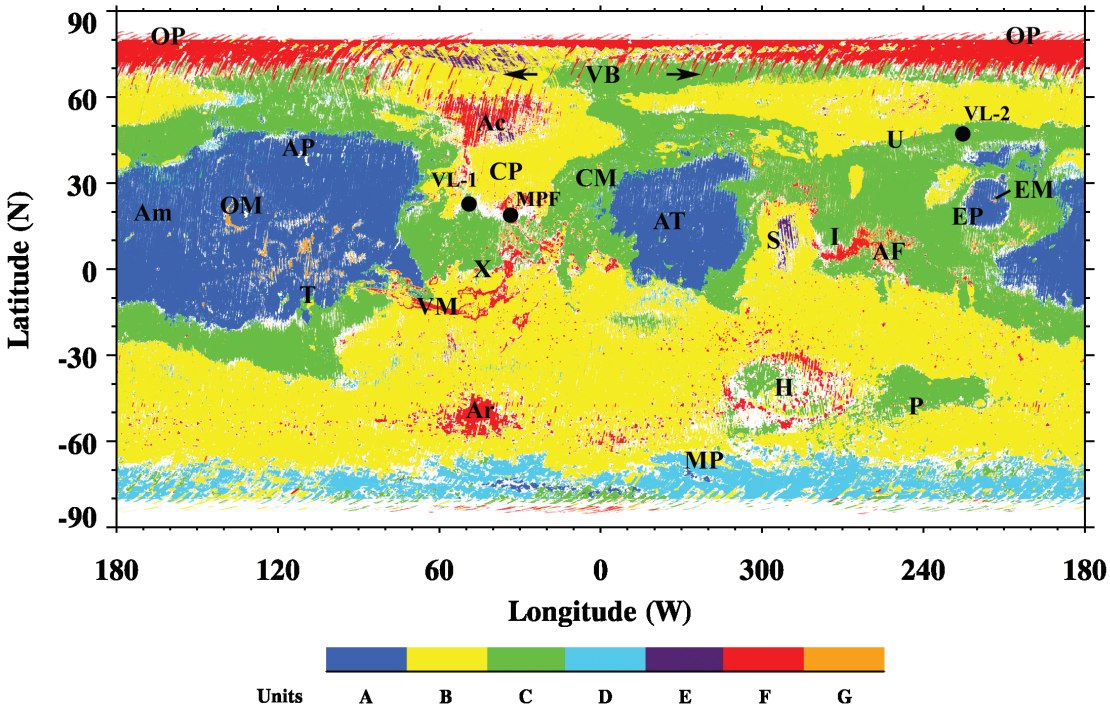

Figure 2.5 Thermal inertia–albedo unit map of Mars. Units represent thermal inertia–albedo modes in Fig. 2.4. White areas correspond to regions between unit bounds in Fig. 2.4 and to no-data regions beyond 80° latitude. See Table 2.1 for interpretation and text for discussion. Lander locations and regions discussed in the text: VL-1, Viking Lander 1; VL-2, Viking Lander 2; MPF, Mars Pathfinder Lander; Ac, Acidalia; AF, Amenthes Fossae; Am, Amazonis; AP, Alba Patera; Ar, Argyre; AT, Arabia Terra; CP, Chryse Planitia; CM, Cydonia Mensae; EM, Elysium Mons; EP, Elysium Planitia; H, Hellas; I, Isidis; MP, Malea Planum; P, Promethei Terra; OM, Olympus Mons; OP, Olympia Planitia; S, Syrtis Major; T, Tharsis; U, Utopia Planitia, VB, Vastitas Borealis; VM, Valles Marineris; X, Xanthe Terra.

compose 78% of Mars' surface area (from the interpolation-filled map) and remain largely unchanged geographically from those of Mellon et al. (2000), with minor differences due to the inclusion of additional data and the modification of the unit boundaries. The new units (D–G) associated with the outliers of global thermal inertia and albedo, which we discuss in detail below, show clear regional groupings, implying surface characteristics distinct from those expected for the

Table 2.1. Mars thermal inertia–albedo units

Unit	Inertia (tiu)	Albedo	% Surface[a]	Interpretation
A	Low (28–135)	High (0.23–0.31)	19	Bright unconsolidated fines
B	High (160–355)	Low (0.10–0.19)	36	Sand, rocks, and bedrock; some duricrust
C	High (110–330)	Med. (0.19–0.26)	23	Duricrust; some sand, rocks and bedrock
D	Low (24–170)	Low–Med. (0.09–0.24)	2	Low density mantle **or** dark dust?
E	High (140–386)	Very Low (< 0.09)	0.3	As B, but little or no fines
F	Very High (> 386)	All	4	Rocks, bedrock, duricrust, and polar ice
G	Low–High (40–386)	Very High (> 0.23)	0.7	As A, thermally thin at higher inertia

[a]From the interpolation-filled unit map (Fig. 2.5).

major global units. Table 2.1 lists the ranges in thermal inertia and albedo and our interpretation for each unit.

Figure 2.6 provides an orthographic map of these units centered on the south pole, showing their spatial distribution in the southern hemisphere. Unit D dominates the region polewards of about 65 °S and exhibits distinct low-thermal-inertia boundaries (cf. Fig. 2.7), making it unique from the surrounding higher thermal inertia Units B and C. Because of the observed relationship between conductivity and grain size under Mars surface conditions, the low thermal inertia values of Unit D (similar to those of Unit A) are normally considered to be indicative of fine-grained, unconsolidated materials (i.e., dust). However, fine-grained materials on Mars normally have high albedo (such as the equatorial deposits in Unit A) whereas the albedo of Unit D is much lower and comparable to that of Unit B.

Before considering physical explanations for Unit D, we will briefly address potential photometric effects relating to the computation of albedo. The TES albedo used in this analysis and in the calculation of thermal inertia is computed relative to a Lambert surface (i.e., a perfectly reflecting surface with reflectance independent of viewing angle and varying only as the distance from the illumination source and the cosine of the incidence angle) (Christensen et al. 2001). In reality, planetary surfaces tend to be either forward or backward scattering to some extent. Such properties may result in a more complex dependence of the surface reflectance on incidence angle and add a dependence on the cosine of the emission (viewing) angle. In computing albedo relative to a Lambert surface, emission angle effects can be minimized by using only near-nadir observations, as is done for TES. However, a dependence of albedo on incidence angle (and hence latitude) may remain, depending on the scattering properties of the atmosphere and surface material. This possibility raises the question as to whether Unit D might actually have photometric properties (and albedo) similar to those

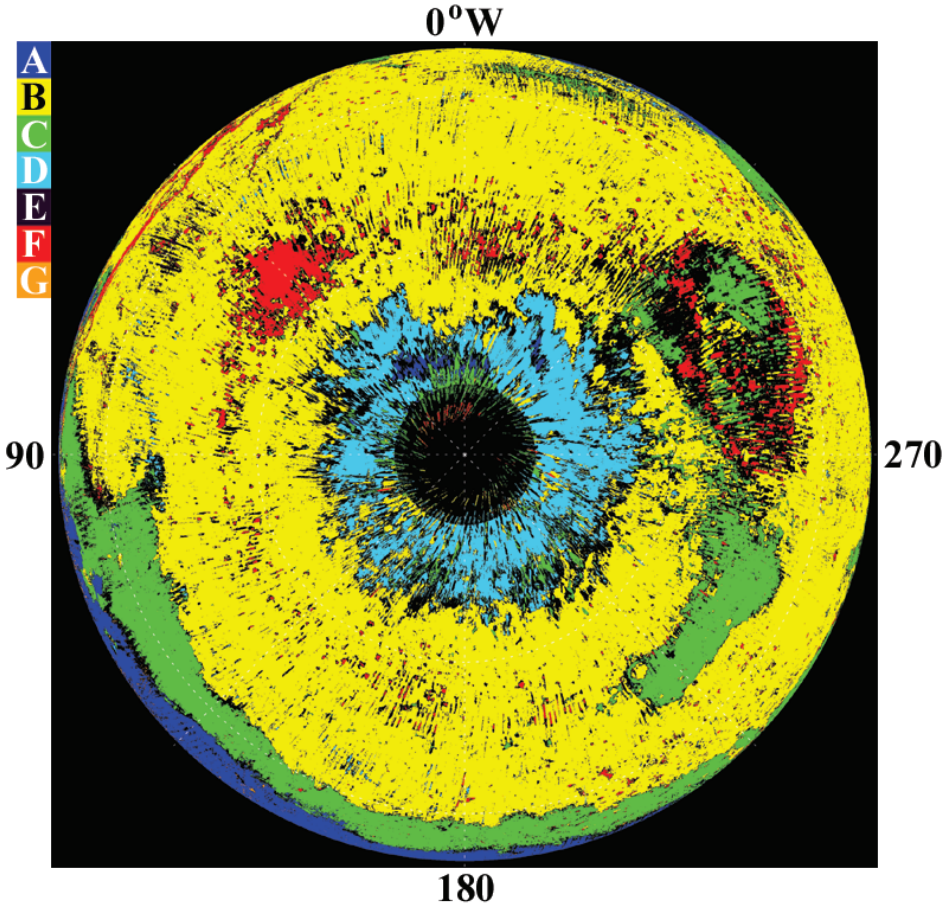

Figure 2.6 Thermal inertia–albedo unit map in an orthographic projection of the southern hemisphere of Mars filled to 80 °S. Unit letters correspond to those in Fig. 2.4 and Table 2.1. The northernmost latitude shown is 0 ° (the equator).

of Unit A, with the lower effective Lambert albedo of Unit D caused by a reduction in surface reflectance at higher incidence angles.

Various empirical methods have been developed to incorporate photometric effects into albedo calculations in an effort to separate scattering characteristics from other surface material properties (Minnaert 1941, Kieffer et al. 1976, 1977, Pleskot and Miner 1981, Hapke 1981, Hapke and Wells 1981, Squyres and Veverka 1982, Hapke 1984, 1986, 1993, 2002). To compare these methods, we calculated

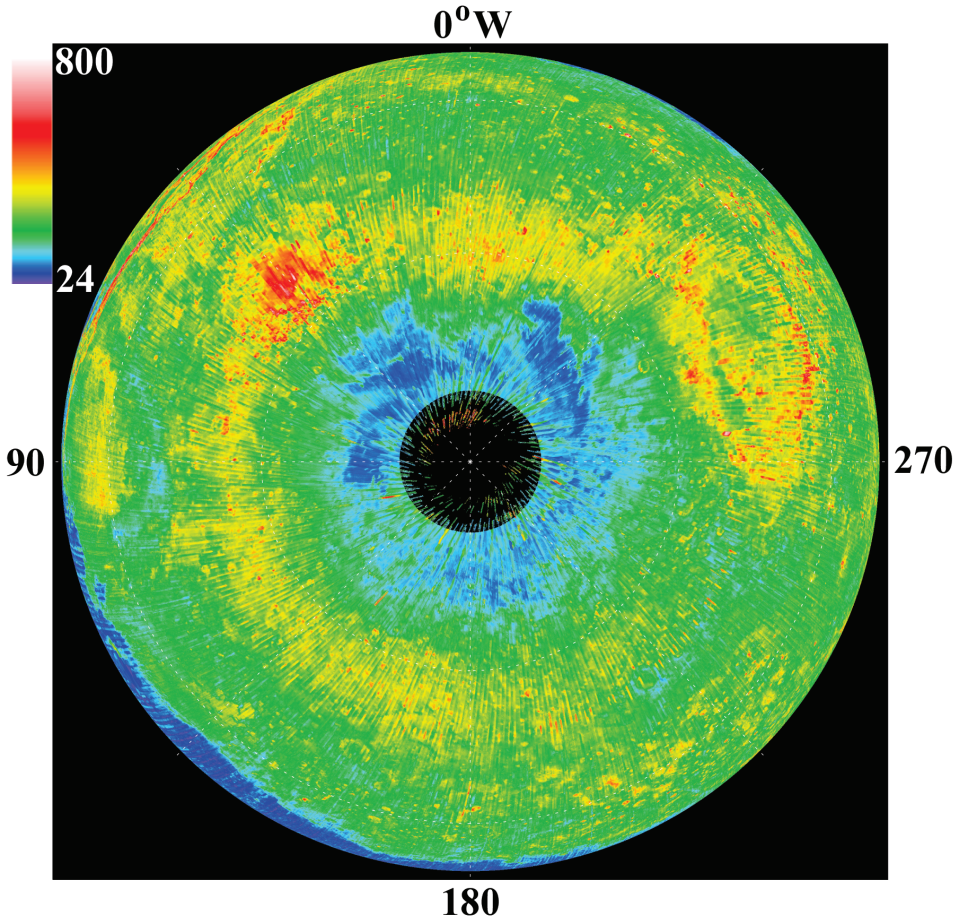

Figure 2.7 Thermal inertia map of the southern hemisphere of Mars in the same projection as Fig. 2.6, filled to 80 °S. Compare polar low thermal inertia region (blue) to Unit D in Fig. 2.6. The northernmost latitude shown is 0 ° (the equator).

albedo as a function of incidence angle for a Lambert surface and for four other photometric functions that have been used to match previous observations of Mars, assuming unit reflectance in each case. We then normalized the Lambert albedo by each of the others to produce a 'Lambert-equivalent' albedo for each function (see Fig. 2.8). Kieffer et al. (1977) fit IRTM data from the early portion of the Viking mission with an empirically-derived exponential function (curve a in Fig. 2.8). Later, Pleskot and Miner (1981) found that a Minnaert surface with

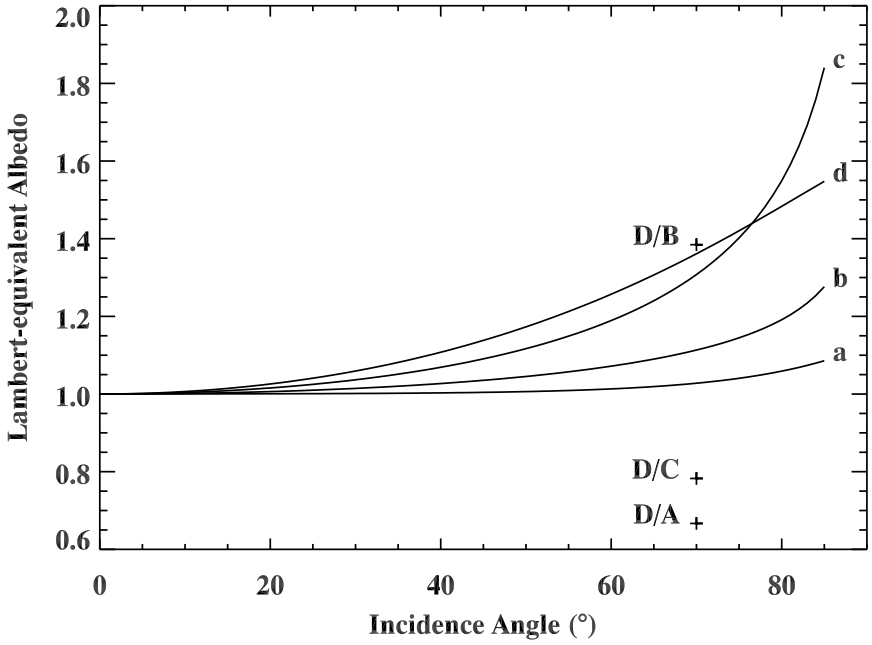

Figure 2.8 Variation of Lambert-equivalent albedo with incidence angle relative to (a) an empirically-derived photometric function based on Viking IRTM data (Kieffer et al. 1977), (b) a Minnaert surface with an exponent of 0.9 (Pleskot and Miner 1981), (c) a Minnaert surface with an exponent of 0.75 (Pleskot and Miner 1981), and (d) an isotropic Hapke surface with single-scattering albedo of 0.5 (Hapke and Wells 1981). Symbols represent the ratios of the median albedo of Unit D to those of Unit A, Unit B, and Unit C. See text for discussion.

an exponent of 0.9 provided a good fit for the complete IRTM dataset (curve b in Fig. 2.8) and suggested a Minnaert exponent of 0.75 (curve c in Fig. 2.8) as an upper limit for albedo uncertainties due to non-lambertian surface reflectance. Hapke (1981) derived an approximate analytical solution to the radiative transfer equation incorporating scattering effects from particulate surfaces, and then Hapke and Wells (1981) applied that solution to fit Mariner 9 data, using isotropic scattering properties and a single-scattering albedo of 0.5 (curve d in Fig. 2.8). In each case, the effective (Lambert-equivalent) albedo increases with incidence angle, whereas the high-latitude Unit D albedo is substantially lower than that of Unit A (point D/A in Fig. 2.8). This observation suggests that Unit D is unlikely

to be the result of non-lambertian photometric characteristics of Unit A materials. However, Squyres and Veverka (1982) used a simple model of surface roughness to show that for extremely rough surfaces ($Q > 0.2$, where Q is the depth-to-radius ratio for parabolic craters used to model roughness), the effective albedo may actually be reduced below that of a Lambert surface at high incidence angles due to shadowing effects. Although there is not presently sufficient evidence to entirely rule out this possibility for Unit D, an analysis of MOLA data by Smith et al. (2001a) shows that 100-m scale roughness is less than 6 m (i.e., $Q < 0.06$) for the south polar region, indicating that at least the large-scale roughness is insufficient to significantly reduce the albedo. Therefore, the probability remains high that any non-lambertian photometric effects are acting in the opposite direction from that required to equate Units A and D.

Further evidence for a compositional distinction between these units comes from a study of TES daytime infrared spectra by Ruff and Christensen (2002). They presented a map of dust-cover index based on particle size effects on emissivity in the 1350–1400 cm^{-1} wavenumber range which suggests that there are no substantial exposures of unconsolidated dust with Unit A characteristics in the region shown as Unit D in Fig. 2.6.

The extent to which non-lambertian surface properties may influence the thermal inertia results is not entirely clear. In the polar regions, a higher effective albedo for a given material should result in lower surface temperatures throughout the diurnal cycle. Nominally, this effect might result in a lower value of nighttime thermal inertia, but the lower temperature should be compensated to some extent by the use of the measured TES Lambert albedo values. Fully characterizing any residual effects will require incorporating a non-lambertian photometric function into the thermal model. Although there is a general trend toward lower thermal inertia in the south (Fig. 2.7) which is nominally consistent with a photometric

effect acting on Unit B materials (point D/B in Fig. 2.8), the reduction in thermal inertia to Unit D is quite large and occurs rather abruptly and at various latitudes for different longitudes (see Figs. 2.6 and 2.7). Thus, the values of thermal inertia as well as those of albedo calculated for Unit D are likely to be controlled predominantly by surface material characteristics and not by photometric effects.

We now consider several physical explanations for Unit D. This unit may be either of a unique origin or the result of some alteration process acting on one of the other major surface units. Mineralogical mapping (Bandfield 2002) shows no correlation with the unit bounds, suggesting that a unique composition is unlikely. Possible alteration processes may be separated into three classes: (1) reduction of albedo in material that is otherwise similar to that in Unit A, either through a compositional difference or a darker coating on individual grains; (2) reduction of thermal inertia in material that is otherwise similar to that in Unit B, which can be achieved by lowering bulk conductivity (see Eq. 2.1); and (3) reduction of both albedo and thermal inertia in a material that is otherwise similar to that in Unit C.

For the first of these classes, Unit D may represent a surface of fine-grained, unconsolidated materials (dust) with thermal properties similar to those of Unit A but of a composition which is either distinct from that in Unit A (implying a distinct source of dust), or the same as that in Unit A but altered by a darkening process. If of distinct composition, the darker material might be either a layer which is "thermally thin" (much thinner than a thermal skin depth, i.e., a few cm) but "optically thick" (thicker than a few μm) overlying a bright dust identical to that in Unit A, or a thicker dark layer with similar thermal properties to that in Unit A. Alternatively, the individual grains of an initially bright dust may be coated by a darker material, presumably by some chemical process which is restricted to the south polar zone. A problem with these dark dust theories is the

fact that global dust storms on Mars are expected to homogenize unconsolidated fines over years to decades (Kahn et al. 1992), especially in the near-surface. Therefore, maintaining a localized region covered with a distinctly different, dark dust over extended periods is difficult. Viking IRTM results (Vasavada et al. 2000, Paige and Keegan 1994) show a similar pattern of low thermal inertia in this region, so this phenomenon is unlikely to be transient over a period of several decades.

For the second class of explanations, Unit D may represent a surface of either indurated fines or coarser-grained materials in which the bulk thermal conductivity has been lowered. Laboratory data show a linear dependence of thermal conductivity on density with a slope of about 0.0225 $\mathrm{W\,m^2\,kg^{-1}\,K^{-1}}$ (Presley and Christensen 1997c). Using Eq. 2.1 and assuming a constant heat capacity (appropriate for a constant composition), we calculate that the observed 2-fold reduction in thermal inertia from Unit B to Unit D would require about a 2.5-fold reduction in density. Such a reduction may seem extreme, but recent estimates of ground ice within the top meter of the martian surface based on data from the Mars Odyssey Neutron Spectrometer (Boynton et al. 2002) predict up to 75% ice by volume in the south polar regions. In the upper few centimeters (the TES sensing depth), ice is seasonally unstable even at high latitudes and the regolith is expected to desiccate (Mellon and Jakosky 1995, Mellon et al. 2004). Conceivably, such an ablation zone may produce a near-surface layer with greatly expanded pore volume and reduced bulk density. Storrs et al. (1988) performed laboratory studies of sublimation processes for mixtures of volatile ices and various silicates, and found that hydrated phyllosilicate mineral grains will bond to form very high porosity residues with relatively high tensile strength, which they refer to as filamentary sublimate residues. They measured low thermal conductivity in these materials, suggesting that heat conduction occurs predominantly through the pore

spaces rather than across grain contacts. A field example of sublimation forming a highly porous residue is located in the U. S. Army Cold Regions Research and Engineering Laboratory's Fox Permafrost Tunnel, which was bored into a loess hill near Fairbanks, Alaska. Circulation of cold, dry air through the tunnel during winter months since its construction in the 1960s has produced a desiccated soil layer on the walls and ceiling of the tunnel up to 10 cm thick. This tunnel and other nearby loess outcrops were discussed by Johnson and Lorenz (2000) as an analog for the Mars polar layered terrain. They found that the desiccated loess has low densities (800–1400 $\mathrm{kg\,m^{-3}}$), moderate shear strength (4 kPa), and low thermal conductivity (0.1–0.7 $\mathrm{W\,m^{-1}\,K^{-1}}$ at 1 bar). They calculated an effective thermal inertia of 114 tiu for these materials at Mars surface pressure, which is in keeping with thermal inertia values derived for Unit D in the south polar region (Table 2.1). Consistent with this hypothesis, Mustard et al. (2001) provided geomorphologic evidence of a widespread surface mantle of a few m thickness which appears to be dissected at mid-latitudes (30 ° to 60 °) in each hemisphere. They suggested that this mantle contains ground ice emplaced during the last period of high obliquity and that the observed dissection is caused by the removal of the now-unstable ground ice. Additionally, we examined about 40 MOC images from Malea Planum (60 °S to 70 °S, 315 °W to 345 °W), where the change in thermal inertia between Units B and D is most distinct (see Fig. 2.7). We found a mantled appearance in both regions, and although we observed no abrupt morphological changes in images extending across the boundary between the units, images over Unit D show more polygonal and cracked surfaces than those over Unit B which appear generally smoother (e.g., Fig. 2.9). These features may represent thermal contraction cracks in ice-rich permafrost, which result from tensile stresses driven by seasonal temperature oscillations in the subsurface (e.g., Lachenbruch 1962, Mellon 1997). These temperature variations, and resulting thermal contraction

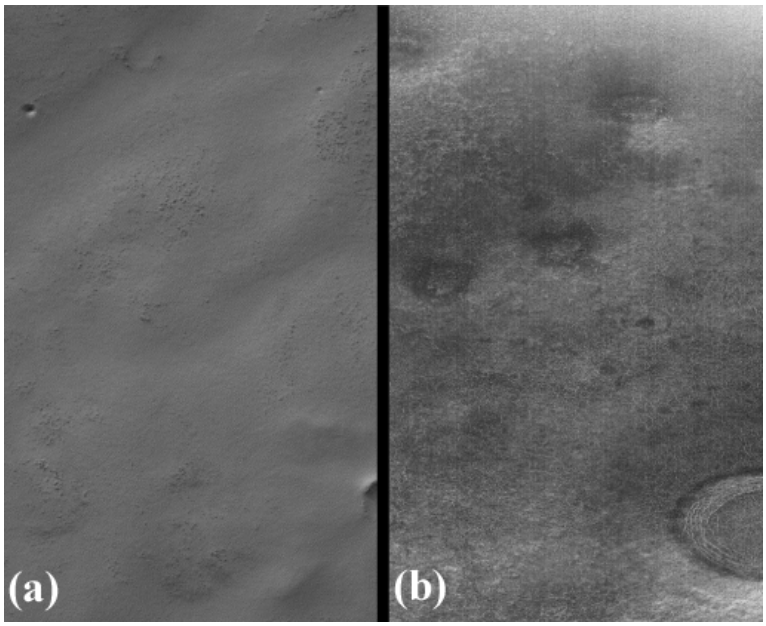

Figure 2.9 Unprojected MOC images over (a) Unit B [MOC Image M19/00982, near 321 °W, 62 °S] and (b) Unit D [MOC Image M08/06534, near 326 °W, 69 °S]. Mantled surfaces appear in both images and 'cracked' surface appears in (b). Both images are about 2.8 km wide.

stresses, are greater nearer to the surface. The shallower the ice-cemented ground, the greater the affinity for polygon formation. Therefore, the observed polygonal crack networks may be indicative of an extended period of shallow ground ice, relative to regions devoid of polygonal networks. A recent theoretical estimation of the global ice table depth on Mars by Mellon et al. (2004) predicts a shallower stability for ground ice in the Unit D region than in the Unit B region, which may explain the observed distribution of the polygonal and cracked surface features.

An important consideration is that the density reduction theory given here does not explain the lack of a similar phenomenon in the north polar region. Recent Mars Odyssey neutron data (Mitrofanov et al. 2003) show even more extensive ground ice in the north than in the south, so one might expect a similar process to occur there, but the current thermal inertia map actually shows a zone

of high thermal inertia at most longitudes polewards of 65 °N (Fig. 2.1). Although we attribute some of these high values to possible model effects[3] (see previous section and Mellon et al. 2000), we see no regional reduction in thermal inertia in those areas where the data appear to be more reliable. Moreover, thermal inertia values calculated from IRTM data polewards of 65 ° latitude (Paige et al. 1994, Paige and Keegan 1994, Vasavada et al. 2000) are about 100–200 higher in the north than in the south, which is consistent with the continuation of Units B and C up to the edge of the north residual polar cap. Future efforts to characterize better the thermal inertia in the north may help resolve this discrepancy.

The third class of explanations for Unit D requires smaller reductions in both albedo and thermal inertia of initially Unit C material in order to produce the characteristics found in Unit D. This scenario involves darkening and reduction of bulk conductivity and is likely to require multiple causes, since physical processes which reduce bulk conductivity (e.g., grain size reduction by erosion) will normally increase albedo. Currently, such intermediate explanations are not readily distinguishable, but they do suffer from the same concerns about darkening processes and global dust homogenization discussed previously for the dark-dust scenario.

In summary, the unusual combination of low thermal inertia and low albedo that defines Unit D presents an interesting challenge to interpretation. At present, the possibility of a fine-grained material with either a dark coating or a unique composition cannot be entirely ruled out. However, concerns about dust homogenization and the lack of a distinct change in albedo at the boundaries of Unit D suggest that such an explanation is unlikely. We favor the second class of explanations discussed above, in which a $\sim$ 2.5-fold density reduction of Unit B material

[3] Subsequent analysis suggests that these high values actually result from the effects of surface heterogeneity (see Chapter 4) and the inclusion of local times near 14:00.

produces Unit D, probably as a result of the desiccation of a formerly ice-rich near-surface.

The interpretation of the remaining units (E–G) is relatively straightforward. Unit E is characterized by high thermal inertia and very low albedo and is geographically confined to moderately-sized regions in Syrtis Major, Acidalia, and a portion of Vastitas Borealis north of Acidalia, with much smaller, scattered occurrences south of Valles Marineris and in Utopia Planitia. Each of these regions is predominantly surrounded by Unit B (except some portions of Unit E in Acidalia which are surrounded by Unit F), and given the similarity of thermal inertia between the two units (see Fig 2.4), a close relationship between Units B and E is a reasonable suggestion. The lower albedo of Unit E is consistent with a strong reduction in the presence of unconsolidated fines in these areas (i.e., a higher proportion of darker duricrust, coarse grains, and rocks). Alternatively, a lower albedo may indicate a surface which has been subjected to a lesser degree of chemical weathering in the case of dust-free surfaces (e.g., fresh basalt).

Unit F is defined by very high thermal inertia and is located in Valles Marineris, Simud Valles, southern Chryse Planitia, Argyre Planitia, Hellas Rim, southern Isidis Planitia, Acidalia, northern Vastitas Borealis, Olympia Planitia, and the edges of both residual polar caps. Other small occurrences are generally located within impact craters throughout the southern highlands, suggestive of intracrater dune deposits (e.g., Pelkey et al. 2001). Typically, Unit F regions are surrounded by Units B and C, extend over a similar range in albedo, and have thermal inertia values consistent with surfaces of very coarse-grained or highly indurated materials, high rock abundance, and bedrock exposures. Unit F occurs at the edges of the northern and southern polar caps (90°E to 120°W, 77°N to 87°N and 83°S to 87°S; cf. Tanaka and Scott 1987) and its high thermal inertia values here are likely due to surface exposures of water ice. Similarly, the highest

values of thermal inertia within Unit F in northern Vastitas Borealis are associated with high albedo (> 0.18) and correlate well with regions south of Olympia Planitia mapped as perennial ice which are detached from the main body of the residual polar cap (Tanaka and Scott 1987). However, the slightly-lower thermal inertia streaks extending across Vastitas Borealis are suspected to be artifacts of the thermal model (see previous section).[4]

Unit G is defined by very high albedo and is found predominantly within the confines of Unit A in the Tharsis region and near Olympus Mons and the Elysium Montes. Smaller occurrences are located in Shalbatana, Simud, and Tiu Valles (canyons debouching into Chryse Planitia from the south), Amenthes Fossae, and on the walls of many large craters in Xanthe Terra and western Arabia Terra. Because of its high albedo and association with Unit A, Unit G probably represents deposits of the finest dust (see, however, Bridges 1994). Those portions of Unit G with higher thermal inertia may represent a cover of dust which is thermally thin (less a skin depth, i.e., a few cm) over material that might otherwise display the characteristics of the surrounding Units C and F.

2.3.2.2 Thermal inertia–elevation units

Quantitative comparison of thermal inertia with elevation can be used to delineate surface units which inform our understanding of the vertical distribution of surface materials and their interaction with the atmosphere. A global 2-D histogram of thermal inertia and elevation (Fig. 2.10) shows 4 nearly-aligned modes, indicating the bimodal distribution of both parameters. This result is consistent with earlier analyses using lower-resolution IRTM and TES maps (Jakosky 1979, Palluconi and Kieffer 1981, Mellon et al. 2000) and demonstrates that the vertical

[4] Subsequent analysis suggests that these high values actually result from the effects of surface heterogeneity (see Chapter 4) and the inclusion of local times near 14:00.

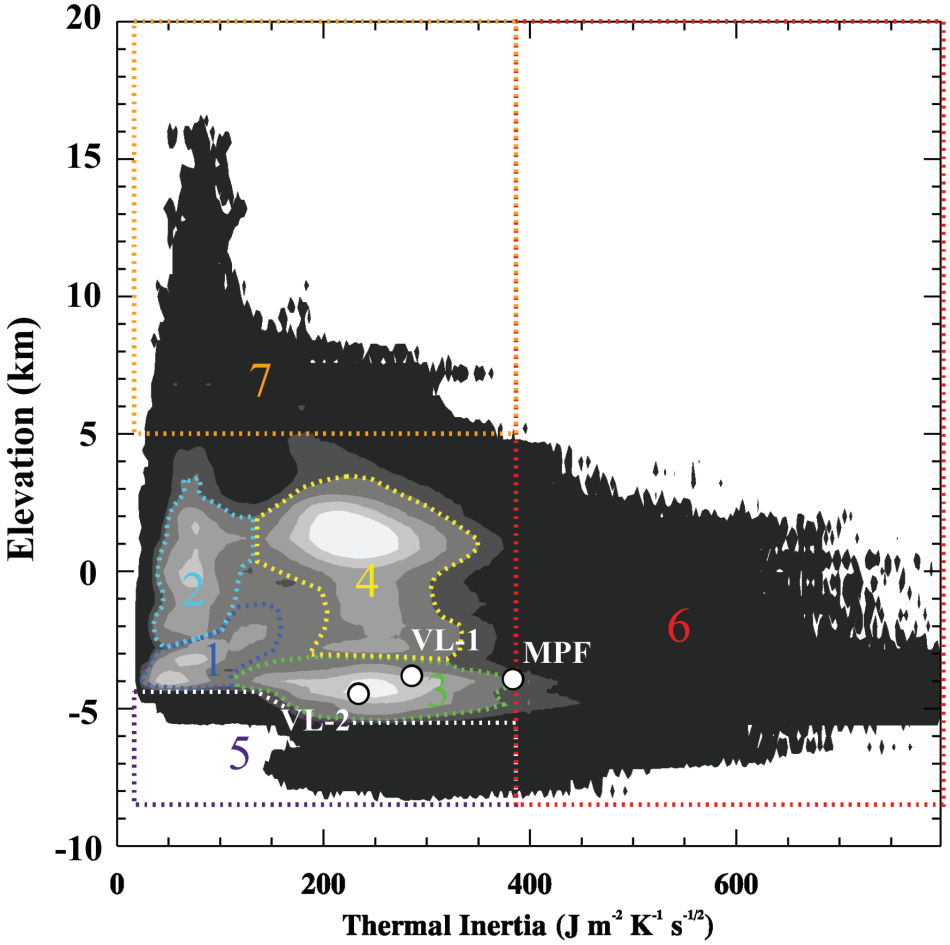

Figure 2.10 Two-dimensional histogram showing global correlation between TES nighttime bolometric thermal inertia and MOLA elevation, created using unfilled maps. Thermal inertia bin size is 3 tiu. Elevation bin size is 400 m. White areas represent no occurrences. Filled contour levels are 1, n/20, n/10, n/5, n/3, and n/2, where n = 15336.5 is the maximum in a single bin wherein each occurrence is weighted by the cosine of its latitude to account for the represented surface area. Four modes of frequent correlation are assigned as Units 1, 2, 3, and 4, with outliers assigned to Units 5, 6, and 7. Unit numbers correspond to those in Fig. 2.11 and Table 2.2.

distribution of thermal inertia is relatively uniform (i.e., high and low thermal inertia occur over a broad range of elevations). Examination of the outliers (darkest

portions of Fig. 2.10) shows that the highest thermal inertia values (> 400 tiu) only occur at relatively low elevations (< 5 km) and the highest elevations (> 10 km) only exhibit low thermal inertia (< 130 tiu). The latter is nominally consistent with low atmospheric pressure causing a reduction in bulk conductivity (Wechsler and Glaser 1965, Jakosky 1979, Bridges 1994) and the finest particles settling out and becoming trapped at high elevations (Christensen 1986a). However, a close inspection also reveals that the very lowest thermal inertia (< 30 tiu) occurs only at lower elevations (−5 – 3 km), suggesting that atmospheric pressure may not in fact be the sole factor controlling bulk conductivity and the distribution of fines at the martian surface.

We identified four major units of distinct thermal inertia and elevation characteristics associated with the modes in Fig. 2.10. These are regions of (1) low thermal inertia (24–160 tiu) and low elevation (−4.3 – −1.2 km); (2) low thermal inertia (35–135 tiu) and high elevation (−2.8 – 3.5 km); (3) high thermal inertia (115–386 tiu) and low elevation (−5.5 – −3.0 km); and (4) high thermal inertia (135–350 tiu) and high elevation (−3.0 – 3.5 km). In Fig. 2.10, we show unit boundaries for the four major units and include further subdivision of the thermal inertia–elevation outliers, which are subdivided into regions of (5) very low elevation (< −4.3 km); (6) very high thermal inertia (> 386 tiu); and (7) very high elevation (> 5.0 km). For this study, the major unit boundaries were chosen to encompass the four peaks of the global histogram while excluding the second-lowest frequency level (< 1534 points per bin) in order to provide a separation between each major unit and between the major units and the outliers. Unit bounds and their associated thermal inertia–albedo units are summarized in Table 2.2.

A global map of these thermal inertia–elevation units (Fig. 2.11) shows their spatial distribution on the surface of Mars. The major units (1–4) compose 78%

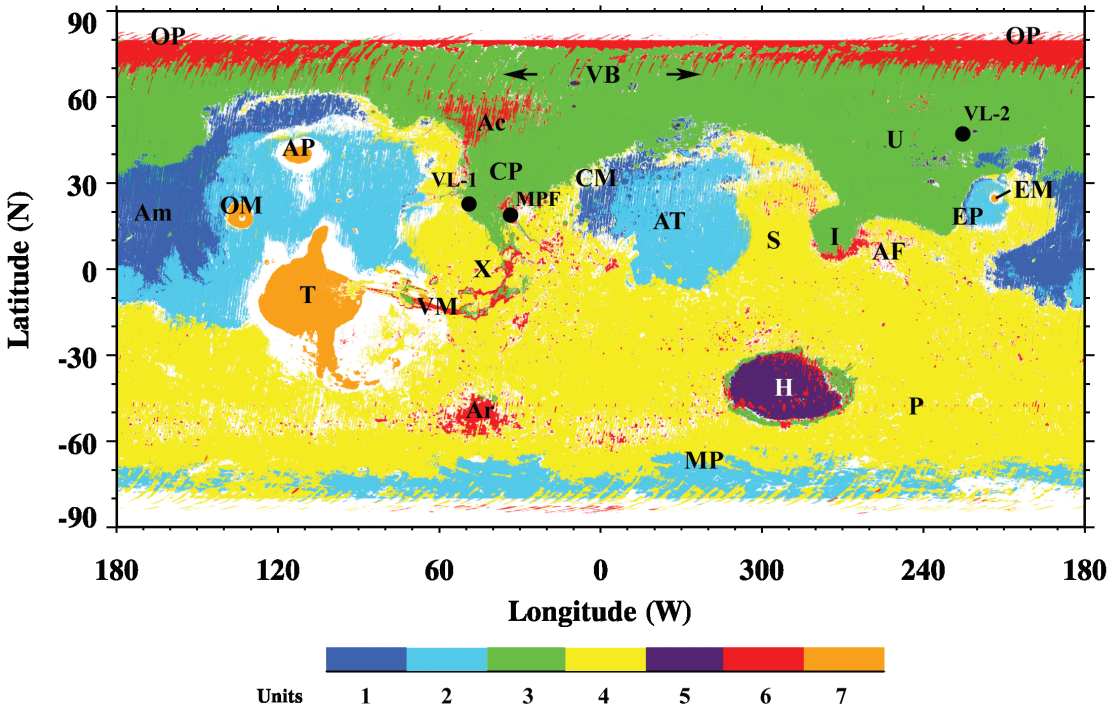

Figure 2.11 Thermal inertia–elevation unit map of Mars. Units represent thermal inertia–elevation modes in Fig. 2.10. White areas correspond to regions between unit bounds in Fig. 2.10 and to no-data areas beyond 80° latitude. See Table 2.2 for correspondence to thermal inertia–albedo units and text for discussion. Lander locations and regions discussed in the text: VL-1, Viking Lander 1; VL-2, Viking Lander 2; MPF, Mars Pathfinder Lander; Ac, Acidalia; AF, Amenthes Fossae; Am, Amazonis; AP, Alba Patera; Ar, Argyre; AT, Arabia Terra; CP, Chryse Planitia; CM, Cydonia Mensae; EM, Elysium Mons; EP, Elysium Planitia; H, Hellas; I, Isidis; MP, Malea Planum; P, Promethei Terra; OM, Olympus Mons; OP, Olympia Planitia; S, Syrtis Major; T, Tharsis; U, Utopia Planitia, VB, Vastitas Borealis; VM, Valles Marineris; X, Xanthe Terra.

of Mars' surface area. Based on thermal inertia values and correspondence with thermal inertia–albedo units (cf. Fig. 2.11 and Fig. 2.5), we interpret Units 1 and 2 (associated with Units A, C, and D) as surfaces dominated by unconsolidated or indurated fines and low density mantle material, and Units 3 and 4 (associated with Units B, C, and E) as surfaces composed of coarser-grained sediments, duricrust, rocks, and perhaps some bedrock exposures. Significant accumulations of

Table 2.2. Mars thermal inertia–elevation units

Unit	Inertia (tiu)	Elevation (km)	% Surface[a]	Inertia–albedo units[b]
1	Low (24–160)	Low (−4.3 – −1.2)	7	A, C
2	Low (35–135)	High (−2.8 – 3.5)	13	A, D
3	High (115–386)	Low (−5.5 – −3.0)	17	B, C, E
4	High (135–386)	High (−3.0 – 3.5)	41	B, C, E
5	Low–High (24–386)	Very Low (< −4.3)	1	B, C
6	Very High (> 386)	All	4	F
7	Low–High (24–386)	Very High (> 5.0)	3	A, B, C, G

[a]From the interpolation-filled unit map (Fig. 2.11).

[b]See Table 2.1.

low thermal inertia material at low elevations (Unit 1) are located in Amazonis Planitia, Cydonia Mensae, and to a lesser extent, Elysium Planitia. All of these are west of topographically elevated regions (Tharsis, Arabia Terra, and the Elysium Montes, respectively) each of which also exhibits low thermal inertia (Unit 2). This observation supports the idea that these regions may act as atmospheric dust sinks, as has been suggested by earlier observations and atmospheric models that show predominantly easterly winds at these latitudes (Christensen 1986b, Zurek et al. 1992, Kahn et al. 1992, Haberle et al. 1993). Thermophysical Unit D discussed above falls entirely within Unit 2, as is expected from its low thermal inertia and the elevated nature of the southern hemisphere. The major units of high thermal inertia (Units 3 and 4) are grossly split between north and south by the planetary dichotomy boundary, with Unit 4 extending northward into some lower elevation areas. Unit 5 is essentially confined to Hellas Planitia and therefore includes portions of thermophysical Units B and C, whereas Unit 6 is by definition equivalent to Unit F. Unit 7 contains all points above 5000 m and is thus located in Tharsis, Olympus Mons, Alba Patera, and Elysium Mons. These areas include thermophysical Units A and C and to a lesser extent, Units B and G.

2.3.3 Past landing site analysis

We now consider thermophysical data in terms of observations made at the surface from the Viking (VL-1 and VL-2) and Mars Pathfinder (MPF) landing sites. As discussed extensively in Jakosky and Mellon (2001), the relationship between in situ observations of surface properties and TES-derived thermal inertia at these sites can help us interpret surface properties at other sites for which we currently have no ground-truth observations. Here we report revised thermal inertia values (VL-1, 283 tiu; VL-2, 234 tiu; MPF, 386 tiu) and present unfilled maps

of TES-derived thermal inertia overlaid on Viking Orbiter MDIM 2.0 mosaics for each site, accompanied by representative lander image mosaics (Fig. 2.12). Registration between the Viking Orbiter images and MGS datasets was performed by manually aligning craters in the images with the MOLA-derived elevation map. Manual alignment was necessary because MOLA and other MGS data are in a planetocentric coordinate system (Smith et al. 2001a) whereas Viking MDIM 2.0 mosaics are projected in a planetographic coordinate system referenced to the IAU1991 ellipsoid and contain some positioning errors (Kirk et al. 2000), and no exact analytic transformation between the two systems is available. The thermal inertia is relatively uniform in the regions surrounding each of the Viking Landers (the higher-thermal-inertia groundtrack-aligned streak west of the VL-2 location in Fig. 2.12b is likely an artifact due to a period of higher dust opacity). The VL-1 region generally has higher thermal inertia than the VL-2 region, and some craters exhibit values slightly higher than the background level. In contrast, the MPF region shows a greater range and spatial variability of thermal inertia values, in keeping with ground-based observations of rock abundance variations (Golombek et al. 2003). At the MPF site, there are correlations between lower thermal inertia and what have been interpreted to be erosional remnants from catastrophic flooding (Baker et al. 1992), such as the large tear-drop-shaped feature southeast of the landing site (Fig. 2.12c). Additionally, several craters or portions thereof exhibit elevated thermal inertia, which may be indicative of coarse-grained intracrater deposits (e.g., Pelkey et al. 2001). The accompanying lander images show rock-strewn surfaces with varying characteristics. As reflected in these images, the VL-2 surface contains a greater frequency of large rocks than either VL-1 or MPF (Moore and Keller 1990, Golombek et al. 2003). However, a complete analysis of surface images by Golombek et al. (2003) has shown that the VL-2 overall rock abundance is lower than that of MPF, indicating a more

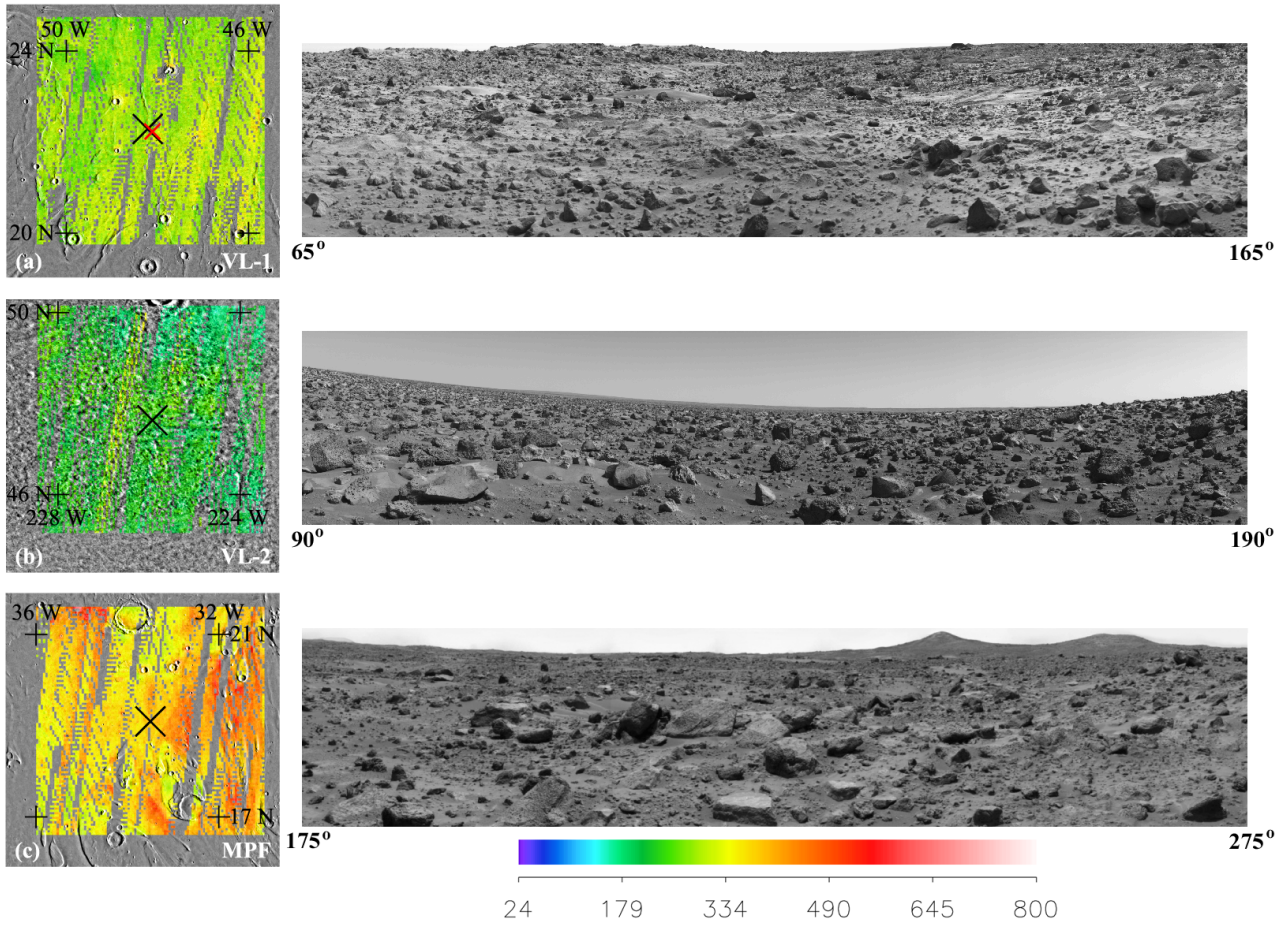

Figure 2.12 Overlay of unfilled TES-based thermal inertia map ($5^\circ \times 5^\circ$) on a Viking MDIM 2.0 mosaic (left) and panorama from the lander showing a representative 100° of azimuth (right) for each landing site. (a) VL-1 relocated from small red to large black $\times$ per Zeitler and Oberst (1999). Lander mosaic 12F180-BB4. (b) VL-2 Lander mosaic 22A252-BB4. (c) Portion of MPF Lander "Presidential Panorama" mosaic PIA01466. Thermal inertia values in tiu.

homogeneous rock distribution for VL-2.

In Table 2.3, we report TES thermal inertia and albedo, MOLA elevation, and rock abundance estimates for each landing site. Remotely sensed data are taken from unfilled maps and reported values include standard deviations for the regions surrounding each lander. Values are reported for an average of 6 $\times$ 6 map pixels ($\sim$ 18 $\times$ 18 km), giving consideration to the uncertainty in lander locations (Zeitler and Oberst 1999) and the fact that the observed radiance of any particular pixel may be affected by variable atmospheric conditions which have not been fully modeled in the calculations of thermal inertia and albedo. Thus, reporting a locally averaged value is more meaningful. Note that the thermal inertia value reported here for VL-1 (283 tiu) is about 40 tiu lower than that reported previously (320 tiu) by Mellon et al. (2000) and Jakosky and Mellon (2001). The latter estimate was based on a seasonally-limited map and used the old location for the lander rather than the revised location as determined by Zeitler and Oberst (1999). The values reported here for VL-2 (234 tiu) and MPF (386 tiu) agree well with those of Mellon et al. (2000) (230 and 380 tiu, respectively). Rock abundances in Table 2.3 are taken from Christensen (1986b), Moore and Jakosky (1989), Moore and Keller (1990, 1991), Golombek et al. (1999), and Golombek et al. (2003).

An interesting consideration is the correspondence between TES thermal inertia and rock abundance as observed from the landers. For the TES data, the VL-1 and VL-2 thermal inertia values are respectively about 100 and 150 tiu lower than that of MPF, whereas the lander-observed rock abundances are all quite similar (within 3% when including far-field estimates and outcrops). As noted by Jakosky and Mellon (2001), this miscorrelation suggests that rock abundance is not the most important factor controlling thermal inertia in these regions, an observation consistent with a similar conclusion reached by Christensen

Table 2.3. Past lander site data, mapped units, and rock abundances

Lander	TES Inertia (tiu)	TES Albedo	MOLA Elevation (m)	Mapped units Inertia vs. Albedo[a]	Mapped units Inertia vs. Elevation[b]	Rock abundance (%) IRTM[c]	Rock abundance (%) Observed[d]
VL-1	283 ± 14	0.216 ± 0.004	-3623 ± 21	C	3	14	8–16
VL-2	234 ± 11	0.238 ± 0.003	-4509 ± 09	C	3	17	14–19
MPF	386 ± 10	0.186 ± 0.003	-3695 ± 23	F	3	18	19

[a]See Table 2.1 and Figures 2.4 and 2.5.

[b]See Table 2.2 and Figures 2.10 and 2.11.

[c]From Christensen (1986b) and Golombek et al. (1999).

[d]From Moore and Jakosky (1989), Moore and Keller (1990, 1991) and Golombek et al. (2003). Low values are from near-field data. High values include far-field estimates and VL-1 outcrops.

(1986b) in a study of rock abundance and thermal inertia from Viking orbiter data. Other surface characteristics, such as the degree of induration or the particle size distribution of fines, are likely to be more important factors for determining the thermal properties of these regions and probably of a large fraction of the martian surface. In an effort to reconcile the Viking orbiter data on the distribution of rocks and thermal inertia with Earth-based radar data, Jakosky and Christensen (1986) proposed that the distribution of duricrust and variation in its degree of induration actually dominate the thermal properties of the martian surface. The lander-site data presented here is consistent with this model. However, TES resolution still allows the possibility that conditions observed from the landers (e.g., the similar rock abundances) may be local anomalies which are not evident at the 3-km scale of the TES instrument. In general, intermediate thermal inertia values such as are associated with the three past landing sites will have a nonunique interpretation, with the potential for a broad range of geological complexity.

2.4 Summary

Complete seasonal coverage now allows near-global mapping of thermal inertia at the resolution (~ 3 km) intrinsic to the MGS-TES instrument. We provide a thermal inertia map with $\sim 60\%$ coverage at $\frac{1}{20}^\circ$ per pixel between 80 °S and 80 °N latitudes and scattered coverage up to 87 ° latitude (Fig. 2.1). Global analysis of thermal inertia and albedo (Fig. 2.5) confirms the presence of three distinct thermophysical units first detailed in Mellon et al. (2000). These units are: (A) low thermal inertia and high albedo dominating continent-sized areas centered on Olympus Mons, Arabia Terra, and Elysium Mons; (B) high thermal inertia and low albedo dominating southern mid-latitudes, central Acidalia Planitia, and eastern Vastitas Borealis; and (C) high thermal inertia and intermediate albedo forming a boundary between Units A and B and covering the floor of Hellas Basin

and portions of Promethei Terra and Vastitas Borealis.

Detailed analysis of thermal inertia and albedo shows other regions characterized by specific thermophysical properties. Most notably, we identify a new unit (D) of low thermal inertia and low-to-intermediate albedo dominating the region polewards of 65 °S. Previous studies using Viking IRTM data (Vasavada et al. 2000, Paige and Keegan 1994) also observed a relative low in thermal inertia in this region, but MGS-TES results provide much greater resolution and allow us to better characterize its relationship to albedo. This unit provides an intriguing puzzle. Normally, such low thermal inertia is associated with unconsolidated, fine-grained dust, such as that believed to compose Unit A. However, the lower albedo associated with Unit D and other considerations preclude a similar composition to Unit A, so an alternative explanation is required. We consider phenomena analogous to those which produce terrestrial low-density soils such as the desiccation of ice-cemented loess (Johnson and Lorenz 2000) as the most likely candidates for explaining the observed thermophysical properties of Unit D. Alternative theories invoking a "dark dust" are not in keeping with the homogenization of fines expected to occur during global dust storms.

Subdivision of the remaining thermal inertia–albedo parameter space yields three additional units: (E) very low albedo regions in central Syrtis Major and northern Acidalia Planitia; (F) very high thermal inertia regions in Argyre Basin, the rim of Hellas Basin, Valles Marineris, Chryse Planitia, northern Acidalia, southern Isidis Planitia, and Vastitas Borealis; and (G) very high albedo regions, some showing associations with the low thermal inertia ramparts of Olympus Mons and the Tharsis Montes, and others covering sparse portions of higher thermal inertia regions in Shalbatana, Simud, and Tiu Valles and Amenthes Fossae. The Vastitas Borealis portion of Unit F, which covers much of the region polewards of 65 °N, has TES-derived thermal inertia values that are highly variable between

adjacent orbital tracks as demonstrated by the streaks seen on the global map (Fig. 2.1). These high values are inconsistent with results obtained from Viking data (Vasavada et al. 2000, Paige et al. 1994), although the extremely high thermal inertia values (pink to white in Fig. 2.1) do correlate with exposed water ice of the residual polar cap and its outliers. We attribute the high thermal inertia streaks in this region to an artifact likely produced by time-of-day sampling limitations in our thermal inertia derivation algorithm.[5]

Global analysis of thermal inertia and elevation shows a 4-mode distribution, with high and low thermal inertia occurring across a broad range of elevations. However, the highest elevations exhibit only low thermal inertia and the highest thermal inertia occurs only at lower elevations. Also, the lowest thermal inertia occurs only at lower elevations (-5 to +3 km), an observation which contradicts the historically popular concepts of gas pressure controlling bulk conductivity and trapping of the finest particles at high elevations.

Local analysis of thermal inertia and albedo shows that the locations of the Viking Landers are contained within Unit C (high thermal inertia and intermediate albedo), which has been interpreted as characterized by indurated fines (duricrust) with some surface rocks (Mellon et al. 2000). This interpretation is consistent with the occurrence and abundances of duricrust and rocks observed at each landing site. Values of thermal inertia and albedo over the Mars Pathfinder site place it near the lower boundary of Unit F (very high thermal inertia) with lower albedo than at the Viking sites, which is nominally in keeping with the high rock abundances observed by the lander at the surface. However, there are indications that other factors such as the degree of induration and local variability in rock abundance may be important. These three sites provide an important check

[5] Subsequent analysis suggests that these high values actually result from the effects of surface heterogeneity (see Chapter 4) and the inclusion of local times near 14:00.

on our interpretation of remotely-derived thermal inertia for the thermophysical units in which they occur. We anticipate that future landers and higher-resolution observations will provide critical additional constraints on our understanding of these and other surface units.

Chapter 3

Thermal behavior of horizontally mixed surfaces

> Everything has a natural explanation. The moon is not a god, but a great rock, and the sun, a hot rock.
>
> — Anaxagoras

3.1 Introduction

A major goal of the Mars exploration program is to characterize the physical surface properties of the planet in order to provide a better understanding of the surface geology and climate, and to ensure the safety of landed spacecraft. An important element of this characterization is the estimation of the surface thermal inertia, which is typically derived from temperature observations obtained from orbit by infrared spectrometers. Methods for deriving thermal inertia (e.g., Kieffer et al. 1977, Palluconi and Kieffer 1981, Jakosky et al. 2000, Mellon et al. 2000, Fergason and Christensen 2003, Putzig et al. 2004, Section 4.2.1) generally employ results from thermal models that assume a level surface with material properties that are horizontally and vertically homogeneous for any given observation or set of co-located observations. It is widely recognized that this assumption does not accurately describe the surface of Mars on the scale of present observations (e.g., $\sim$ 3 km for the Mars Global Surveyor [MGS] Thermal Emission Spectrometer [TES] and $\sim$ 100 m for Mars Odyssey Thermal Imaging System [THEMIS]). In theory, fully incorporating a generalized heterogeneous subsurface model into an algorithm for deriving thermal inertia is possible, but the greatly increased

potential for non-unique solutions and the limitations of available computational resources have prevented the implementation of such an algorithm. It is therefore important to assess the impact of the homogeneity assumption on derived thermal inertia results, with the goal of finding ways to mitigate its effects, or even use those effects to better characterize the surface.

Observations of the surface of Mars from fixed and mobile landed spacecraft show widespread horizontal and vertical heterogeneity. The Viking landers found rock-strewn surfaces with extensive areas of duricrust veneers and drifts of unconsolidated fines (Binder et al. 1977, Mutch et al. 1977, Moore et al. 1977, 1987, Moore and Jakosky 1989, Arvidson et al. 1989, Golombek and Rapp 1997, Golombek et al. 1999, Moore et al. 1999, Golombek et al. 2003). A similar surface was observed at the Mars Pathfinder site (Smith et al. 1997, Golombek et al. 1999, Moore et al. 1999, Ward et al. 1999, Bell III et al. 2000). Mobility has allowed the Mars Exploration Rovers Spirit and Opportunity to examine a wider variety of surface features, including large bedrock exposures on crater walls, rock-strewn surfaces, and broad plains of fine-grained materials generally covered with a thin layer of hematite spherules (Soderblom et al. 2004, Golombek et al. 2005, Golombek et al. 2006). Large variations in surface slope angle and azimuth occur at crater rims, on duneforms, and within the Columbia Hills at the Gusev site (Li et al. 2006). Clearly, these surfaces are far from uniform on the scale of orbital spacecraft observations.

Indications of heterogeneity are also found in remote-sensing observations. The Viking orbiters observed the surface at various times of day, and albedo and thermal inertia were derived from Infrared Thermal Mapper (IRTM) data (Kieffer et al. 1976, 1977, Palluconi and Kieffer 1981). Observations in the solar band (0.3–3.0 μm) were used to determine albedo, while emission in a 20-μm-centered atmospheric spectral window were used to estimate surface temperatures. For

many locations, differences in temperature between the observed values and values modeled using fixed material properties were found, with the largest occurring in the afternoon. Thermal inertia and a model albedo were derived using temperatures from multiple times of day and a two-parameter curve-fitting method that assumed a surface of constant and uniform properties for any given location on the surface. A substantial difference between the model albedo and the solar-band albedo was observed, even after atmospheric effects were later incorporated into the thermal model (Hayashi et al. 1995), but no cause for these differences was identified. One possible explanation is that errors in the model albedo may occur wherever the assumption of a uniform surface is incorrect. However, the curve-fitting method forces a single value of thermal inertia for any given location, and thus any diurnal or seasonal variations in apparent thermal inertia cannot be ascertained with this multi-point method.

Through forward modeling, Jakosky (1979) assessed the theoretical effects of non-uniform surfaces on thermal inertia as determined by the multi-point method, and given an independent estimate of component characteristics such as rock abundance and layering observed from the Viking landers, he was able to estimate the effect in the data for certain locations. However, the thermal inertia values thus-derived from the IRTM data are highly non-unique with respect to potentially non-ideal surface characteristics, and in the absence of independent data, no definitive characterization of surface heterogeneity is possible. By comparing Earth-based radar observations of Mars with the thermal inertia derived from Viking IRTM data, Jakosky and Muhleman (1981) identified some surfaces with radar cross-section and thermal properties that are consistent with up to 50% rock abundance. Christensen (1986b) developed a spectral-differencing technique for IRTM observations to estimate rock abundance globally, obtaining values of 1–35% at 1° resolution, with no locations showing zero rock abundance.

In contrast to the Viking orbiters, the MGS spacecraft observes the surface from a fixed-local-time orbit (02:00 and 14:00) that infrequently repeats surface coverage, thereby necessitating the development of a single-point method for deriving thermal inertia (Jakosky et al. 2000, Mellon et al. 2000). While this single-point method also assumes a surface of constant and uniform properties, the assumption applies separately to each observation. Additionally, the albedo used in the derivation of thermal inertia is obtained from an independent source (the TES visible-band bolometer). Therefore, observations of a particular location at different seasons or times of day can and do yield different apparent thermal inertia values, thus allowing direct comparison to heterogeneous-surface modeling results (Chapter 4). Previous mappings of TES thermal inertia (Jakosky et al. 2000, Mellon et al. 2000, Chapter 2) incorporated a broad range of seasons but nighttime-only data, due to concerns about greater sensitivity to the uncertainty in albedo and larger effects of surface slopes for daytime observations. Thus, the available global thermal inertia maps, from both IRTM and TES, are essentially averages of apparent thermal inertia for the seasons and times of day observed. These results may be substantially skewed to the extent that the surface is heterogeneous and the diurnal or seasonal sampling is biased or aliased.

In summary, there is abundant evidence for widespread surface heterogeneity on Mars from both landed and orbiting spacecraft. Temperature observations and the estimates of surface material properties derived from them show effects which are likely to be related to layered surfaces or surfaces with horizontal mixtures of materials or slopes. Numerical models have now reached a level of sophistication where detailed characterization of the thermal effects of heterogeneity is achievable, and performing such a characterization is justified by the growing demand for more-detailed and higher-resolution information about martian surface properties. The availability of a large data set of apparent thermal inertia derived

from single TES observations of Mars (Chapter 4) provides further incentive for heterogeneity modeling, given that direct comparison between the TES results and those from modeling may yield constraints on surface properties that are unavailable from other sources. In the present work, we focus on understanding the thermal behavior of horizontal mixtures of materials and slopes. These forms of heterogeneity are the ones most-readily observed by spacecraft. Mellon and Putzig (2006) provide a similar study of layered-surface behavior, and in Chapter 4, we compare modeling results, from both horizontal mixtures and layered surfaces, with seasonally mapped apparent thermal inertia derived from TES observations.

In the next section, we review thermal inertia and the single-point technique used to derive it as developed by Mellon et al. (2000) and as modified in Chapter 4, and we discuss the details of our mixed-surface modeling method. In section 3.3, we present our numerical modeling results for idealized surfaces containing material and slope mixtures, characterizing their diurnal and seasonal effects on temperature and apparent thermal inertia. We conclude with a summary of our results and their implications for the interpretation of apparent thermal inertia as derived from spacecraft data.

3.2 Background and methodology

The thermal behavior of the martian surface can be represented as a boundary condition on the thermal diffusion equation, where radiative loss to space is balanced by subsurface conduction and heat flux due to insolation (F_{SUN}), downwelling atmospheric radiation (F_{IR}), and seasonal CO_2 condensation ($F_{\mathrm{CO_2}}$):

$$\epsilon\,\sigma\,{T_{\mathrm{S}}}^4 = I\sqrt{\frac{\pi}{P}}\left.\frac{\partial T}{\partial Z'}\right|_{Z'=0} + F_{\mathrm{SUN}} + F_{\mathrm{IR}} + F_{\mathrm{CO_2}}\,, \tag{3.1}$$

where ϵ is the emissivity of the surface or CO_2 frost if present, σ is the Stefan–Boltzmann constant, T_{S} is surface temperature, I is thermal inertia, P is the

diurnal or seasonal period, T is subsurface temperature, and Z' is depth normalized to the thermal skin depth δ. The thermal skin depth is the e-folding depth of the subsurface diurnal or seasonal thermal wave given by

$$\delta \equiv \frac{I}{\rho\, c} \sqrt{\frac{P}{\pi}}\,, \tag{3.2}$$

where density ρ and heat capacity c are bulk material properties of the near-surface layer. From the subsurface conduction term—the first term on the right in Eq. 3.1—it is evident that thermal inertia is the key material property controlling diurnal surface temperature variations. Thermal inertia is defined as a combination of bulk thermal conductivity k, density, and heat capacity:

$$I \equiv \sqrt{k\, \rho\, c}\,. \tag{3.3}$$

For typical geological materials under Mars surface conditions, conductivity tends to dominate thermal inertia (Wechsler et al. 1972, Jakosky 1986) and is controlled primarily by physical properties, such as particle size and porosity, within the top few centimeters of the subsurface. In general, unconsolidated fines will have low values of thermal inertia, indurated dust (duricrust) and sand-sized particles will have intermediate values, and rocks and exposed bedrock will have high values.

For observations made from orbit, the surface temperature of any given location within the instrument's field of view is controlled by a composite mixture of different surfaces, which may contain an assortment of geological materials and slope facets. In the case of material mixtures where the components are evenly distributed both horizontally and vertically on scales much smaller than a thermal skin depth, the bulk thermal inertia will differ fundamentally from that of either component (Jakosky 1986) and the surface will not demonstrate diurnally or seasonally variable apparent thermal inertia. For macroscopic mixtures where

the material properties vary at larger scales, the components may have different temperatures relative to one another at any given time of day, and the radiance observed by an orbiting instrument will be a composite of the radiances from each component. Assuming unit emissivity, one may approximate the effective surface temperature T_{S_e} from component surface temperatures T_{S_i} by performing a linear mix of the emitted flux given by the Stefan–Boltzmann function (left side of Eq. 3.1, with $\epsilon = 1$):

$$\sigma \, {T_{\mathrm{S}_e}}^4 = \sigma \sum_i A_i \, {T_{\mathrm{S}_i}}^4 , \tag{3.4}$$

where A_i is the fractional area of the ith surface component. The apparent thermal inertia derived from such composite temperatures may be expected to vary with time of day and season, due to the nonlinear relationship between temperature and thermal inertia given in Eq. 3.1. In the context of relating surface observations of rock abundance to orbital observations of thermal inertia, Golombek et al. (2003) used this approximation to model the variation of surface temperature and apparent thermal inertia for idealized surfaces containing mixtures of rocks and fines. In their model, they represented the surface temperatures with IRTM 20-μm-band-equivalent spectral temperatures. Their results showed a systematic, nonlinear relationship between rock abundance and apparent thermal inertia for a single time of day and season.

In our consideration of the thermal behavior of horizontally mixed surfaces, we obtain bolometric temperatures for each model component and find effective bolometric surface temperatures using Eq. 3.4. We then derive the apparent thermal inertia for the mixed surface from those temperatures. In general, mixed-surface bolometric and spectral temperatures, and the values of apparent thermal inertia derived from them, will differ from one another because the two techniques of mixing radiance will sample different portions of each component's

Planck radiance spectrum and the relative contributions of the components differ with wavelength. While their specific values may differ, the general behavior of the two techniques is similar (see Section 3.3.4). These differences can become important when comparing model and data results in detail. The bolometric apparent thermal inertia modeling results presented in Section 3.3.4 are appropriate for comparison to results obtained from the TES bolometer (e.g., Mellon et al. 2000, Chapters 2 and 4).

The mixed-surface model temperatures used in the present work are created from a numerical thermal model of the martian near-surface and atmosphere (see Chapter 4), which implements the thermal-diffusion boundary condition given in Eq. 3.1. This thermal model was modified from that of Mellon et al. (2000) which extended previous work by Jakosky (1979), Pollack et al. (1990), and Haberle and Jakosky (1991). Mellon et al. (2000) describe the method used here to derive thermal inertia from bolometric temperatures. In summary, a lookup table of temperatures for intervals of time of day, season, latitude, surface pressure, dust opacity, albedo, and thermal inertia is generated using the thermal model. Input temperatures are correlated with other data and interpolated through the lookup table to find the best-fitting thermal inertia.

In an effort to characterize more extreme surfaces, we expanded the lookup table to allow thermal inertia values in the range of 5–5000 tiu and surface pressures in the range of 0.8–15.0 mbar (see Chapter 4). For that analysis, we also incorporated an approximate correction for slope effects. To evaluate the efficacy of the slope correction, we modified the thermal model to incorporate surface slope to first order (the calculations include corrections to incoming solar radiation for the surface incidence angle and for the slant path through the atmosphere, but not for the effects of radiation between adjacent surfaces). This modification also allows us in the present work to evaluate here the theoretical effects of sub-pixel

slope variations on apparent thermal inertia.

We use the modified thermal model described in Section 4.2.1 to calculate diurnal and seasonal bolometric surface temperatures for a suite of idealized materials and surface slopes with fixed material properties. Using (Eq. 3.4), we then determine effective surface temperatures for multi-component horizontal mixtures of these idealized components. The effective temperatures are interpolated through the same lookup table as was used for TES data processing (see Chapter 4) to obtain bolometric apparent thermal inertia values for the multi-component mixed surfaces. Figure 3.1 shows an example of diurnal temperatures for four model surfaces representing sand, rock, an intermediate material, and a 50:50 mixture of sand and rock created using the Stefan–Boltzmann-function mixing method. Relative to the other surfaces, the sand surface shows much greater diurnal amplitude of surface temperature, is cooler at night, and is warmer during the day. For the surfaces with fixed thermal inertia (curves R, N, and S), the time of day at which the peak temperature occurs is later with higher thermal inertia and the curve intersection points are not coincident. For the mixture (curve M), the peak temperature occurs at the same time as that for the sand surface and all three curves intersect at the same times. When the temperature of the mixed surface falls between that of the sand and intermediate material (e.g., 0:00–6:00), the associated apparent thermal inertia will be less than that of the intermediate material; when between the rock and intermediate material curves (e.g., 13:00–16:00), an apparent thermal inertia greater than that of the intermediate material will be derived

3.3 Results and analysis

We characterize the surface temperature behavior and the corresponding apparent thermal inertia that would result from a series of material and slope mix-

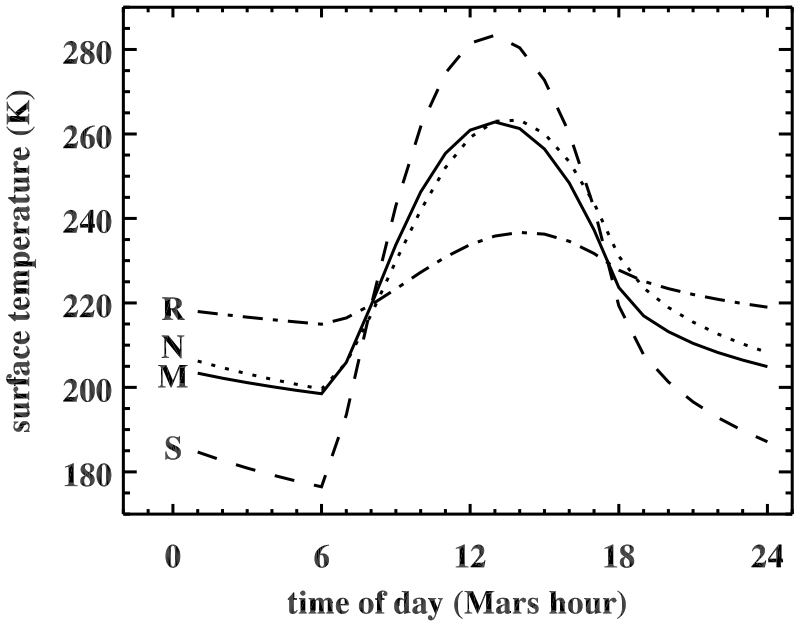

Figure 3.1 Diurnal temperature for model surfaces of (S) sand with $I = 223$ tiu, (R) rock with $I = 2506$ tiu, (N) an intermediate material with $I = 629$ tiu, and (M) a horizontal 50:50 mixture of sand and rock. All surfaces are at 30 °S, $L_S = 178$, 5 mbar, and zero dust opacity. The effective temperature of the mixture is computed from an area-weighted linear mixing of the Stefan-Boltzmann function for each component (Eq. 3.4) and will yield different values of apparent thermal inertia at various times of day (Fig. 3.2). The intermediate material properties were chosen to closely approximate the temperature curve for the mixture, and differences between curves N and M cause variations in apparent thermal inertia.

tures, focusing on the diurnal and seasonal signature for latitudes between 75 °S and 75 °N. Material components representing dust, sand, duricrust, and rock with fixed values of thermal inertia and albedo were considered (Table 3.1). Thermal inertia was chosen at representative lookup-table nodal values for each component. This choice minimizes interpolation errors when deriving apparent thermal inertia and serves as a check on the accuracy of the interpolation algorithm. The dust and sand values (56 and 223 tiu, respectively) were chosen to correspond to nightside global modal values (see Fig. 4.8). The lookup table contains only three nodes of albedo (0.15, 0.25, and 0.35). Thus, albedo values were chosen at global modal values (0.16, 0.23, and 0.26; see Fig. 2.4), rather than on nodes, to

Table 3.1. Model surface materials

Material	Thermal inertia (tiu)	Albedo
dust	56	0.26
sand†	223	0.16
duricrust	889	0.23
rock	2506	0.16

†Material used for slope mixtures.

be more representative of martian surface properties. Sub-pixel slope effects were investigated assuming uniform material properties (sand), generally with one surface component at zero slope and the other dipping at a fixed angle and azimuth. Model output is produced for each Mars hour every 8th sol throughout the martian year. For diurnal analysis, we chose seasons which are representative of either average or extremes of behavior, generally near the equinoxes (L_S = 0, 180) or solstices (L_S = 90, 270). For seasonal analysis, we focus on results at 02:00 and 14:00 local times, which correspond to the TES observation times for the nightside (southbound) and dayside (northbound) legs of the MGS orbit. These times are also representative of typical day–night differences. See Table 3.2 for a summary of model analysis parameters.

3.3.1 Two-component material mixtures

To characterize the thermal behavior of material mixtures, we modeled six combinations of two-component surfaces, using properties representative of dust, sand, duricrust, and rock. We investigated the diurnal and seasonal variation of surface temperature, the corresponding apparent thermal inertia, and the effects on their behavior due to changes in mixture components, mixing ratio of components, and latitude. Diurnal and seasonal trends are qualitatively similar for

Table 3.2. Model analysis parameters

Parameter	Analysis values	Fixed value(s) when others are varied for mixtures of: Materials	Slopes
time of day	every Mars hour	02:00, 14:00	02:00, 14:00
season	every 8th sol	$L_S = 178$	$L_S = 268$
mixing percentage	10, 30, 50, 70, 90	50	50
latitude (°N and °S)	0, 15, 30, 45, 60, 75	30 °S	0 °
slope angle (°)	0, 1, 5, 10, 45, 90	0	10
slope azimuth (°E of N)	0, 45, 90, 180, 270	0	0, 90

the different material mixtures, so we present examples with fixed components using mixtures of sand and rock to demonstrate the behavior of material mixtures in general. The equator experiences asymmetric seasonal cycles because of the orbital eccentricity of Mars, so we chose material mixture examples with fixed latitude at 30 °S. When examining other effects, a fixed mixing ratio of 50:50 is assumed.

Figure 3.2 shows diurnal and seasonal surface temperatures and the corresponding apparent thermal inertia for a 50:50 mixture of sand and rock at 30 °S. Spurious extremes of apparent thermal inertia (outlying purple points) occur near dawn and dusk due to the inherently non-unique nature of the relationship between thermal inertia and temperature at these times (see curve intersections in Fig. 3.1). Temperatures are also changing rapidly and temporal under-sampling in the lookup table may result in large interpolation errors. Diurnally, the mixed-surface apparent thermal inertia exhibits large ($\sim$ 800 tiu) changes, decreasing rapid at dawn and dusk and increasing gradually during the intervening hours, both at night and during the day. At dawn and dusk, the lower-thermal-inertia sand heats and cools much more rapidly than the higher-thermal-inertia rock,

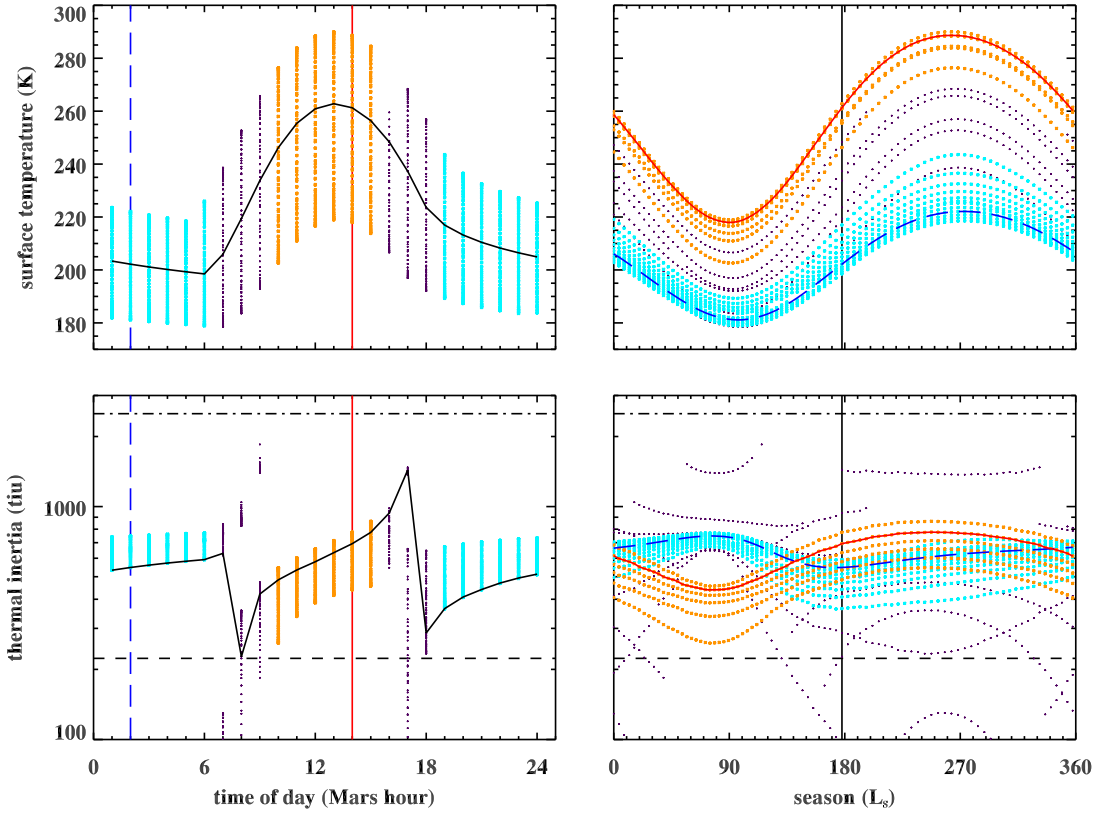

Figure 3.2 Diurnal (left) and seasonal (right) surface temperature (top) and apparent thermal inertia (bottom) for a model surface with a 50:50 mixture of sand (223 tiu) and rock (2506 tiu) at 30 °S. Each panel shows modeled values for 24 times of day and 84 seasons superimposed as individual points. Diurnal curves for $L_S = 178$ are shown in solid black and correspond to the solid curve in Fig. 3.1. Nighttime points are shown in light blue with dashed blue seasonal curves for 02:00. Daytime points are shown in orange with solid red seasonal curves for 14:00. Points near dawn and dusk (07:00–09:00, 16:00–18:00) are shown in purple. The apparent thermal inertia is found by interpolating the effective temperatures for the mixture through a lookup table. Temperatures at dawn and dusk are not uniquely related to thermal inertia (see Fig. 3.1) and may therefore result in unrealistic or multiple solutions, leading to the large diurnal thermal inertia excursions at those times.

and its contribution to the radiance becomes relatively more important, thereby reducing the apparent thermal inertia of the mixture. During subsequent hours, the contribution to the radiance from the higher-thermal-inertia rock, which acts like a thermal battery, becomes increasingly important. Seasonally, the waxing and waning of insolation modifies the overall influx of heat to the surface, and the

relative influence of each component material on the nighttime and daytime radiance varies with season. Near the winter solstice ($L_S = 90$ at this latitude) when temperatures and their diurnal fluctuations are lower, the radiance contribution from the rock becomes more important at night and less important during the day, thereby raising the overall apparent thermal inertia at night and lowering it during the day. Conversely, temperatures and their fluctuations reach a maximum near the southern summer solstice ($L_S = 270$), and the radiance contribution from the sand is relatively higher at night and lower during the day, resulting in the apparent thermal inertia for the mixture becoming lower at night than it is during the day. The seasonal variation is asymmetric due to the eccentricity of the Mars orbit. The apparent thermal inertia behavior displayed in Fig. 3.2, including the diurnal and seasonal cycling, the rapid changes at dusk and dawn, and the seasonal mirroring of daytime and nighttime trends, are qualitatively typical of all material mixtures which we examined.

In Fig. 3.3, we compare the diurnal and seasonal variations in apparent thermal inertia which are associated with six different two-component material mixtures. The diurnal curves all show rapid decreases at dawn and dusk and a more gradual trend of increasing values during the intervening hours. The rate of increase is greater for mixtures with higher thermal contrast (difference of component thermal inertia values), most noticeably during the day (e.g., compare diurnal DR and SC curves). Unlike the others, the duricrust–rock mixture (CR) shows a trend of decreasing apparent thermal inertia in the mid-morning (09:00-12:00). In this case, both components have very high thermal inertia and heat up relatively slowly, causing the reduction of the mixture apparent thermal inertia due to the influence of the lower-thermal-inertia duricrust to extend over a period of several hours. Seasonally, the variations of apparent thermal inertia for the various mixtures appear to have broadly similar characteristics, apart from

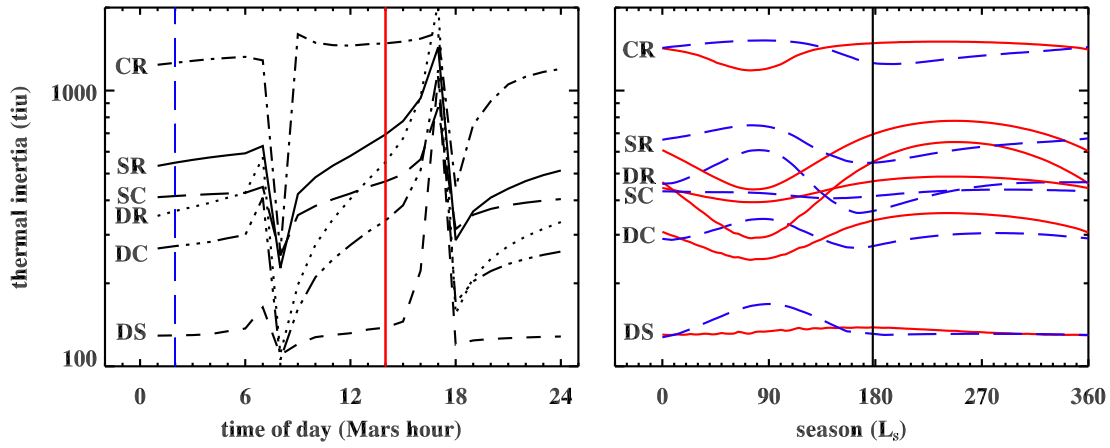

Figure 3.3 Diurnal (left) and seasonal (right) apparent thermal inertia for six model surfaces with two-component 50:50 mixtures of (DS) dust and sand, (DC) dust and duricrust, (DR) dust and rock, (SC) sand and duricrust, (SR) sand and rock, and (CR) duricrust and rock at 30 °S, $L_S = 178$, and local times 02:00 (dashed blue) and 14:00 (solid red). SR curves correspond to those in Fig. 3.2. Larger diurnal and seasonal variations occur for mixtures with components having larger thermal contrasts (e.g., compare SC and DR curves). See Table 3.1 for component properties.

their differences in mean value and in the amplitude of variation, at least when nighttime and daytime curves are compared separately. However, when one considers these curve pairs together, it is evident that each mixture shows distinct behavior. The differences between night and day values, the seasons at which those differences have extrema, and—for some mixtures—the seasons at which night and day curves intersect, are all unique. These diagnostic features, together with the diurnal trends, represent a potential means of discriminating between model types, which may prove to be an important element of constraining the heterogeneity of real planetary surfaces where similar behavior is found in remote sensing data. For real surfaces, finer diurnal sampling may be required in order to distinguish surfaces with similar seasonal behavior. For example, the seasonal curves for surfaces of sand and rock (SR) and of dust and rock (DR) in Fig. 3.3 show similar behavior, which might be construed as representing two surfaces of

sand and rock with differing mixing ratios (discussed further below). However, their diurnal behavior is distinct, with the surface of dust and rock showing more rapidly increasing apparent thermal inertia than would be expected for a surface of sand and rock.

Figure 3.4a shows the seasonal variations in apparent thermal inertia that occur for five different mixing ratios of a two-component sand–rock mixture. Changes in the mixing ratio cause the mean apparent thermal inertia to shift toward the value associated with the increasing component fraction. For increasing fraction of the component with high thermal inertia, the amplitude of the seasonal variation increases. Additionally, there is a slight increase in the range of seasons near the winter solstice ($L_S = 90$ here) at which the apparent thermal inertia is higher at night than during the day. Figure 3.4b shows the difference of apparent thermal inertia at individual times between opposing seasons ($L_S = 253$ and $L_S = 71$) near the seasonal extrema. This figure shows that the sign and relative magnitude of the differences as observed in Fig. 3.4a for 02:00 and 14:00 extend to other times, with larger magnitudes at earlier times of day and night. Figure 3.4c shows the absolute amplitude of seasonal variation at individual times of day, without regard to specific seasons. The increase of seasonal amplitude and mean value of apparent thermal inertia with increasing fraction of higher-thermal-inertia component, as identified in Fig. 3.4a, also extends to all other times of day. In general, the season and time of day at which one observes a surface of mixed materials may have a large impact on the inferred abundance of components if these effects are not taken into consideration. Additionally, adding a small amount of fines to a surface of coarser materials has a much larger thermal effect than adding a similar quantity of coarse materials to a surface of fines. This observation is in agreement with the conclusion by Christensen (1986b) that rocks—with abundances generally below 30% at 1° resolution—do not dominate

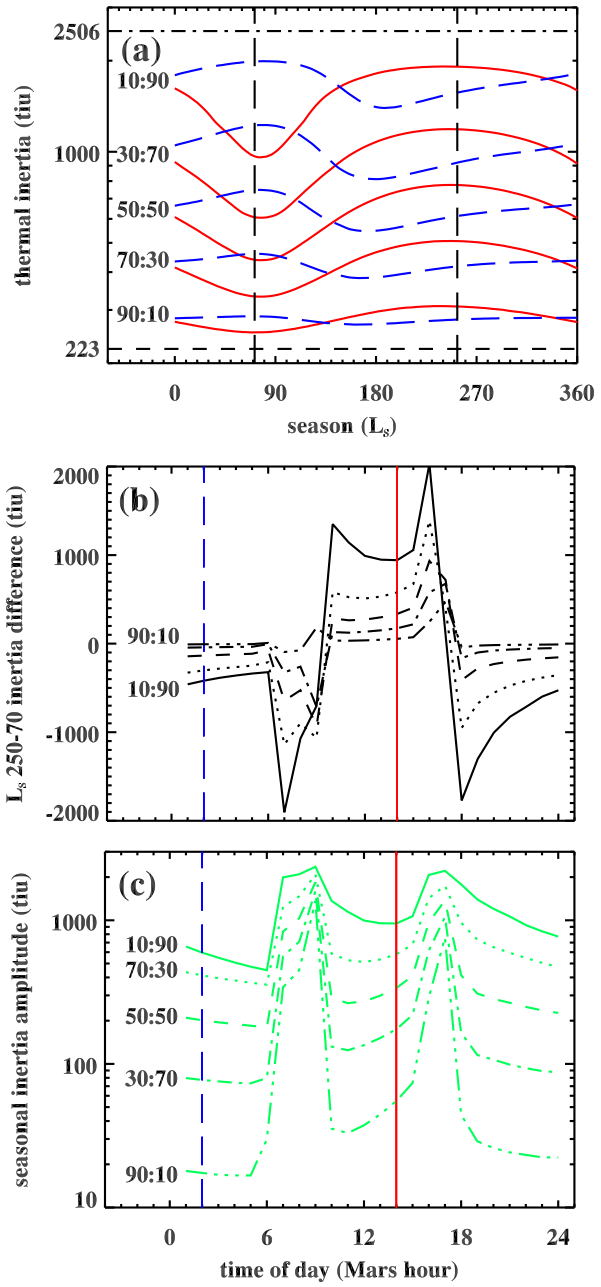

Figure 3.4 Results for model surfaces with mixtures of sand (223 tiu) and rock (2506 tiu) for five sand:rock mixing ratios at 30 °S and local times 02:00 (dashed blue) and 14:00 (solid red), showing (a) seasonal apparent thermal inertia, (b) the difference of diurnal apparent thermal inertia values between seasons $L_S = 253$ and $L_S = 71$, and (c) the diurnal amplitude of seasonal thermal inertia excursions, without regard to specific seasons. Seasonal 50:50 curves correspond to those in Fig. 3.2. Large diurnal changes near dawn and dusk (07:00–09:00, 16:00–18:00) are due to non-unique thermal inertia solutions at these times of day (see Fig. 3.2 caption).

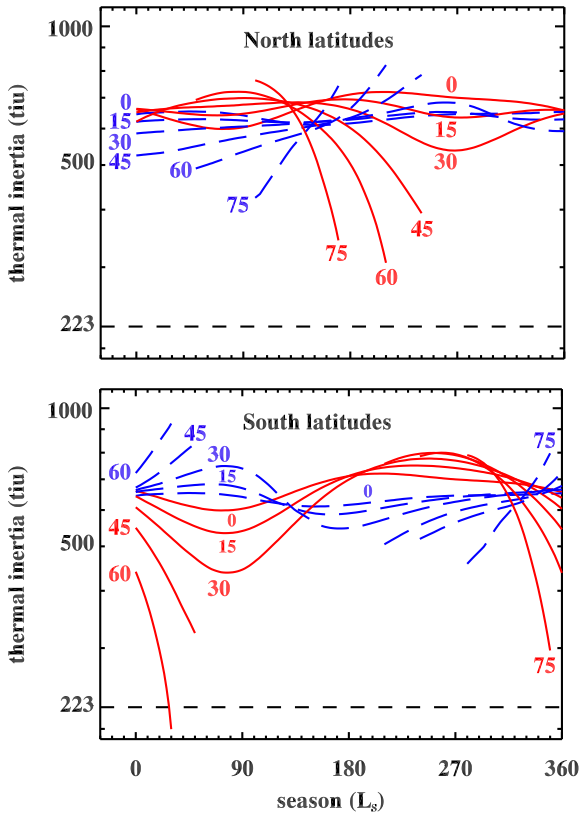

Figure 3.5 Seasonal apparent thermal inertia for model surfaces with a 50:50 mixture of sand (223 tiu) and rock (2506 tiu) for every 15 ° of latitude in the northern and southern hemispheres at local times 02:00 (dashed blue) and 14:00 (solid red). Curves for 45–75 ° latitude are seasonally limited due to the occurrence of seasonal CO_2 frost. 30 °S curves correspond to those in Fig. 3.2. N–S symmetry is distorted due to the orbital eccentricity of Mars.

the thermal inertia on Mars.

Latitudinal effects on apparent thermal inertia variations of a sand–rock mixture are shown in Fig. 3.5. Poleward of about 35–40 ° latitude, CO_2 frost covers the ground seasonally, thereby restricting the range of seasons available at higher latitudes for calculating the thermal inertia of the surface. With increasing latitude in each hemisphere, the amplitude of the seasonal variation in apparent thermal inertia increases, with very large changes (several 100 tiu) occurring over an increasingly limited range of seasons in more poleward regions. In the southern and low-northern latitudes, the apparent thermal inertia is greater at 02:00 than

at 14:00 for a range of seasons centered near the southern winter solstice ($L_S = 90$), with this seasonal range being larger for more southerly latitudes. Between 10 °N and 15 °N, this behavior transitions to occur near the northern winter solstice ($L_S = 270$). This latitudinal asymmetry and the larger amplitude of southern latitude variation are the result of the orbital eccentricity of Mars, which causes the planet to be 17% closer to the Sun at perihelion ($L_S = 251$) than at aphelion ($L_S = 71$) and introduces asymmetry in the duration of the seasons and the intensity of insolation. Because of the limited seasons available and the large variations in apparent thermal inertia which occur for heterogeneous surfaces in the polar regions, an assessment of surface characteristics in these locations from thermal observations would be greatly improved by incorporating a range of diurnal observation times. Depending on the latitude, the Sun may be continuously above the horizon for most of the available seasons, and the restriction of mapping to nighttime-only observations (e.g., Mellon et al. 2000, Chapter 2) limits data for these regions to marginal seasons which do not well-represent surface conditions. For mapping polar-region surface features thermally, a better choice is to group observations by local time without regard to whether the Sun is above or below the horizon (see Chapter 4).

In general, the magnitude of the effects of material mixtures on apparent thermal inertia can be very large. For example, the seasonal variations at 02:00 and 14:00 for the 50:50 sand–rock mixture at 30 °S have a nighttime seasonal amplitude of 200 tiu, a daytime seasonal amplitude of 460 tiu, and differences approaching 300 tiu, with a mean apparent thermal inertia value of 620 tiu. These 32–74% variations are many times greater than the estimated 6% uncertainty for thermal inertia derived from TES bolometer data (Mellon et al. 2000), and they exceed the 20–25% uncertainty estimates for results derived from THEMIS data (Putzig et al. 2004, Fergason et al. 2006). For a 90:10 sand–rock mixing ratio,

which is closer to the range of martian rock abundance estimates of 6–20% (e.g., Christensen 1986b, Golombek et al. 2003), the corresponding range of variations in apparent thermal inertia falls to 7–18%, which still exceeds the TES uncertainty. Surfaces of mixed materials on Mars may be expected to exhibit diurnal and seasonal variations in apparent thermal inertia similar to those examined here.

3.3.2 Sloped and level surface mixtures

We now consider the effects of sub-pixel slope mixtures on surface temperature and apparent thermal inertia. For our analysis, we chose modeled surfaces with a fixed thermal inertia of 223 tiu and albedo of 0.16, which are the values used to represent sand in the mixed-material analysis above. Both values are also near global modes for TES data (Figs. 2.4 and 4.8. In the following examples that are at a fixed latitude, we display results from the equator. Slope effects are driven predominantly by differences in the solar incidence angle with respect to the surface normal and are much less skewed latitudinally by the martian orbit eccentricity than are the mixed-material effects. However, seasonal asymmetry due to the fluctuation of insolation is an important factor in sloped-surface thermal behavior.

To illustrate the general effects of slope, we compare diurnal and seasonal temperature curves for five surfaces of uniform slope angle and azimuth in Fig. 3.6. One surface has zero slope and the others have 45 ° slope in each of the cardinal directions. Diurnally, the general effect of N–S slopes is to raise or lower the mean surface temperature and its amplitude, without affecting the time of day at which the peak temperature occurs. Whether the mean temperature is raised or lowered is highly dependent on the season and slope angle, which control the amount of insolation incident on the surface. When the temperatures are elevated, higher nighttime and lower daytime apparent thermal inertia will result, with

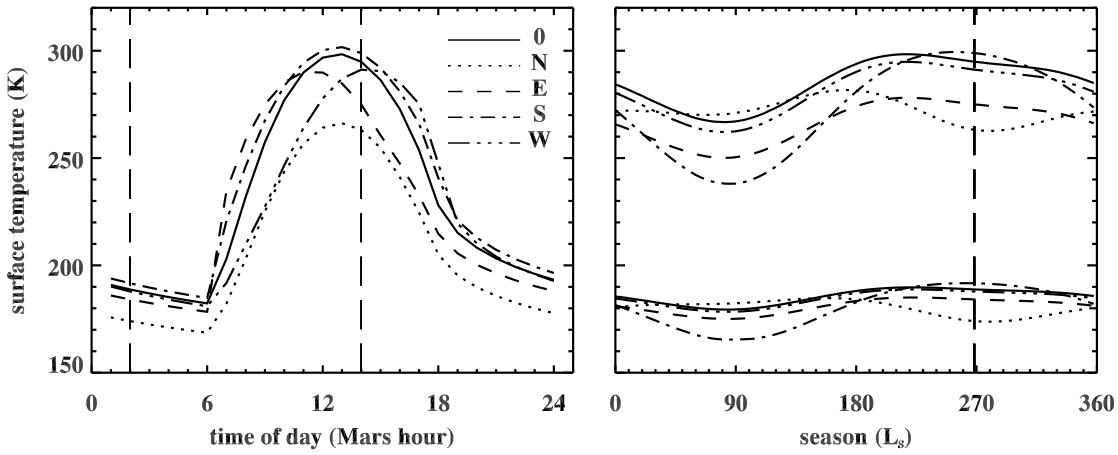

Figure 3.6 Diurnal and seasonal surface temperature for five monotonically-sloping model surfaces of sand ($I = 223$) with 0 ° slope (solid curve) and with 45 ° slope at four azimuths (0 °, 90 °, 180 °, and 270 ° [N, E, S, W]) at the equator, 5 mbar, and 0 dust opacity for $L_S = 268$ (left) and 02:00 and 14:00 local times (right). Diurnally, peak temperatures vary only in amplitude with N–S slopes and in amplitude and time of day with E–W slopes. Seasonally, temperatures vary in annual-mean value, amplitude, and season of extrema with N–S slopes and only in annual-mean value with E–W slopes.

the converse occurring for lowered temperatures. For E–W slopes, the diurnal temperature curve is skewed to earlier or later times of day and its amplitude is reduced. Eastward slopes receive relatively more heat in the morning and less in the afternoon, with the opposite being the case for westward slopes. Consequently, the apparent thermal inertia for eastward slopes will be generally lower in the morning and at night, and higher in the afternoon. For westward slopes, apparent thermal inertia will be generally higher in the morning and in the evening just after dusk, lower in the late afternoon, and may be either higher or lower in the pre-dawn hours and in the early afternoon, depending on the surface thermal inertia and the slope angle. Seasonally, N–S slopes alter the amplitude, seasons of extrema, and annual-mean value of the temperature variations whereas E–W slopes only affect their annual-mean value. The slope angle of 45 ° assumed here is quite high and was chosen to accentuate the effects on temperature. For subsequent examples

with fixed-slope components, we assume an angle of 10°, for which the apparent thermal inertia effects are more typical of sloped surfaces.

Fig. 3.7 shows the diurnal and seasonal variations of apparent thermal inertia for four surfaces with 50% of each surface level and 50% sloped at an angle of 10° in each of the cardinal directions. The associated diurnal and seasonal temperature variations (not shown) are grossly similar to those seen for material mixtures (e.g., Fig. 3.2). As with the mixed materials, large excursions of apparent thermal inertia occur near dawn and dusk (purple points) due to the inherent non-uniqueness of the relationship between thermal inertia and temperature and the potential for interpolation errors (see previous section). The apparent thermal inertia variations are otherwise quite different in character and depend strongly on the azimuthal orientation of the sloped component. Diurnally, the nighttime variations are much smaller (by a factor of ~ 5) than for mixed-material surfaces whereas the daytime variations are of comparable amplitude. Both may show either an increase or decrease with time of day, depending on the azimuth and season, and the daytime may show both for north or south azimuths. The generalizations concerning the expected apparent thermal inertia behavior of monotonically sloped surfaces based on our examination of diurnal temperature curves in Fig. 3.6 also apply to these mixed surfaces containing a component with the corresponding slope azimuth. Seasonally, surfaces with north- or south-facing slope components show apparent thermal inertia variations with much larger amplitude than for those with east- and west-facing slope components. The variations for surfaces containing north- and east-facing slope components are seasonally and diurnally mirrored, respectively, by those with south- and west-facing slopes, with extrema near the solstices ($L_S = 90, 270$). As might be expected, we found that results for a sloped-component azimuth of 45° (not shown) are intermediate between those for north and west azimuths, with extrema at the solstices and a

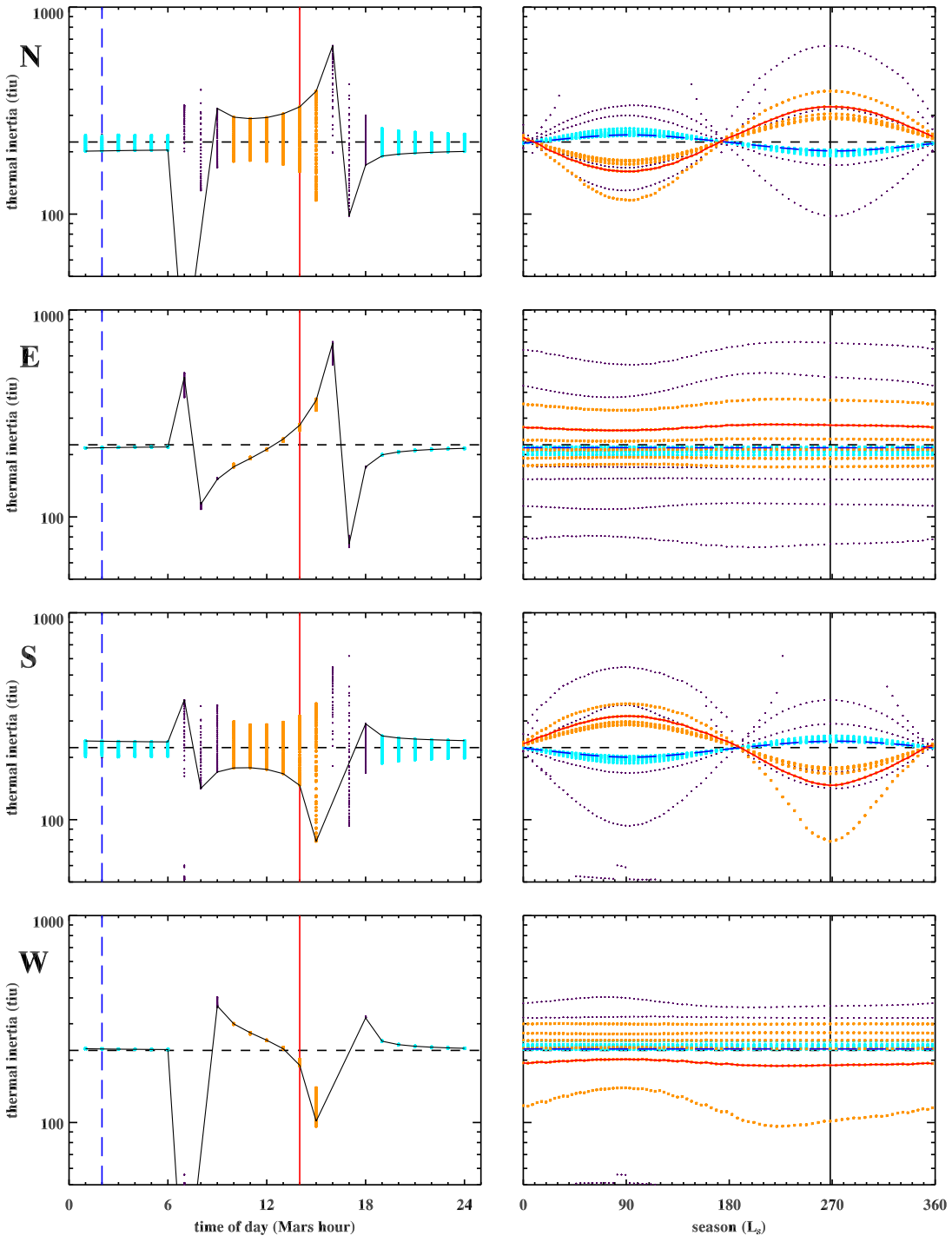

Figure 3.7 Diurnal and seasonal apparent thermal inertia for model surfaces of sand (223 tiu) with 50% level and 50% sloped at 10 ° for four azimuths (0 °, 90 °, 180 °, and 270 ° [N, E, S, W]) at the equator for 24 times of day and 84 seasons. Diurnal curves for $L_S = 268$ are shown in solid black. Other colors as in Fig. 3.2. N–S and E–W symmetries are distorted due to the orbital eccentricity of Mars.

significant offset between night and day annual-mean apparent thermal inertia. The magnitude of the apparent thermal inertia variations shown here for partially sloped surfaces with a relatively low slope angle of 10 °, particularly for N–S azimuths, is comparable to that found for a 70:30 mixture of sand and rock (compare Fig. 3.4a). Thus, sub-pixel slope variations may play an important role in the apparent thermal inertia of real surfaces.

In Fig. 3.8, we present examples of variations in seasonal apparent thermal inertia with slope angle for partially sloped surfaces. For surfaces with north- or south-facing slope components, increasing the slope angle increases the amplitude of seasonal apparent thermal inertia variations and also increases the difference between the annual-mean values for day and night. Additionally, flattening of the curves with 90 ° slope occurs for the pole-facing slopes during the fall and winter in each corresponding hemisphere (L_S = 180–360 in the north and L_S = 0–180 in the south), when the sub-solar point is in the opposite hemisphere and no sunshine falls directly on the vertical slope components. During these seasons, incident energy is limited to diffuse illumination and downwelling infrared radiation from the atmosphere and CO_2 frost forms on the vertical surfaces, which remain at the condensation temperature (148 K) until the spring equinox. The southern-hemisphere winter is colder here at the equator, but the level surface warms rapidly in the daytime after the solstice (see Fig. 3.6), causing a kink near L_S = 110 in the daytime curve for the surface with a 90 ° south-facing component. In comparison to the case for N–S slope components, increases of slope angle for east- and west-facing slope components produce much smaller increases in the amplitude of the seasonal variation but similar increases in the difference between annual-mean daytime and nighttime apparent thermal inertia. Surfaces with west-facing slope components at angles of 45 ° and 90 ° exhibit higher apparent thermal inertia in the day than at night, whereas the converse is true for lower-angle west-facing slopes.

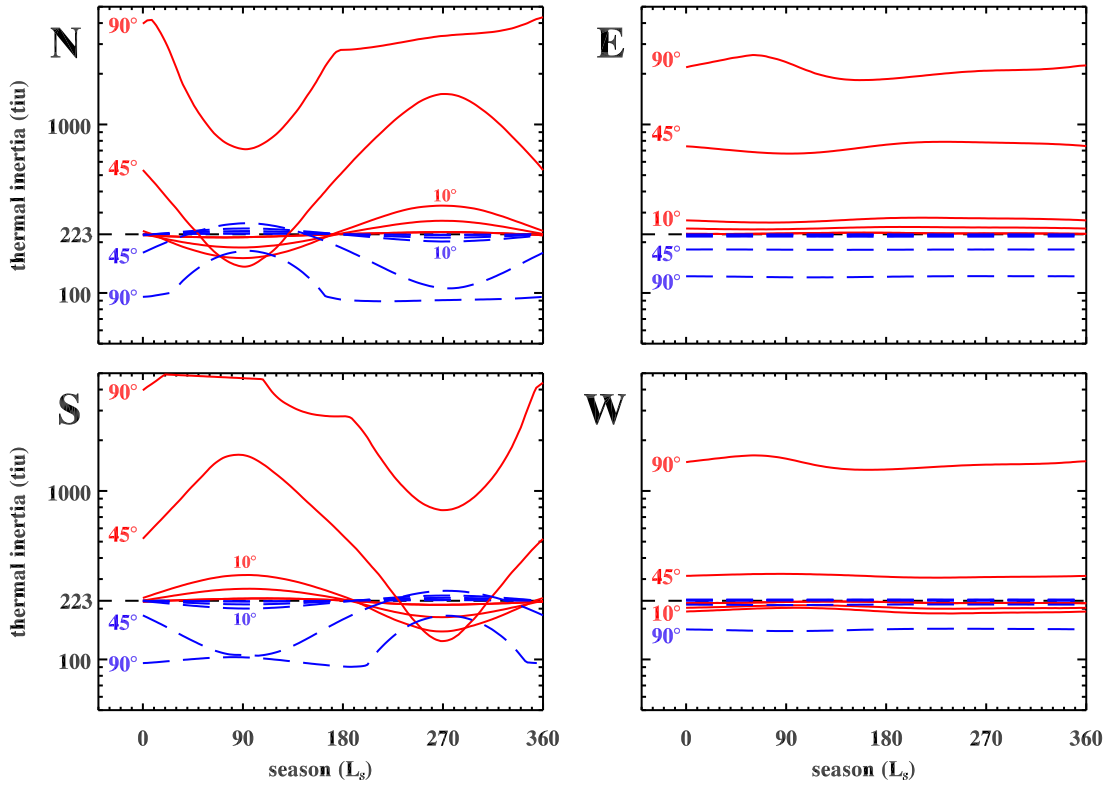

Figure 3.8 Seasonal apparent thermal inertia for model surfaces of sand (223 tiu) with 50% level and 50% sloped at angles of 1°, 5°, 10°, 45°, and 90° for four azimuths (0°, 90°, 180°, and 270° [N, E, S, W]) at the equator for local times 02:00 (dashed blue) and 14:00 (solid red). With increasing sloped-component angle, the apparent thermal inertia annual-mean value increases for N–S and E azimuths, its diurnal variation (i.e., absolute day–night difference) increases for all azimuths, and its seasonal amplitude increases for surfaces containing N–S slope components. Flattening of curves for 90° N–S slopes is due to the seasonal complete shadowing of the sloped component. Westward slopes have higher apparent thermal inertia at 14:00 than at 02:00 for high slope angles due to delayed morning insolation. 10° curves correspond to those in Fig. 3.7.

Although the higher-angle surfaces receive more insolation in the afternoon, they begin heating later in the day and are still relatively cool at 14:00 (see Fig. 3.6).

Figure 3.9 shows examples of the effects of different area percentages on seasonal apparent thermal inertia for partially sloped surfaces. For surfaces with north-facing slope components, increasing the sloped-area percentage increases the amplitude of seasonal apparent thermal inertia variations and slightly increases

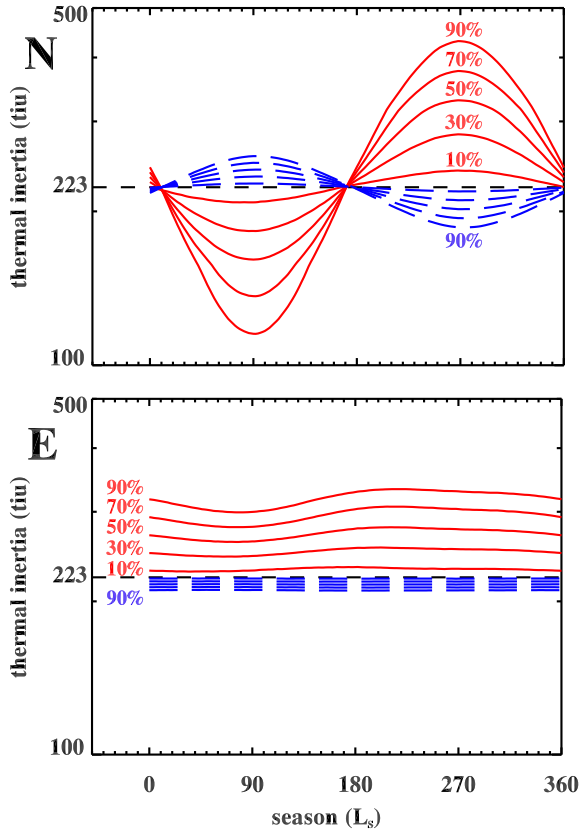

Figure 3.9 Seasonal apparent thermal inertia for model surfaces of sand (223 tiu) with one level component and one sloped component for areal percentages of the sloped component of 10%, 30%, 50%, 70%, and 90% at a slope angle of 10 ° and azimuths of 0 ° [N] and 90 ° [E] and local times 02:00 (dashed blue) and 14:00 (solid red) at the equator. 50% curves correspond to those in Fig. 3.7. With increasing sloped-component areal percentage, the apparent thermal inertia diurnal variation increases for all azimuths, its seasonal amplitude increases for surfaces containing N–S slope components, and its annual-mean value increases for surfaces containing N–S or E slope components.

the difference between the annual-mean values for night and day. In comparison, equivalent increases of sloped-area percentage for east-facing slope components produce much smaller increases in the amplitude of the seasonal variation but larger increases in the difference of day and night annual-mean apparent thermal inertia. Sloped-area-percentage effects for south-facing slopes (not shown) are similar to those for north-facing slopes, but are mirrored seasonally. West-facing-slope component effects (not shown) are similar to those for east-facing, with the

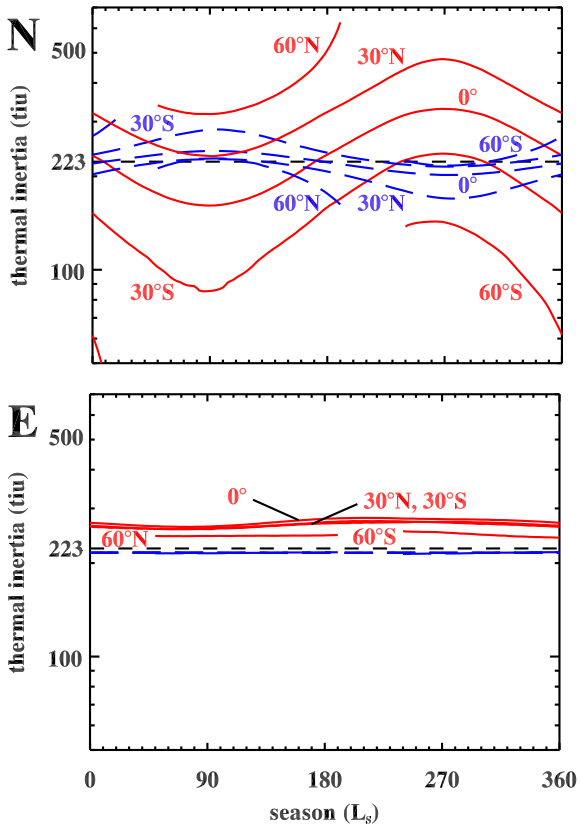

Figure 3.10 Seasonal apparent thermal inertia for model surfaces of sand (223 tiu) with 50% level and 50% sloped at an angle of 10 ° and azimuths of 0 ° [N] and 90 ° [E] at every 30 ° of latitude and local times of 02:00 (dashed blue) and 14:00 (solid red). Curves for 60 ° latitude are seasonally limited due to the presence of seasonal CO_2 frost. 0 ° latitude curves correspond to those in Fig. 3.7. With increasing north latitude, the apparent thermal inertia annual-mean value, seasonal amplitude, and diurnal variation increase for surfaces with northward slope components and its diurnal variation decreases slightly for surface with E–W slope components.

difference between the apparent and true thermal inertia having the opposite sign (daytime less than nighttime apparent thermal inertia) for slope angles less than 45 ° (see Fig. 3.8).

Examples of seasonal apparent thermal inertia variation with latitude for partially sloped surfaces are shown in Fig. 3.10. For surfaces with north-facing slope components, the day and night annual-mean apparent thermal inertia increase and decrease, respectively, with northern latitude. At latitudes further from

the equator, the amplitude of the seasonal variation in apparent thermal inertia is larger and the magnitude of the difference between day and night annual-mean values increases. For surfaces containing only east-facing slope components, very little variation in seasonal apparent thermal inertia with latitude occurs. For these surfaces, the reduction of insolation with latitude is the same for both components, and consequently, the daytime apparent thermal inertia is reduced slightly because of the reduced temperature difference between the components. Latitudinal effects for south-facing slopes (not shown) are similar to those for north-facing slopes, but are mirrored seasonally and latitudinally. Effects for west-facing slope components (not shown) are similar to those for east-facing slope components, with the difference between the apparent and true thermal inertia having the opposite sign (daytime less than nighttime apparent thermal inertia) for slope angles less than 45 ° (see Fig. 3.8).

3.3.3 Complex surface mixtures

The preceding examples of partially sloped surface mixtures show the separate effects of slope in the cardinal directions. Slopes at intermediate azimuths have effects which are essentially linear mixtures of those described above. However, real surfaces tend to have paired or azimuthally distributed slopes and the effects of such surfaces can become much more complex. For example, consider two equatorial sand surfaces, each containing opposed 45 ° slopes, with one surface having a 50:50 mixture of north and south azimuths and the other a 50:50 mixture of east and west azimuths. Diurnal temperature curves for these surfaces at three seasons (L_S = 0, 135, and 268), together with curves for corresponding monotonically sloped surfaces and a level surface, are presented in Fig. 3.11. For the N–S mixed surface, its effects and that of its separate components are all exactly the same at the equinox (L_S = 0 example). At other seasons, the

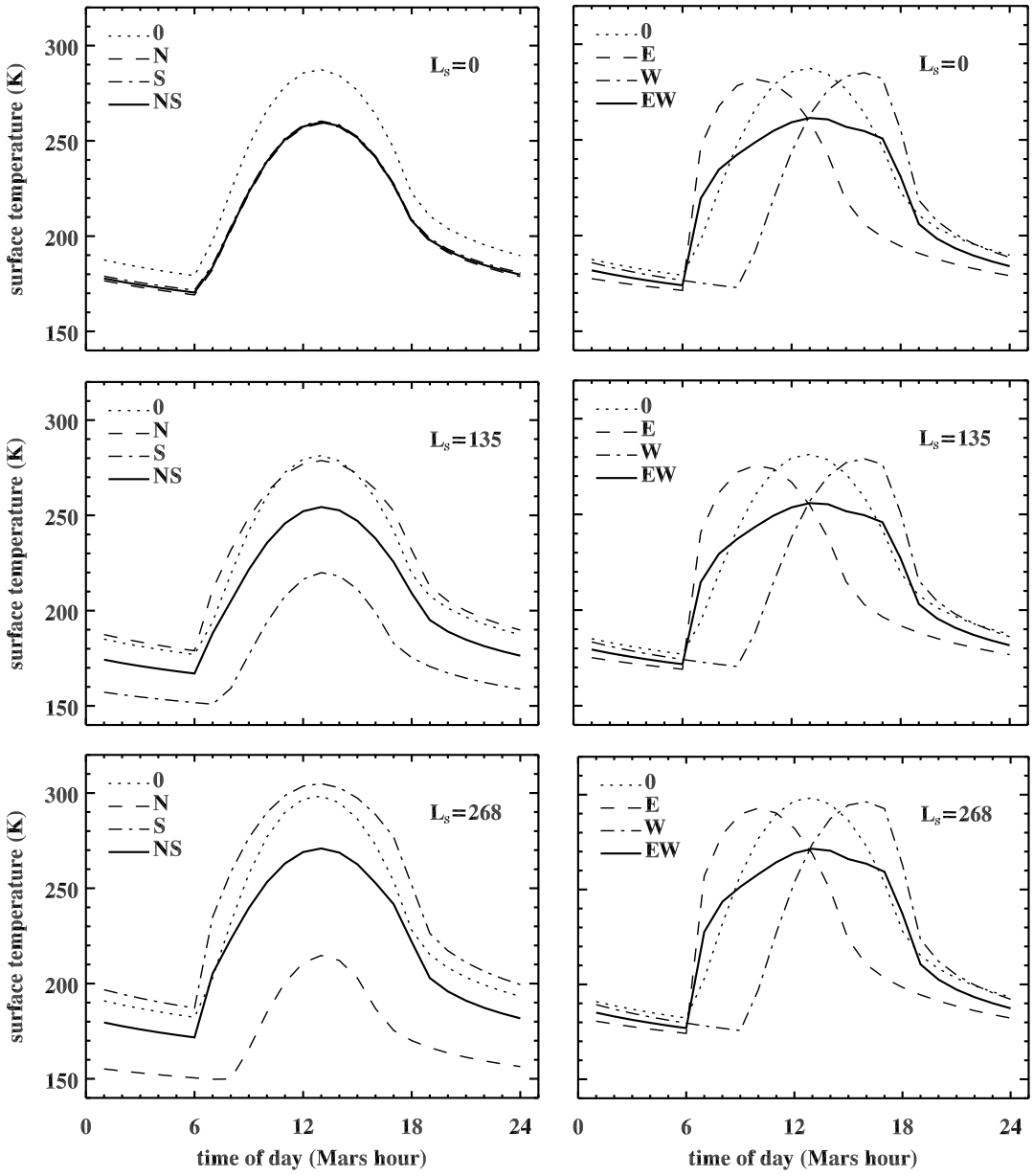

Figure 3.11 Each plot shows diurnal surface temperature for four model surfaces of sand ($I = 223$ tiu) where one surface has 0 slope (dotted curve), two surfaces are sloping monotonically at 45° (dashed and dash-dotted curves) at azimuths of either 0° and 180° (N and S; left) or 90° and 270° (E and W; right), and the fourth surface is a 50:50 mixture of the two sloped surfaces (solid curve; NS and EW). Three seasons illustrate the annual variation. All models were run at the equator, 5 mbar, and zero dust opacity. See text for discussion.

N–S mixed-surface temperature curve is more distorted relative to the level surface than either component because the variable difference in daily temperatures between the component surfaces is accentuated upon mixing (Eq. 3.4). This behavior will yield larger deviations in apparent thermal inertia. For the E–W mixed surface, the diurnal curve is severely distorted, with much lower temperatures at mid-day, elevated temperatures in the early morning and late afternoon, and lower temperatures at night, relative to the level surface. These features apply at all seasons nearly identically, with the amplitude of temperatures changing with season in equal measure for the mixed surface and its separate components. Diurnal apparent thermal inertia will vary much more for the mixed surface than for the component surfaces.

Natural surfaces also exhibit material and slope mixtures simultaneously. In Fig. 3.12, we show diurnal and seasonal apparent thermal inertia for three partially model sloped surfaces, one containing 100% sand (curves labeled S), another containing 100% rock (curves labeled R), and the third containing a 50:50 mixture of sand and rock throughout its area. For the latter surface, the curves labeled T are produced using our method of mixing temperatures and deriving thermal inertia. If such an algorithm were not available, one might consider other methods of approximating the apparent thermal inertia of the complex mixture directly from that of its single-material components. For example, the relationship between temperature and thermal inertia in Eq. 3.1 suggests a quartic approximation scheme:

$$I_{\mathrm{A}} = \left(\sum_i A_i \, I_i^{\frac{1}{4}} \right)^4 , \tag{3.5}$$

where I_{A} is the approximate complex-surface apparent thermal inertia, A_i is the fractional area of the ith component surface, and I_i is its apparent thermal inertia. The curves labeled A in Fig. 3.12 were generated from the rock and sand curves us-

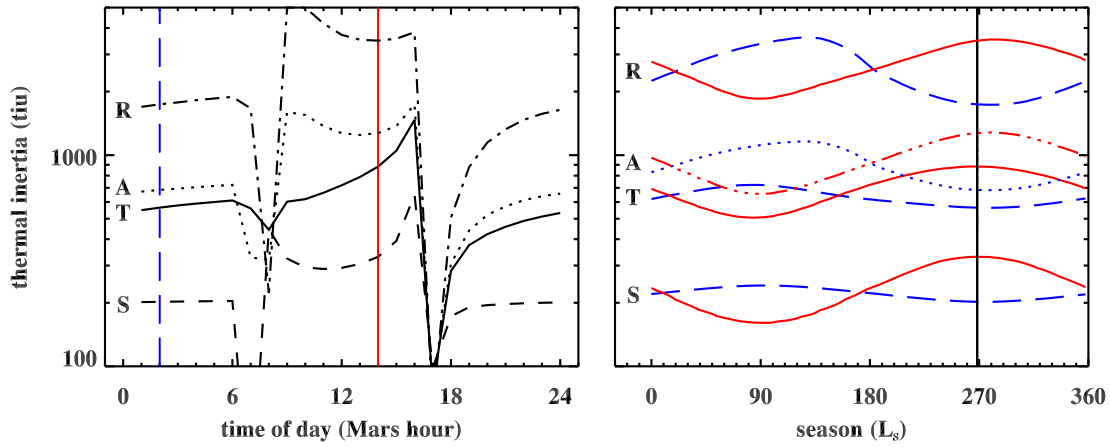

Figure 3.12 Diurnal and seasonal apparent thermal inertia for three types of mixed surfaces at the equator, where each surface is 50% level and 50% sloped at an angle of 10° and an azimuth of 0° (north). Both level and sloped portions contain (S) 100% sand (223 tiu), (R) 100% rock (2506 tiu), and (T,A) a 50:50 mixture of sand and rock. Values for the sand–rock mixture are determined (T) precisely by derivation from temperatures mixed according to the Stefan–Boltzmann function (Eq. 3.4) and (A) approximately by quartic weighting of the component values of apparent thermal inertia (Eq. 3.5). Diurnal curves are for $L_S = 178$ and seasonal curves are for local times 02:00 (dashed blue) and 14:00 (solid red). Compare to curves for 50:50 sand–rock mixture with zero slope in Fig. 3.2. The curves for the precisely mixed surface differ substantially from the others in their mean values, daytime diurnal variations, and seasons at which daytime and nighttime curves intersect.

ing this method. Both diurnally and seasonally, this approximation overestimates the apparent thermal inertia by $\sim 45\%$. Moreover, the approximate method does not capture the systematic increase of apparent thermal inertia during the daytime hours, nor the shift to earlier seasons of the intersection between the curves for 02:00 and 14:00, both of which occur using the more-precise temperature-mixing method. In short, the approximate curves (A) resemble a partially sloped surface of uniform thermal inertia which is intermediate between that of sand and rock, and any simple approximation involving direct mixing of apparent thermal inertia will have similar shortcomings.

3.3.4 Apparent thermal inertia and rock abundance

As mentioned in Section 3.2, a previous study by Golombek et al. (2003) used a technique similar to ours for approximating the effects of horizontally mixed surfaces in order to find a relationship between apparent thermal inertia and lander-observed rock abundance. They generated Viking IRTM 20-μm-band-equivalent temperatures for model surfaces containing two-component mixtures of fines and rock, and derived apparent thermal inertia for those surfaces using the thermal model and derivation algorithm of Mellon et al. (2000). Thermal inertia values were limited to a maximum of 800 tiu by the lookup table, and the rock abundance was varied from 0% to 50%. Using the modified thermal model and derivation algorithm of Section 4.2.1 which allows thermal inertia up to 5000 tiu, we extended this model to 100% rock abundance. Additionally, we explored the difference between bolometric and IRTM-20-μm-band temperatures. A comparison of our apparent thermal inertia results for three mixtures of fines and rock with corresponding results of Golombek et al. (2003) from spectral temperatures is shown in Fig. 3.13a. There is a good general agreement between all three methods. The deviation between the two spectral curves is attributable to the use by Golombek et al. (2003) of a single albedo (0.25) when deriving the apparent thermal inertia of the mixture, whereas we used an albedo that varied linearly with component fractional area between 0.25 at 0% rock abundance to 0.10 at 100% rock abundance. The divergence of our bolometric and spectral curves at intermediate rock abundance occurs because the relative magnitudes of the broadband and band-limited radiances are different for materials with different thermal properties. When comparing apparent thermal inertia values as derived from a rock abundance model with those from spacecraft data, the use of the same spectral bands is recommended. For use in rock abundance studies with

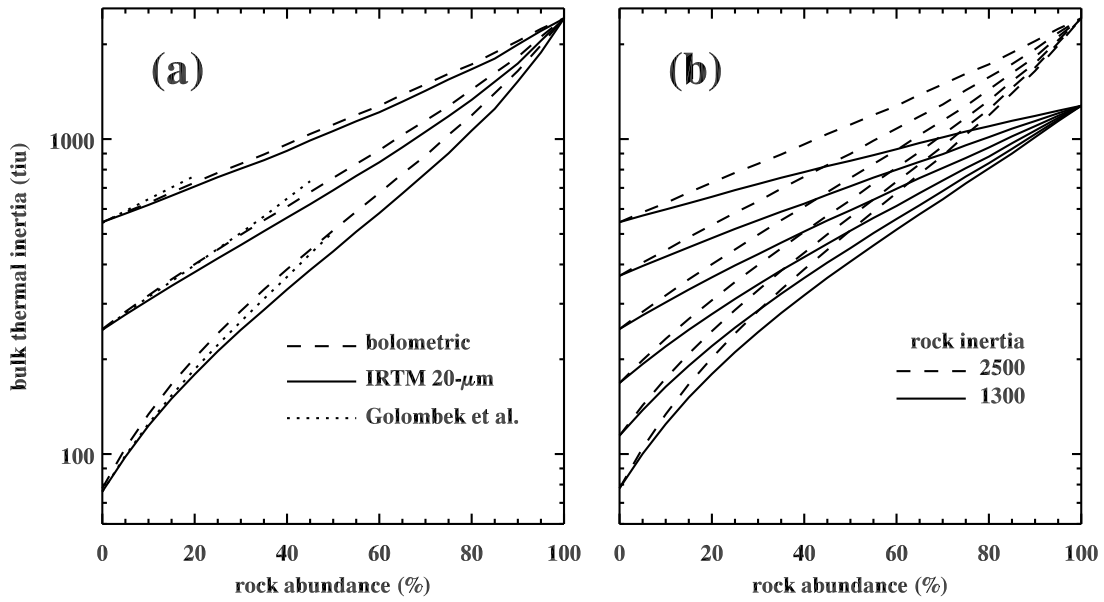

Figure 3.13 Plots of bulk apparent thermal inertia vs. rock abundance for various mixtures of materials representing fines and rocks at 10 °N, local time 05:00, L_S = 127, 6 mbar, and 0.2 visible dust opacity. Rock albedo is 0.10 and fine albedo is 0.25. (a) Results for component thermal inertia values of 2500 tiu for rocks and 77, 249, and 542 tiu for fines. Bolometric (dashed) and IRTM-20-μm-band spectral (solid) temperatures were used with the Putzig and Mellon (2006b) derivation algorithm. Dotted curves show results for IRTM-20-μm-band spectral temperatures from Golombek et al. (2003) which were derived using the algorithm of Mellon et al. (2000), assumed a constant (0.25) albedo for the mixture, and were limited to values below 800 tiu and 50% rock abundance. (b) Results for bolometric temperatures and component thermal inertia values of 1300 tiu (solid) and 2500 tiu (dashed) for rocks and 77, 114, 168, 249, 367, and 542 tiu for fines. Compare to Fig. 16 of Golombek et al. (2003). See text for discussion.

TES bolometric apparent thermal inertia (e.g. Mellon et al. 2000, Chapters 2 and 4), we provide the curves in Fig. 3.13b, which use the same fine and rock components as the complementary 20-μm spectral results of Golombek et al. (2003). As the preceding results in Section 3.3.1 illustrate, extreme caution should be taken when extrapolating the rock abundance relationship given here to other times of day, seasons, or latitudes.

3.4 Summary and conclusions

We have modeled the thermal behavior of horizontally heterogeneous surfaces on Mars, using simple two-component mixtures of idealized material components (dust, sand, duricrust, and rocks) and surface slopes. Material mixtures produce variations in apparent thermal inertia, with values gradually increasing diurnally between abrupt reductions at dawn and dusk and cycling seasonally with a period of one Mars year. There is generally a seasonal delay between daytime and nighttime extrema that varies with the thermal contrast of the mixture components. Larger variations occur with increasing proportions of the higher thermal inertia component. The amplitude of the seasonal variation in apparent thermal inertia also increases with latitude in either hemisphere.

For partially sloped surfaces, diurnal variations in apparent thermal inertia may show an increase, decrease, or both, depending on the slope angle and azimuth. Nighttime variations are generally about five times smaller than daytime variations. Seasonal variations also occur with a period of one Mars year, with the amplitude of variations much greater for surfaces with north- and south-facing slope components than for those with east- and west-facing slope components. An increase in slope angle results in an increase of the amplitude of seasonal apparent thermal inertia variations and also an increase in the magnitude of the difference between the annual-mean daytime and nighttime values. Similarly, increases in seasonal amplitude and annual-mean differences occur for increases in the percentage of sloped area. Increases in latitude in either hemisphere result in increases in the seasonal amplitude and the magnitude of the difference between daytime and nighttime annual-mean variations for surfaces with north- or south-facing components. Latitude has relatively little effect on the behavior of surfaces with only east- or west-facing slope components.

More complex surfaces, such as those with multiple slope azimuths or mixtures of materials and slopes, exhibit diurnal surface temperature and apparent thermal inertia characteristics which are much more variable. Simplified approximations based on linear mixing of the apparent thermal inertia of one- or two-component model results do not adequately characterize these surfaces.

These modeling results show that seasonal and diurnal variations in apparent thermal inertia can be as high as several 100 tiu, even for small ($\sim$ 10%) admixtures of materials with moderately contrasting thermal properties or slope angles. When considered together with similar results for layered surfaces (Mellon and Putzig 2006), it becomes evident that surface heterogeneity can be expected to be an important aspect of the thermal behavior of the martian surface, producing large variations in apparent thermal inertia as derived from spaceborne instruments. Proper interpretation of thermal inertia values taken from median or average maps or derived from single temperature observations must consider the potential effects of surface heterogeneity. While the thermal behavior of horizontally mixed surfaces is qualitatively similar in character for a broad range of materials, the apparent thermal inertia variations of different material mixtures are distinct in their details, particularly when seasonal and diurnal variations are considered together. This ability to discriminate between model types suggests the feasibility of using a suite of observations over a range of seasons and times of day to evaluate the surface heterogeneity of Mars.

The fact that different types of heterogeneity exhibit distinguishable characteristics provides a strong argument for obtaining surface temperature observations at as broad a range of time of day and season as possible in future missions. Given sufficient sampling, one might hope to overcome problems with non-unique solutions at particular times of day or seasons and incorporate horizontal material and slope mixtures directly into a thermal inertia derivation algorithm. However,

computational limitations may make such an effort impractical for some time to come. Until such a time as computing capabilities and seasonal and diurnal sampling allow a direct derivation of the properties of heterogeneous surfaces, one may employ heterogeneous-surface modeling together with single-point apparent thermal inertia derived from spacecraft data to provide some constraints on the degree and nature of surface heterogeneity. A first effort to characterize the surface heterogeneity of Mars using simple two-component models and TES results is presented in Chapter 4.

Chapter 4

Apparent thermal inertia and the surface heterogeneity of Mars

> The sun, with all those planets revolving around it and dependent on it, can still ripen a bunch of grapes as if it had nothing else in the universe to do.
>
> — Galileo Galilei

4.1 Introduction

Understanding the physical properties of the near-surface layer is critical to many elements of the Mars exploration effort. Apart from a few sites where spacecraft have landed, nearly all our information regarding the nature of the surface is the product of remote-sensing instruments. While visible images have been an important piece of the puzzle by providing the geological context of relatively large-scale features, certain aspects of the surface materials, such as composition, grain size, and the presence of volatiles in the subsurface, are not readily understood from visible image data alone. Spectral imaging and multi-spectral mapping provide some insight into these characteristics, and temperature derived from spectral radiance measurements is the basis for investigating many of the physical attributes of martian surface materials. Through numerical modeling, one may relate the surface temperature, which is greatly influenced by time-varying factors such as diurnal and seasonal variations of the local insolation and atmospheric constituents, to the physical properties of near-surface materials.

Such numerical models generally treat the thermal behavior of the martian

surface as an upper boundary condition on the heat equation, where upward radiative loss is balanced by heat flux due to insolation, downwelling atmospheric radiation, and seasonal CO_2 condensation, together with subsurface heat conduction:

$$\epsilon\,\sigma\,{T_{\rm S}}^4 = S_{\rm M}\,(1-A)\,\cos\,i + F_{\rm IR} + L\,\frac{\partial m}{\partial t} + I\,\sqrt{\frac{\pi}{P}}\,\frac{\partial T}{\partial Z'}\bigg|_{Z'=0}\,. \tag{4.1}$$

Here, ϵ is the emissivity of the surface or CO_2 frost if present, σ is the Stefan–Boltzmann constant, $T_{\rm S}$ is surface temperature, $S_{\rm M}$ is the insolation at Mars, A is albedo, i is the solar incidence angle, $F_{\rm IR}$ is downwelling atmospheric radiation, L is the latent heat of CO_2 sublimation with m the mass of CO_2 frost and t time, I is thermal inertia, P is the diurnal or seasonal period, T is subsurface temperature, and Z' is depth normalized to the thermal skin depth δ. The thermal skin depth is the e-folding depth of the subsurface diurnal or seasonal thermal wave given by

$$\delta \equiv \frac{I}{\rho\,c}\,\sqrt{\frac{P}{\pi}}\,, \tag{4.2}$$

where the density ρ and heat capacity c are bulk material properties of the near-surface layer. Thermal inertia is defined as a combination of bulk thermal conductivity k, density, and heat capacity such that

$$I \equiv \sqrt{k\,\rho\,c}\,. \tag{4.3}$$

One may infer from the subsurface conduction term (the last term in Eq. 4.1) that thermal inertia is the key material property controlling the diurnal and seasonal surface temperature variations. For granular materials under Mars surface conditions, conductivity tends to dominate the thermal inertia (Wechsler et al. 1972, Jakosky 1986) and is controlled primarily by physical characteristics, such as particle size and porosity, within a thermal skin depth of the subsurface. In general, surfaces of unconsolidated, fine-grained materials will have low values of thermal inertia, cemented surfaces and surfaces composed of sand-sized grains will

have intermediate values, and rocky surfaces and bedrock outcrops will have high values.

If surface materials are level and either homogeneous or mixed only on horizontal and vertical scales much smaller than a diurnal thermal skin depth, they will exhibit uniformly changing temperature and a constant value of thermal inertia (Jakosky 1986). If they contain divergent slopes or are mixed at larger scales, different surface components may have different temperatures at any given time. The surface temperature as observed from an orbiting spacecraft will be a composite mixture of the component temperatures on the scale of the observing-instrument resolution ($\sim$3 km for the Mars Global Surveyor Thermal Emission Spectrometer, MGS-TES) and on depth scales on the order of a seasonal thermal skin depth (a few decimeters to a few meters, depending on the properties of the surface materials). Where horizontal mixtures or near-surface layers of differing materials are present in the instrument's field of view, the apparent thermal inertia derived from surface temperature observations will vary with time of day and season (or season only, if the surface layer is homogeneous and thicker than a diurnal skin depth but thinner than a seasonal skin depth), due to the nonlinear relationship between temperature and thermal inertia (see Eq. 4.1) and any differential heat storage in the subsurface. Similar effects will occur for surfaces where portions of the field of view have non-zero slopes (see Chapter 3).

Since the earliest radiometric observations of Mars (Sinton and Strong 1960), diurnal temperature has exhibited anomolous behavior which appears to be incompatible with homogeneous models of surface materials. Some consideration was given to surface heterogeneity as a possible cause, calling on analogous studies of lunar temperature observations (Jaeger and Harper 1950) which invoked a layered regolith. Differences between surface albedo as determined from visible-band observations and as derived from temperature data in tandem with thermal

inertia (Kieffer et al. 1977, Palluconi and Kieffer 1981) are also suggestive of surface heterogeneity, but have never been fully explained (Hayashi et al. 1995). The presence of an atmosphere at Mars complicates the thermal behavior. While early thermal models neglected most atmospheric effects (e.g., Morrison et al. 1969, Kieffer et al. 1973, 1977), subsequent efforts to compensate for airborne dust and other atmospheric phenomena (Jakosky 1979, Palluconi and Kieffer 1981, Ditteon 1982) reduced but did not eliminate the anomalies. Modeling of heterogeneous surfaces (Jakosky 1979, Ditteon 1982) provided qualitative explanations, but no detailed assessment of the relationship to the diurnal, seasonal, and geographic variations observed on Mars was pursued. Christensen (1982) developed a technique to estimate rock abundance at the surface by comparing different spectral bands in individual observations. He found that rocks alone were insufficient to explain observed geographic variations in thermal inertia (Christensen 1986b), and other types of heterogeneity, such as regional variations in the degree of induration (Jakosky and Christensen 1986), remained the most-likely explanation for the temperature anomalies.

Studies of ground-ice stability in the polar regions as well as at lower latitudes (Paige 1992, Mellon and Jakosky 1993, 1995, Vasavada et al. 2000, Mellon et al. 2004) and the recent detection of near-surface hydrogen attributed to the presence of ground ice (Boynton et al. 2002, Feldman et al. 2004) have implications for surface heterogeneity. To the extent that ground ice forms within a seasonal skin depth of the surface, seasonal variation in apparent thermal inertia is expected. Previous global mapping of thermal inertia (Chapter 2) showed high nighttime values in the north polar region. While it was suggested that these results may have been due to either atmospheric effects or modeling artifacts associated with the polar dawn, modeling of the thermal behavior of ground ice in this region by Chamberlain and Boynton (2005) demonstrated that similar effects

may occur if near-surface ground ice is present. In an effort to estimate depth to ground ice for Phoenix Lander site characterization, Titus et al. (2006) fit TES brightness temperature observations to two-layer thermal-model results, yielding estimates of ground-ice depth well within a seasonal skin depth in all three of their study regions.

Current modeling of the effects that horizontal mixtures of materials and partially sloped surfaces have on apparent thermal inertia was presented in Chapter 3. In that effort, we used the numerical thermal model presented here to obtain temperatures for idealized surfaces of constant properties and then found effective temperatures for multi-component surfaces by performing a linear mix of the Stefan–Boltzmann function (left-hand side of Eq. 4.1). Modeled values of apparent thermal inertia were determined from the effective temperatures using the same derivation algorithm as is used here for obtaining apparent thermal inertia from TES observations. To investigate the effects of layering, Mellon and Putzig (2006) employed a modified numerical model of a layered subsurface (see Mellon et al. 2004). They used this layered thermal model to compute effective temperatures for idealized layered surfaces and derived apparent thermal inertia to examine its variations. In this work, we use these heterogeneity-modeling techniques to compare the effects of simple two-component, horizontally-mixed and layered surfaces to the apparent thermal inertia derived from TES data, with the goal of globally mapping the different types of heterogeneity that may explain the variations observed in the data.

In the following section, we describe our modifications of the thermal model and algorithm developed by Mellon et al. (2000) and the derivation of thermal inertia from TES data, discuss our methods of mapping seasonal apparent thermal inertia, summarize the heterogeneity-modeling methods employed herein, and explain our technique for mapping the surface heterogeneity of Mars. In Section 4.3,

we present our TES mapping results, local comparisons between TES and model results for landed-spacecraft sites and other regions of interest, and global maps of heterogeneity. We conclude with a summary of our results and a discussion of their implications for the greater Mars exploration effort.

4.2 Methodology

Prior to the MGS-TES mission, the thermal inertia of the martian surface was generally derived by fitting multiple, co-located spacecraft observations of brightness temperature from various times of day to modeled temperature curves. The technique treated both albedo and thermal inertia as free parameters in matching the observed diurnal temperature oscillations (e.g., Kieffer et al. 1973, 1977, Palluconi and Kieffer 1981, Hayashi et al. 1995). Because the TES instrument observes the surface from a fixed-local-time orbit, there are generally only two times of day available (02:00 and 14:00), and overlapping groundtracks are relatively rare. Thus, the multi-point curve-fitting technique is not appropriate for the TES dataset.

4.2.1 Thermal inertia derivation

For deriving thermal inertia from TES brightness temperature observations, Mellon et al. (2000) developed a single-point method which was employed to produce global maps of nighttime thermal inertia by Jakosky et al. (2000), Mellon et al. (2000), and in Chapter 2 with increasingly higher spatial resolution and coverage. In this method, a numerical thermal model is used to generate a lookup table of temperatures for intervals of season, time of day, latitude, surface pressure, dust opacity, albedo, and thermal inertia (Jakosky 1979, Haberle and Jakosky 1991, Mellon et al. 2000). Each observed brightness temperature is correlated with other data and interpolated through the lookup table to find the

best-fitting thermal inertia. Because measurements of geographic and temporal opacity variations were not then available, the interpolation algorithm assumed a constant infrared dust opacity of 0.1 at 6.1 mbar, scaled to the local elevation. This was found to be consistent with average TES spectral observations during much of the mapping mission (Mellon et al. 2000, Smith et al. 2001b, Smith 2004, and Chapter 2), but did not account for any local or seasonal opacity variations. Water-ice-cloud opacity was not expected to be available and is not taken into account by the thermal model. Instead, individual observations from locations and times of high dust- or water-ice-cloud opacity were removed prior to mapping (Mellon et al. 2000, Chapter 2).

Derivation of thermal inertia by Mellon et al. (2000) and in Chapter 2 produced values at the limits of the lookup-table bounds (24 and 800 tiu) and their mapping results contained large gaps at the highest elevations. For this work, we modified the thermal model and derivation algorithm of Mellon et al. (2000) to accommodate a wider range of thermal inertia and atmospheric pressure, and we added a more realistic transition of properties for times when CO_2 frost is accumulating. For emissivity and albedo, we use a cosine-weighted transition from bare-ground values when no CO_2 frost is present to CO_2-ice values when the CO_2-frost mass reaches 6 kg/m^2. This functional dependence agrees well with albedo and emissivity models for CO_2 frost (Warren et al. 1990). We generated a new lookup table, expanding the range of thermal inertia to 5–5000[1] tiu and the range of pressure to 0.8–15.0 mbar. We also decreased the node spacing for infrared dust opacity from 0.5 to 0.4 to reduce interpolation errors, and we modified the interpolation algorithm to incorporate measured dust opacity, account for inter-annual albedo variations, and employ $\frac{1}{20}$ °-resolution Mars Orbiter Laser Altimeter (MOLA) maps of elevation (used for surface pressure determinations)

[1] See also Fig. A.1 in the Appendix.

Table 4.1. Lookup-table and algorithm enhancements

Dimension	Lookup-table range [nodes]		Data source and map resolution	
	Mellon et al. (2000)	This work	Mellon et al. (2000)	This work
Mars day	0–668 [84]	Same	TES ephemeris	Same
Mars hour	1–24 [24]	Same	TES ephemeris	Adjusted by $\frac{1}{20}^\circ$ slope map
Latitude (°N)	-90–90 [37]	Same	TES ephemeris	Adjusted by $\frac{1}{20}^\circ$ slope map
Dust opacity	0.0–1.0 [3]	0.0–0.8 [3]	Assumed constant at 0.1	2-day 5° maps of TES data*
Pressure (mb)	3.0–10.0 [3]	0.8–15.0 [5]	Scaled 1° elevation map	Scaled $\frac{1}{20}^\circ$ elevation map
Albedo	0.15–0.35 [3]	Same	$\frac{1}{4}^\circ$ TES map	3 annual $\frac{1}{20}^\circ$ TES maps
Thermal inertia (tiu)	24–800 [10]	5–5000 [21]	$\frac{1}{4}^\circ$ nighttime map	$\frac{1}{20}^\circ$ nightside & dayside maps

*Dust opacity data from Smith et al. (2001b), Smith (2004).

and planetary radii (used for an approximate regional slope correction). Each of these elements is discussed in detail below and a summary of lookup-table and algorithm enhancements is presented in Table 4.1.

The MGS spacecraft completes 12 orbits each Mars day, with orbit tracks spaced at approximately 30 ° in longitude. Atmospheric dust and water-ice-cloud opacity (Smith et al. 2001b, Smith 2004) were derived from daytime observations and can vary significantly over the course of a few days. Figure 4.1 shows the seasonal variation of the globally averaged TES dust opacity for all orbits included in our processing, spanning two complete Mars years and portions of two others (Mars Years 24–27). Globally, the dust opacity shows a regular cycle, with dust-storm activity commencing near $L_S = 135$, intensifying after the equinox at $L_S = 180$, and continuing through the southern spring and early summer to about $L_S = 310$. Apart from a late-summer storm during Mars Year 26, a trend of declining opacity generally follows as dust settles out of the atmosphere. Dust opacity affects surface temperatures in much the same way as thermal inertia (Mellon et al. 2000),[2] and an analysis aimed at understanding seasonal variations in thermal inertia must consider seasonal dust-opacity variations as well. To optimize spatial and temporal coverage, we mapped dust and water-ice-cloud opacity for two Mars days (24 orbits, including the current and previous days) at 5 ° resolution in longitude and latitude, when processing observations for each day. We interpolated each map for use in the derivation and mapping of thermal inertia for both nighttime and daytime observations. Dust opacity for the two days leading up to the observation has the greatest influence on surface temperatures.

The surface albedo of Mars has been observed to change significantly from year to year, which is attributable to the redistribution of dust that occurs predominantly during global dust storms (Pleskot and Miner 1981, Christensen 1988).

[2] See also Fig. A.2 in the Appendix.

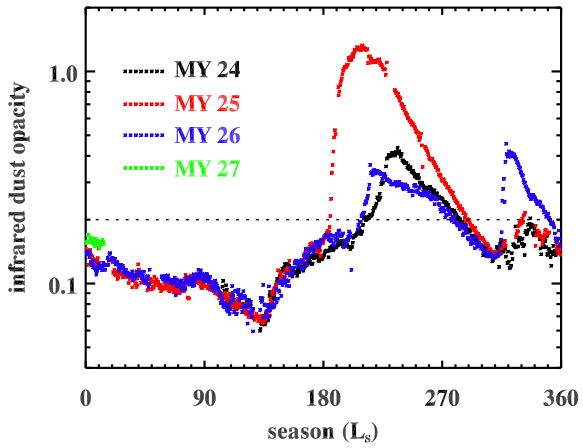

Figure 4.1 TES atmospheric infrared dust opacity, globally averaged each Mars day for orbits 1,583–24,346, color-coded by Mars Year. Dotted line at 0.2 opacity shows local threshold value used to select thermal inertia for mapping. Trends are remarkably consistent from year to year outside of the peak dust-storm seasons ($\sim L_S$ 180–310).

Since we were intending to process observations spanning three Mars years during which global storms had been observed (Geissler 2005), we created separate annual maps of TES visible-bolometer albedo (Christensen et al. 2001) for each Mars year at $\frac{1}{20}^\circ$ resolution, filtering out seasons and locations with high dust and water-ice-cloud opacity. Maps of TES albedo for the latest year included, Mars Year 26, and the change since the first year included, Mars Year 24, are presented in Fig. 4.2. Albedo changes of $\sim$0.05 are common in many broad regions, with more-isolated areas having brightened or darkened by 0.10 or greater. An accurate measure of albedo is important to the derivation of thermal inertia, particularly in the daytime when albedo has larger effects on surface temperature (Mellon et al. 2000).[3]

Surface slopes also can have large effects on diurnal and seasonal surface temperature variations (Spencer 1990, Colwell and Jakosky 2002, Chapter 3). In this context, slope refers to deviations of the surface from a sphere and not from

[3] See also Fig. A.2 in the Appendix.

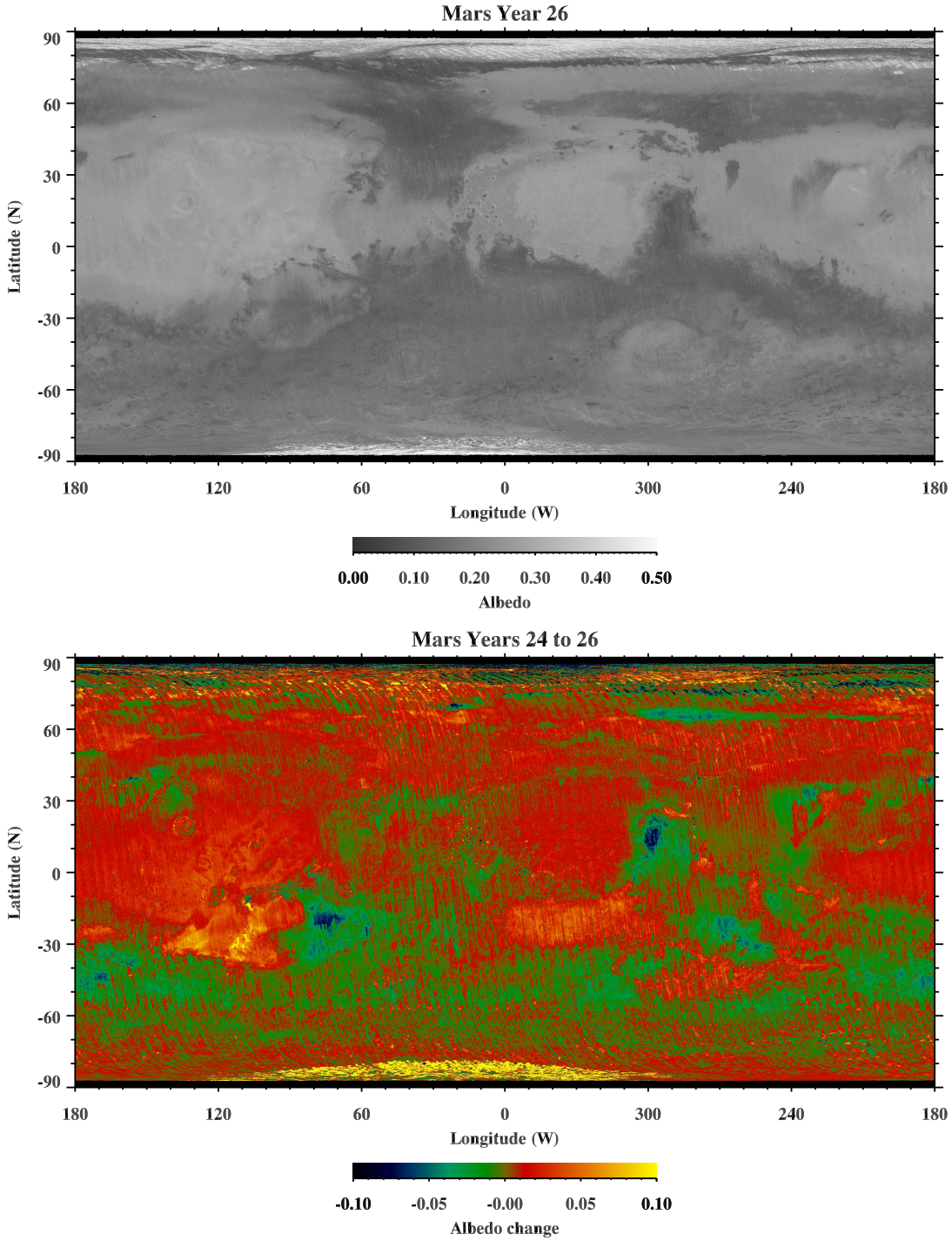

Figure 4.2 TES global albedo for Mars Year 26 (top) and the change of albedo between Mars Years 24 and 26 (bottom). Albedo maps were binned at $\frac{1}{20}^\circ$ per pixel and infilled between 87 °S and 87 °N latitude. Large interannual changes occur after major dust storms.

a gravitational potential surface, since the thermal effects are driven by the solar incidence angle. Prior work has not accounted for slope in the derivation of thermal inertia since the incorporation of full slope corrections is computationally impractical for a global study and regional slopes are generally limited to a few degrees (e.g., 99.4% of the surface has an average slope of less than 10° at TES $\frac{1}{20}$° resolution). However, slope based on planetary radii includes polar flattening due to Mars' spin, which when combined with the N–S hemispheric topographic dichotomy (Smith et al. 2001a), results in poleward median slopes of 0.15° and 0.23° in the southern and northern hemispheres, respectively, as determined from MOLA radii binned at TES resolution.[4] Small hemispherical and other regional slopes will introduce a slight bias in apparent thermal inertia if they are not taken into account. We therefore incorporated an approximate correction for slope, wherein the true time of day and latitude of each observation are adjusted to effective time of day and latitude based on the average slope over each observational footprint. Our approximate correction includes the effect of changes in insolation due to slope at ∼3-km resolution, but not the effect of differences in atmospheric path length.

To quantify the atmospheric-path-length effect and determine maximum slope values for applying our approximate corrections, we modified the thermal model to include full corrections for slope angle and azimuth. For 02:00 and 14:00 local times, the approximate corrections begin to deviate from full corrections within a few degrees of slope, but they improve the accuracy of derived thermal inertia up to high angles in three of the four cardinal directions (50° or more for N–S slopes and 20° or more for eastward slopes). The approximate correction deteriorates for westward slopes greater than 10° due to the delay of heating toward late afternoon which causes a pronounced skew in the diurnal temperature

[4] See also Fig. A.4 in the Appendix.

curve (see Fig. 3.6). Consequently, we do not apply the effective-time-of-day adjustment for observations where the westward component of slope exceeds 10 °. Slopes greater than about 15 ° in any direction will produce highly inaccurate results with or without the approximate corrections, so we chose to apply the corrections for all slope components in the other cardinal directions. Over 99.95% of map pixels have average slopes less than 20 °, so our approximate corrections improve the accuracy of apparent thermal inertia nearly everywhere.

The slope corrections discussed here refer to the average slope within each map pixel. Sub-pixel slope effects on apparent thermal inertia are a separate concern and were investigated in Chapter 3 using the modifications to the thermal model discussed above. We present a comparison of modeled apparent thermal inertia for partially sloped surface models with TES results in Section 4.3.2.

4.2.2 Thermal inertia mapping

Using our modified interpolation algorithm, we processed three Mars years of brightness temperature observations from TES orbits 1,583–24,346 to derive apparent thermal inertia. Any inaccuracy in the mapped dust opacity discussed above may lead to inaccurate thermal inertia. Also, each result may be affected by physics that is not included in the thermal model, such as the effects of water-ice clouds. Therefore, thermal inertia values were excluded for observations with infrared dust opacity greater than 0.2 or infrared water-ice-cloud opacity greater than 0.1 as mapped for the two days prior to the temperature observations, and for brightness temperatures below 160 K (to avoid CO_2 frost). We also explicitly rejected TES orbits 2,135-2,146 which correspond to the particularly severe global dust storm during Mars Year 26 (2001). The remaining results were used to produce 36 nightside and 36 dayside seasonal maps, each encompassing 10 ° of L_S at $\frac{1}{20}$ ° per pixel resolution ($\sim 3 \times 3$ km at the equator), which is approximately

equivalent to the intrinsic resolution of the TES instrument.

Throughout this work, the terms 'nightside' and 'dayside' refer respectively to the southbound and northbound legs of the MGS orbit. Local times for these orbit legs are nominally 02:00 and 14:00, but they vary rapidly between these times as the spacecraft crosses the polar regions near 87° latitude. Consequently, the polar regions of some nightside maps contain observations from periods when the Sun was continuously above the horizon. Previous global mapping of TES thermal inertia (Mellon et al. 2000, Chapter 2) employed only nighttime data—with selection criteria that restricted coverage to polar night—and was therefore limited to late summer when CO_2 frost was absent in these regions. Due to the seasonal variability which will be discussed below, the resulting thermal inertia was not representative of the average surface properties, especially in the north.

As with previous TES mapping efforts (Mellon et al. 2000, Chapter 2), we compensated for the shrinking of the map-pixel scale with latitude due to converging lines of longitude by binning each value of thermal inertia into all the longitudinal bins covered by its nominal observational footprint at each latitude. The TES instrument's downtrack smear of 5.4 km (see Section 2.2) and longitudinal variations within each observation ensure that any given observation does not fall entirely within a single map pixel, even at low latitudes. Additionally, overlapping observations of any particular location are only partially coincident with each other and the values of thermal inertia calculated from them are not linearly related to the fluxes measured. For practical reasons, we performed only a simple linear averaging of thermal inertia within each bin and thus the values within any given pixel throughout each map are actually representative of a somewhat larger area.

To provide a complete global representation of nightside and dayside thermal inertia, as well as a basis for comparison to previous global nighttime mapping

Table 4.2. Model surface materials

Type Material	Inertia†	Albedo	Density†	Heat Cap.†	Skin Depth (m) Diurnal (δ_D)	Seasonal (δ_S)
Dust	56	0.26	1375	837	0.008	0.212
Sand*	223	0.16	1650	837	0.027	0.702
Duricrust	889	0.23	1875	854	0.093	2.413
Rock	2506	0.16	2500	837	0.201	5.206

†Thermal inertia in tiu, density in $\mathrm{kg\,m^{-3}}$, heat capacity in $\mathrm{J\,kg^{-1}\,K^{-1}}$.

*Material used for slope mixtures.

results of Mellon et al. (2000) and Fig. 2.1, we latitudinally cropped each of the 36 seasonal maps and produced nightside and dayside median maps. The median operator should be more representative of the surface properties than the mean, due to the fact that seasonal variations in apparent thermal inertia can be quite large and nonlinear (see Section 4.3.1).

4.2.3 Heterogeneity modeling

In order to understand the diurnal and seasonal variations in apparent thermal inertia observed in TES results (see Section 4.3.1), we employed the numerical techniques of Chapter 3 and Mellon and Putzig (2006) to produce a suite of two-component diurnal and seasonal temperature curves for idealized surface materials (dust, sand, duricrust, and rock), where each component has fixed values of thermal inertia, albedo, density, and heat capacity (see Table 4.2). Values of thermal inertia for each material were selected on lookup-table nodes to minimize interpolation errors and values of albedo were chosen at TES global modes (see 2.4). Representative values for basaltic materials were adopted for density and heat capacity, modified in the case of duricrust to approximate the effects of sulfate

cements in pore spaces. For horizontal mixtures of materials, the thermal model described in Section 4.2.1 was used to generate surface temperatures T_{S_i} for each component. For partially sloped surfaces, we generated component temperatures for a limited set of slopes (1, 5, 10, 45, and 90 °) and azimuths (0, 45, 90, 180 and 270 °) and a single material (sand). Effective temperatures T_{S_e} for horizontal mixtures of materials or slopes were determined by performing a linear mix of the Stefan-Boltzmann function, assuming unit emissivity:

$$\sigma T_{S_e}^4 = \sigma \sum_i A_i T_{S_i}^4 , \tag{4.4}$$

where A_i is the fractional area of the ith model component (Chapter 3). For layered materials, we used a layered version of the thermal model (Mellon et al. 2004, Mellon and Putzig 2006) to generate effective temperatures for various two-layer configurations of the same idealized components. The layered model allows a single upper layer over a substrate, where each layer may have distinct, fixed material properties. The thickness of the upper layer may be set to values greater than about $\delta_S/512$, where δ_S is the seasonal skin depth. For thicknesses greater than about a seasonal skin depth, the upper layer becomes thermally "opaque" and the model results are indistinguishable from the constant-properties case.

For each class of heterogeneity (mixed and layered), apparent thermal inertia is derived from the modeled temperatures using the same algorithm employed for TES data derivations (see Section 4.2.1). To avoid introducing numerical uncertainty in the apparent thermal inertia of layered surfaces, a separate lookup table was generated from the layered thermal model assuming only one layer Mellon and Putzig (2006). Thermal inertia was derived for local times 02:00 and 14:00 every 10 ° of L_S at 10 ° intervals of latitude, assuming constant values of zero for elevation and dust opacity. Models were run with component horizontal-mixing ratios of 0:100, 10:90, 30:70, and 50:50 and upper-layer thicknesses of

Table 4.3. Modeling parameters

Parameter	Values [count]
Mix percentage	0, 10, 30, 50, 70, 90, 100
Layer thickness†	$\delta_S/512$–$2\delta_S$ by $\times 2$ [11]
Time of day	02:00 and 14:00
Season (Mars day)	0–668, every 8 [84]
Latitude (°N)	-90–90, every 10 ° [19]
Slope angle (°)	0*, 1, 5, 10, 45, 90
Slope azimuth (°)	0*, 45, 90, 180, 270

†See Table 4.2 for δ_S values.

*Fixed slope value for material mixtures.

$\delta_S/512$ to $2\delta_S$ spaced at powers of 2. See Table 4.3 for a summary of modeling parameters.

Comparisons of TES data and model results for selected locations, including past and present landing sites, are presented in Section 4.3.2. Modeled seasonal variations in apparent thermal inertia for different material mixtures or layers can be qualitatively similar for any given local time (Chapter 3, Mellon and Putzig 2006). Thus, our initial efforts to compare TES data and model variations separately for nightside and dayside observations yielded matches to different model types for many locations at these two times of day. When modeling results for different local times (e.g., 02:00 and 14:00) are considered together, the behavior of the different model types are more readily distinguishable. We therefore developed a simultaneous (nightside and dayside) curve-matching technique for the purpose of finding the best-fit between TES-data and model results for apparent thermal inertia. For a given location and model type (e.g., mixed dust and rock, layered duricrust over dust, etc.), we first extract nightside and dayside TES data from the seasonal maps, calculating the median value in the specified region for

each season. Next, we linearly interpolate the modeled seasonal curves of apparent thermal inertia between modeled latitudes to the specified latitude. We then find the sum of the annual median of dayside and nightside results for the TES data and for the set of bounding modeled seasonal curves. Using the ratio of the differences between the data and model summed medians, we linearly interpolate the bounding modeled seasonal curves to find an estimated closest-fitting set of curves for the current model type. A null-match results where the sum of data medians does not fall between the sum of medians for any set of model curves. Where we do find a match, we then calculate the RMS of differences between the TES data and the interpolated model curves for dayside and nightside and sum them together. Within each class of models (mixed and layered), we select the model type with the minimum sum of RMS differences between data and model as the best-fit for that class. Given the actual nonlinear nature of the base model results, any intermediate estimates of mixing ratio or layer thickness derived from this fitting technique may contain substantial errors and should be interpreted accordingly.

To facilitate the production of global heterogeneity maps, we automated the matching of TES data to modeled seasonal curves as described above by applying a selection threshold (chosen empirically at 40 tiu) to the RMS of the differences between the data and estimated best-fit model curves. Matches are further restricted to those having an RMS of differences that is less than 5% of the difference in thermal inertia of the model-component materials. The latter restriction eliminates spurious matches between highly variable TES results and relatively invariable low-thermal-contrast model results (predominantly those with dust and sand components). Matches with nightside or dayside RMS values exceeding these thresholds are not considered for heterogeneity mapping. We applied our matching algorithm at a resolution of 5° per pixel to capture variations in regional

surface characteristics without introducing higher-order seasonal variations seen in higher-resolution TES results which tend to derail the matching algorithm.

4.2.4 Uncertainty

Mellon et al. (2000) estimated a total uncertainty of 6% for nighttime bolometric thermal inertia, and this value remain essentially unchanged for our modified algorithm. Small reductions in the interpolation uncertainty for thermal inertia, atmospheric pressure, and dust opacity due to finer node spacing do not significantly alter the computational uncertainty. As discussed by Mellon et al. (2000), other, less-tractable sources of uncertainty are of greater concern. Some reduction of uncertainty was achieved by including two-day dust opacity maps and higher-resolution maps of elevation and annual albedo. Our inclusion of an approximate regional-slope correction reduces uncertainty due to regional slopes $< \sim 15\,^{\circ}$ and corrects an error in the solar incidence angle which was introduced by the use of areocentric latitudes (i.e., polar flattening). Other uncertainty sources that are difficult to quantify include uncorrected atmospheric effects (e.g., water-ice clouds, horizontal transport), non-lambertian albedo (Pleskot and Miner 1981, Section 2.3.2.1), and sub-pixel surface frosts. Since both the calculation of TES bolometric brightness temperatures and the thermal model assume unit emissivity, spatial variability in emissivity should not be a significant source of error in the derived thermal inertia (Mellon et al. 2000).

Earlier restriction to nighttime-only data for mapping TES thermal inertia (Jakosky et al. 2000, Mellon et al. 2000, Chapter 2) was predicated on concerns about greater daytime sensitivity to inaccuracies in albedo, which has been shown to vary significantly between global dust storms (e.g., Pleskot and Miner 1981, Christensen 1988; see also Fig. 4.2). By using separate annual maps of higher-resolution albedo, we have sufficiently reduced this source of uncertainty to provide

greater confidence in daytime results and allow the first global dayside mapping of apparent thermal inertia.

The heterogeneous-surface modeling results are subject to the same numerical uncertainty as are those derived from TES observations. As discussed above, linear interpolation of the modeled thermal inertia in latitude and in mixing percentage or layer thickness was performed to produce best-fit curves and their associated RMS differences with respect to the TES data. Departures from linearity may result in substantial errors in these interpolated results and RMS values, which we estimate may be as high as 10% for horizontal-mixture models and 20% or more for layered models. The latter models exhibit increasingly nonlinear behavior for extremely thin upper layers with higher thermal inertia and also for layer thicknesses greater than a diurnal skin depth ($\delta_D \approx \delta_S/26$) for upper layers with lower thermal inertia.

4.3 Results and analysis

In this section, we present our results for global seasonal mapping of TES-derived apparent thermal inertia, comparisons between results from TES data and idealized two-component surface modeling at selected locations, and global heterogeneity maps showing the best-fitting results for two-component horizontally-mixed and layered materials.

4.3.1 TES apparent thermal inertia maps

The 36 seasonal maps of apparent thermal inertia derived from TES brightness temperatures as described in the previous section showed latitudinally dependent bands of high thermal inertia immediately equatorward of zones where data was rejected due to low temperature (< 160 K) that is a likely indicator of complete CO_2-frost coverage at the surface. We attributed these zones of high thermal iner-

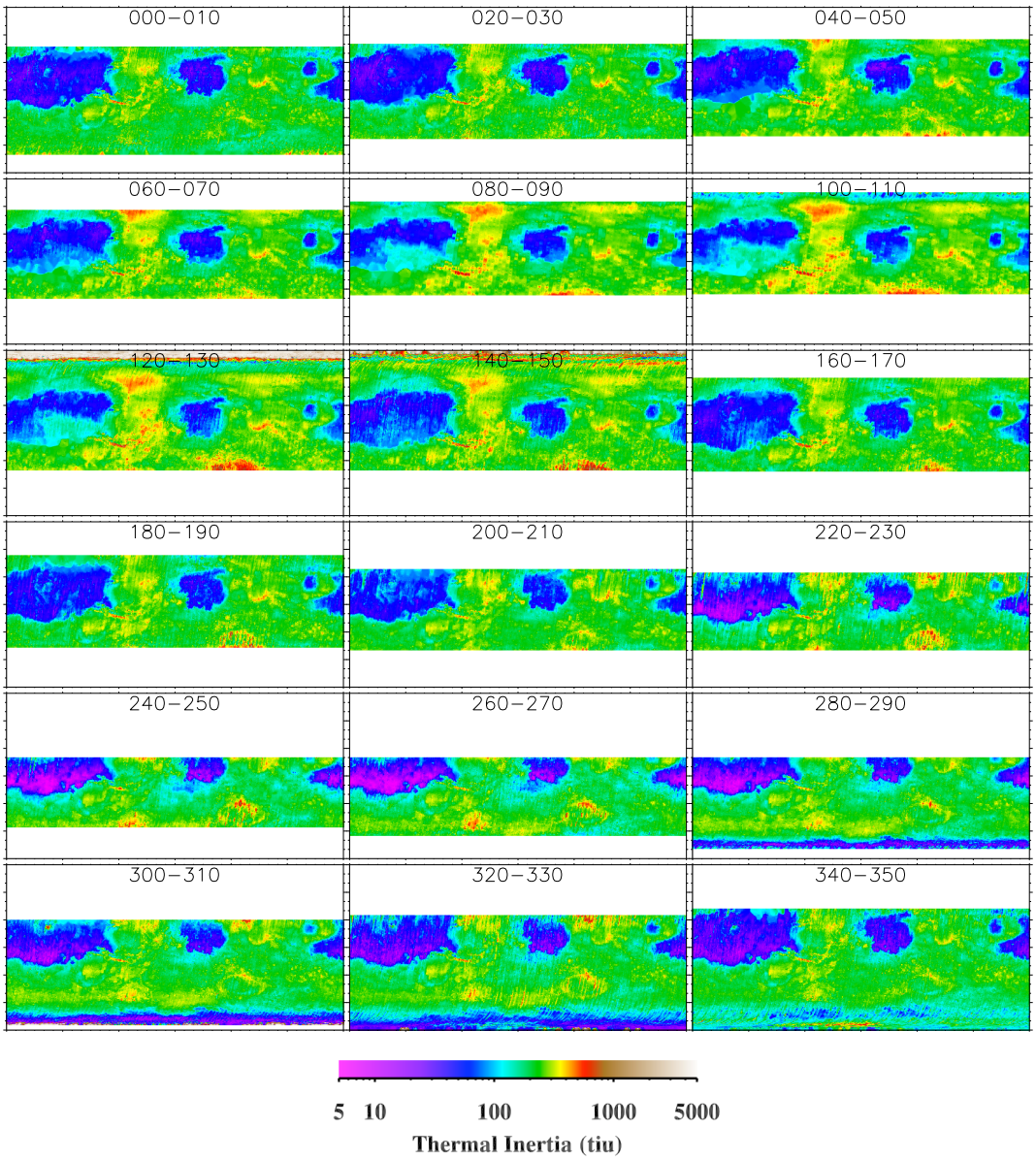

Figure 4.3 TES global nightside bolometric apparent thermal inertia for 10 °-L_S seasons every 20 ° of L_S. Maps include 3 Mars years of observations and were rebinned from $\frac{1}{20}$ ° to $\frac{1}{2}$ ° per pixel and filled between cropped latitudes. Maps show systematic seasonal variations (see text).

tia to partial CO_2-frost coverage in the affected regions, and cropped these maps at fixed latitudes to remove the frosted regions. Figures 4.3 and 4.4 show a sampling of seasons throughout the year. Each seasonal map contains data from three

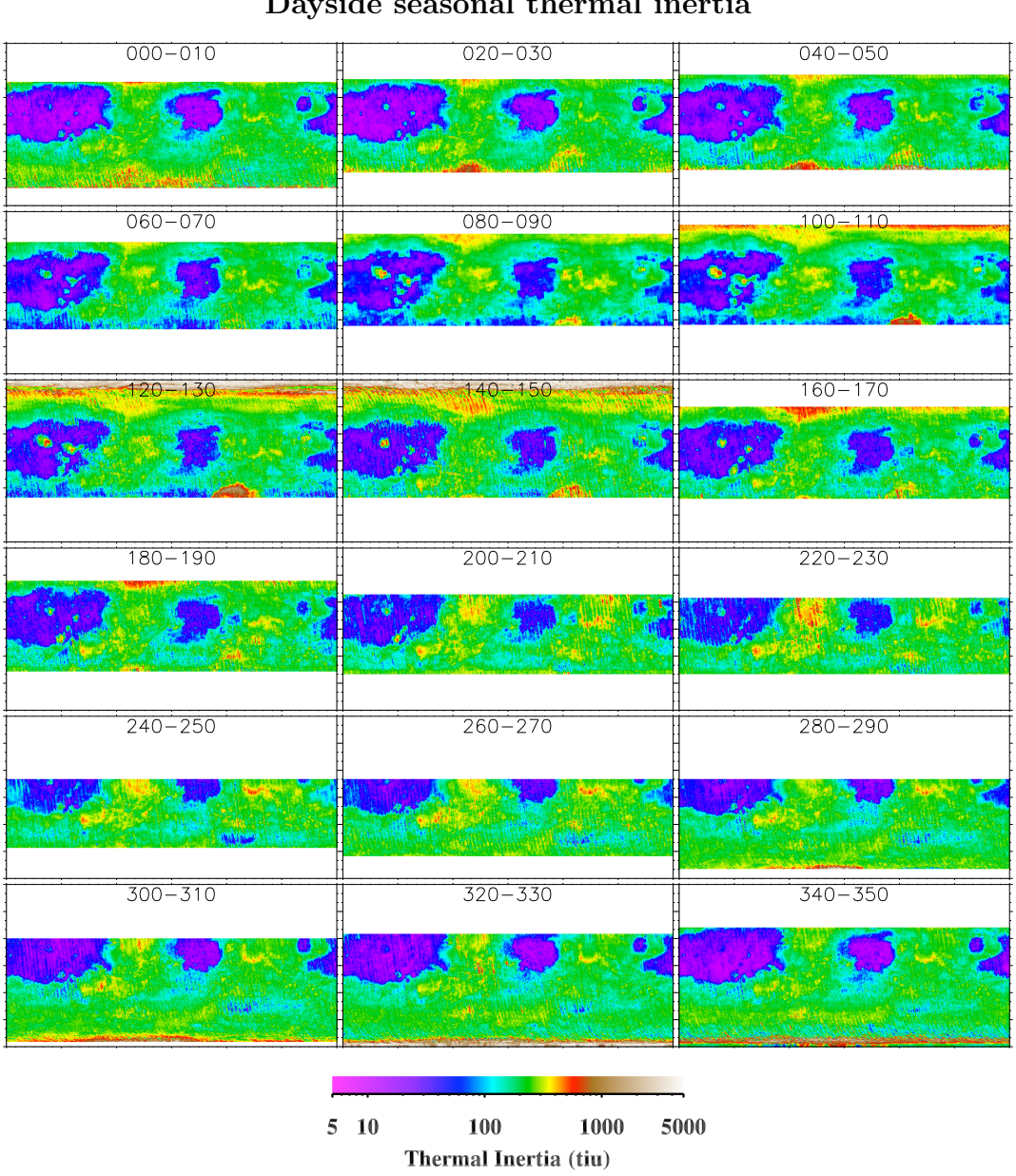

Figure 4.4 TES global dayside bolometric apparent thermal inertia for 10 °-L_S seasons every 20 ° of L_S. Maps include three Mars years of observations and were rebinned from $\frac{1}{20}$ ° to $\frac{1}{2}$ ° per pixel and filled between cropped latitudes. Like nightside, maps show systematic seasonal variations, but extrema occur at different seasons (see text).

Mars years and shows a high degree of regional consistency, which reflects a lack of large inter-annual variations in apparent thermal inertia. A systematic variation of regional apparent thermal inertia over the course of the martian year is evident

in the maps. At mid-latitudes (60 °S to 60 °N), the seasonal maps show a general sinusoidal trend of thermal inertia in time, with a nightside maximum near $L_S = 110$ and minimum near $L_S = 260$, and a dayside maximum near $L_S = 220$ and minimum near $L_S = 0$. The polar regions are more limited in seasonal coverage and show a greater magnitude of change between each map for the available seasons, with nightside apparent thermal inertia generally increasing and dayside generally decreasing with season, converging toward similar values.

Maps of the amplitude of the seasonal variations in apparent thermal inertia for nightside and dayside observations are presented in Fig. 4.5. Nearly all locations show amplitudes of variation greater than 50 tiu, with dayside amplitudes higher than nightside by $\sim$50 tiu on average. Areas of high thermal inertia generally show greater amplitudes of variation than areas of low thermal inertia (compare Fig. 4.6), but the geographic pattern of amplitudes differs between nightside and dayside. The largest amplitudes occur over the permanent polar ice caps, more broadly in the polar regions on the dayside, over the Tharsis and Olympus Mons volcanoes on the dayside, and in Hellas (290 °W, 40 °S) and Argyre (45 °W, 50 °S) basins. These latter occurrences are the result of very high apparent thermal inertia near the edge of the cropped regions from isolated seasons during the southern fall and winter ($L_S = 0$–180; see Figs. 4.3 and 4.4), and may be associated with partial CO_2 frost coverage. Apart from a band near 80 °N on the nightside where only one or two seasons were available, the lowest amplitudes of variation occur on the nightside for a region surrounding Alba Patera (110 °W, 40 °N) and extending eastward to about 55 °W. Nightside low amplitudes also occur on the flanks of the Tharsis and Olympus Mons volcanoes to the south. On the dayside, these same locations show moderate to very large (several 100 tiu) variations. Homogeneous surfaces should not exhibit large amplitudes of seasonal variation in apparent thermal inertia—such behavior is indicative of surface het-

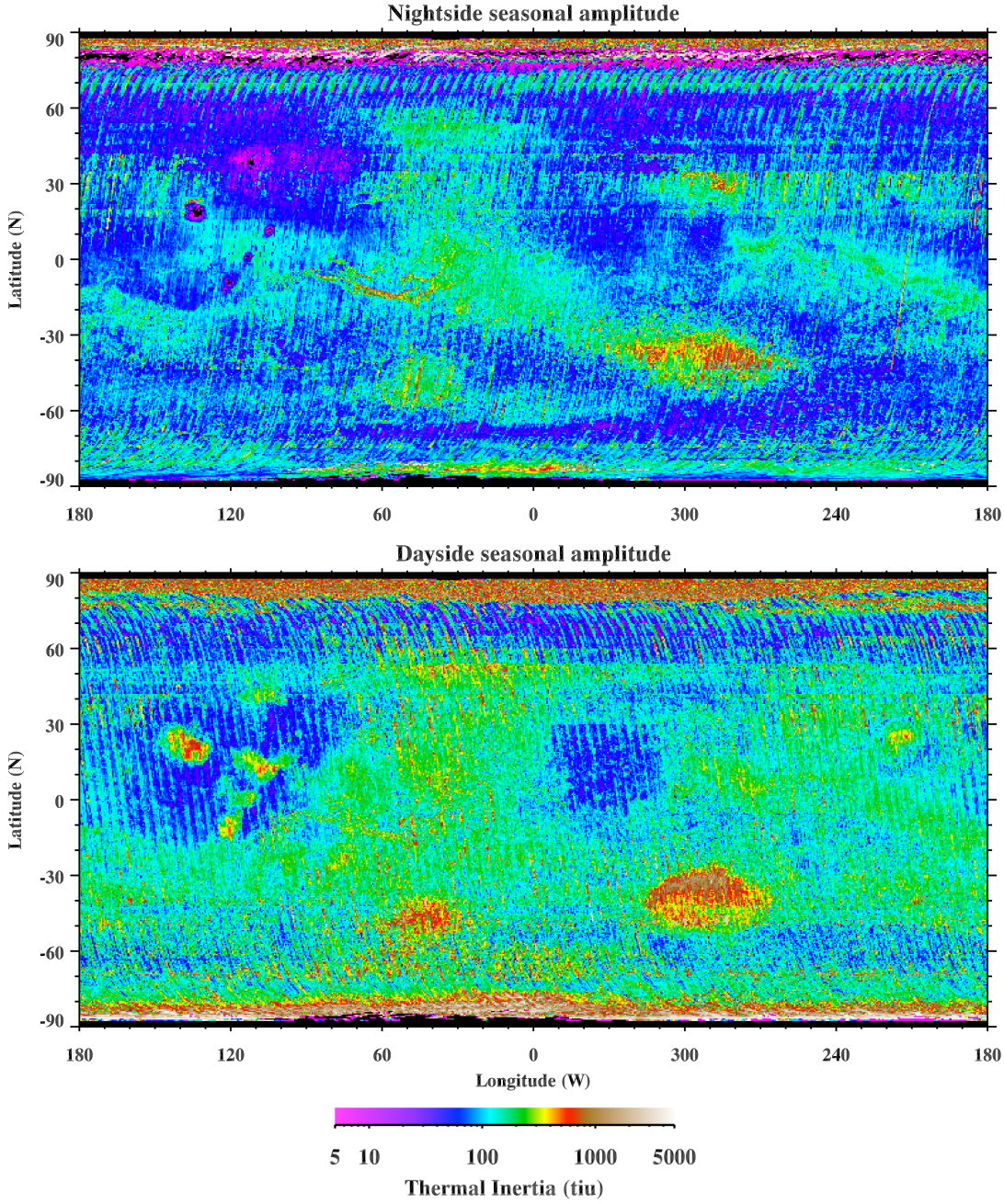

Figure 4.5 Amplitude of seasonal variation in TES apparent thermal inertia for nightside (top) and dayside (bottom), using unfilled seasonal maps binned at $\frac{1}{2}^\circ$ per pixel. Black pixels respresent no-data locations. Nightside or dayside amplitudes greater than 50 tiu are ubiquitous, suggestive of widespread surface heterogeneity.

erogeneity (Chapter 3 Mellon and Putzig 2006). The ubiquitous nature of the variability suggests that the surface of Mars is heterogeneous nearly everywhere

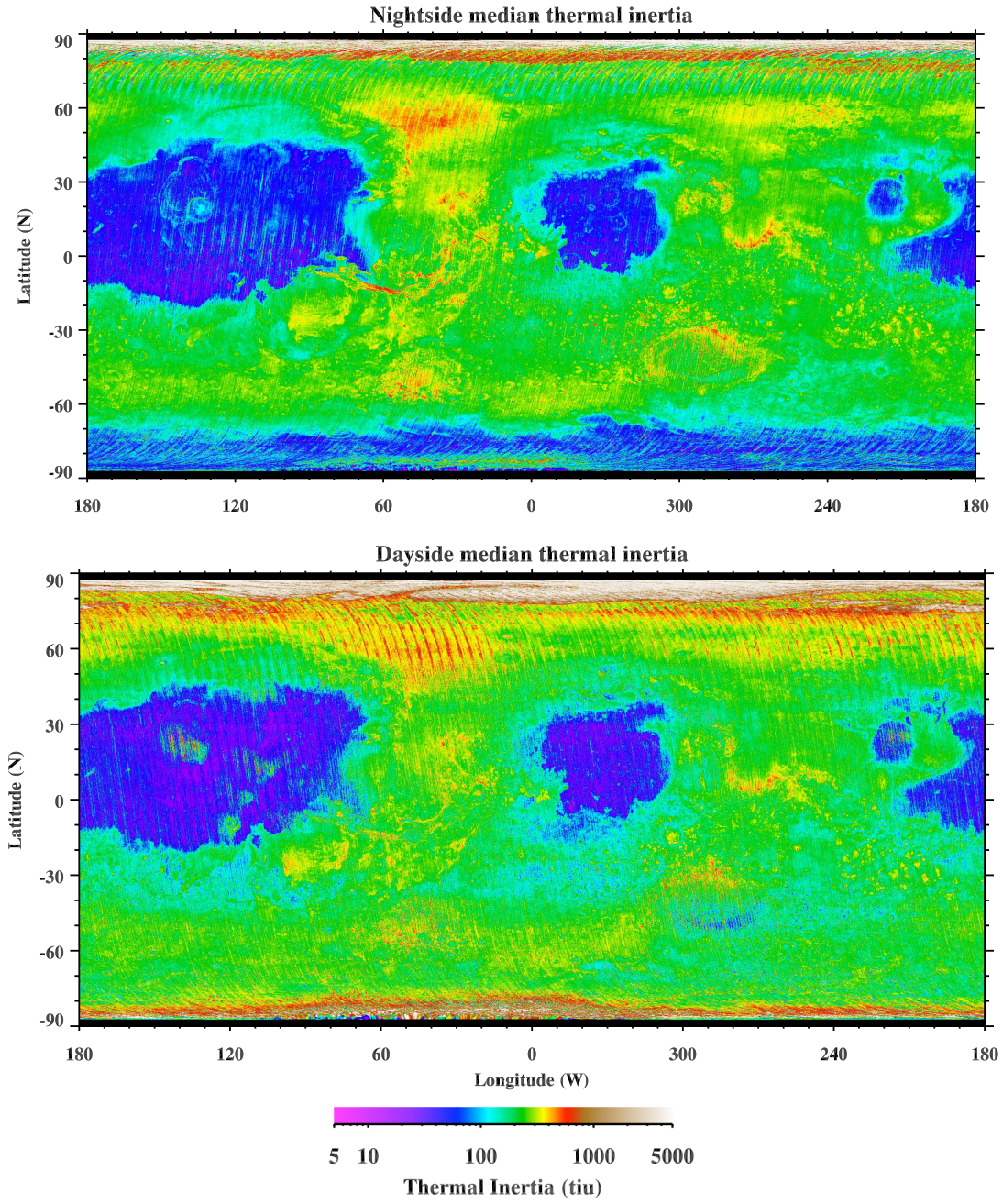

Figure 4.6 Median of 36 seasonal maps of TES global nightside (top) and dayside (bottom) bolometric apparent thermal inertia, at $\frac{1}{20}^\circ$ per pixel. Maps were infilled between 87 °S and 87 °N latitude for display purposes. Nightside values are generally higher at mid-latitudes and lower in the polar regions than dayside values.

at TES scale ($\sim$3 km).

Nightside and dayside global maps of apparent thermal inertia created by

selecting the median of the seasonal maps for each $\frac{1}{20}^\circ$ pixel are presented in Fig. 4.6. While grossly similar at mid-latitude—exhibiting similar patterns of high and low thermal inertia—the nightside and dayside median maps have substantial regional differences. The dayside median map generally shows lower thermal inertia at mid-latitudes and higher thermal inertia in the polar regions. Both maps show orbit-track-aligned streaks, which are due to the combination of large seasonal variations and incomplete geographic coverage during any given season. These effects are more pronounced at higher latitudes, where seasonal coverage is limited and season-to-season variations are larger (see also Figs. 4.3 and 4.4). The greatest differences between nightside and dayside occur in the polar regions ($60^\circ - 90^\circ$; see Fig. 4.7). Interestingly, the increase in mapping resolution and the expansion in range of thermal inertia to include values for surface ice allows us to distinguish individual canyons and troughs in the north polar cap as well as some details of outlying permanent ice features. In the south, a dramatic difference between nightside and dayside results is evident, with a large region of low nightside apparent thermal inertia mostly absent on the dayside. A region over the south polar residual cap of elevated nightside apparent thermal inertia poleward of 80°S expands greatly on the dayside.

The nightside and dayside mapping results are largely consistent with those derived earlier from Viking and TES observations (Kieffer et al. 1977, Palluconi and Kieffer 1981, Paige et al. 1994, Paige and Keegan 1994, Vasavada et al. 2000, Jakosky et al. 2000, Mellon et al. 2000, Chapter 2). Figure 4.8 shows normalized histograms comparing our nightside and dayside TES results with the nighttime results from Fig. 2.1 and with Viking results from Palluconi and Kieffer (1981) and Jakosky et al. (2000). Jakosky et al. (2000) reprocessed Viking data using the same algorithm as that used in Chapter 2, which included atmospheric effects not considered by Palluconi and Kieffer (1981) that are largely responsible for the shift

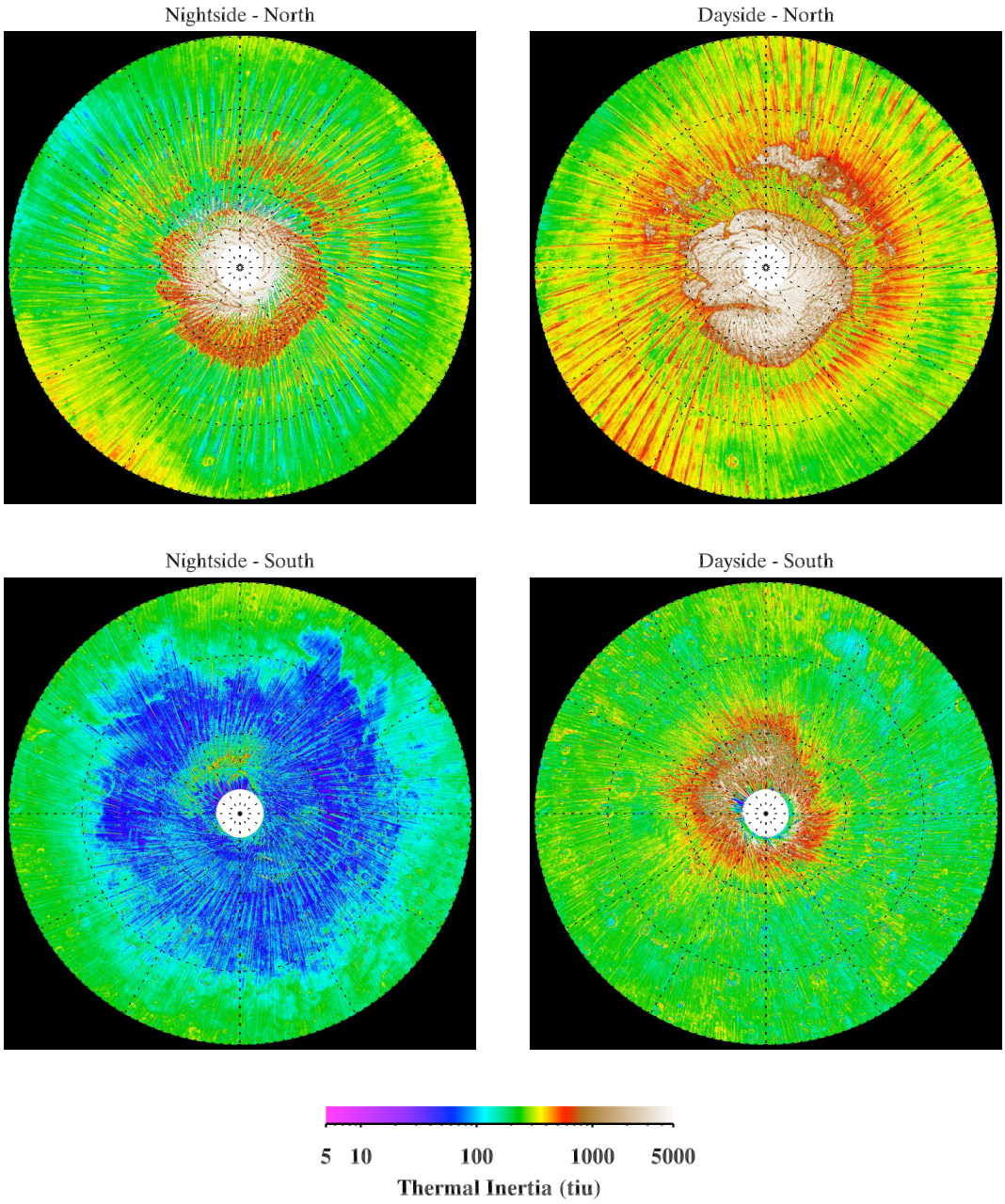

Figure 4.7 Polar-region thermal inertia. Nightside (left) and dayside (right) TES apparent thermal inertia in an orthographic project for the north (top) and south (bottom) polar regions, 60° to 90° latitude in each hemisphere. Maps show large differences between nightside and dayside values, and seasonal variability is manifested as orbital-track-aligned streaks.

between the two Viking curves in Fig. 4.8. Many artifacts of high thermal inertia

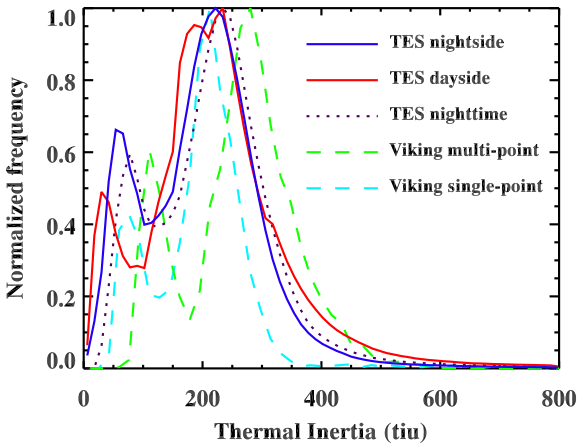

Figure 4.8 Normalized Histograms of global thermal inertia as derived from TES for our median nightside (blue) and dayside (red) results; from TES for previous nighttime results (dotted purple; Fig. 2.1); from Viking using the multi-point method and no atmospheric corrections (dashed green; Palluconi and Kieffer 1981); and from Viking using the single-point method with atmospheric corrections (dashed light-blue; Jakosky et al. 2000). All show a similar bimodal distribution. See text for further discussion.

seen in previous TES maps have been reduced or eliminated using our revised algorithm. The inclusion of measured dust opacity in the derivation algorithm, the choice of compositing seasons with a median rather than mean operator, and the choice of selecting data by local time (i.e., nightside) rather than by insolation angle (i.e., nighttime) are collectively responsible for greatly reducing the presence of orbital-track-aligned streaks attributable to seasonal variations. Streaks which remain are more likely to represent heterogeneities in surface characteristics (discussed below) rather than atmospheric effects or transient volatiles on the surface. These improvements are reflected in the shift between the TES nighttime and nightside curves in Fig. 4.8.

The dayside mapping results represent a new product that is critical to the analysis of seasonal variability of apparent thermal inertia and its relationship to surface heterogeneity. While dayside seasonal variations are qualitatively similar to those of the nightside, the magnitude of the dayside variations is greater, and

there is a large seasonal delay between the two trends. When compared to modeled heterogeneous-surface apparent thermal inertia, these distinct features of nightside and dayside trends allow us to distinguish more readily between potentially corresponding classes and types of heterogeneity models.

4.3.2 Local heterogeneity analysis

Figures 4.9, 4.10, 4.11, and 4.12 present local comparisons of TES-derived and heterogeneous-model apparent thermal inertia for various sites of interest. The surface models considered are horizontal mixtures and layers of two components composed of materials with properties representative of dust, sand, duricrust, and rock (Table 4.2). Tables 4.4, 4.5, 4.6, and 4.7 summarize for each site the model class and type, and where applicable, the estimated best-fit horizontal-mixing percentages or upper-layer thicknesses and the RMS of differences between the TES data and modeled apparent thermal inertia.

The locations in Figs. 4.9a–e are $5^\circ \times 5^\circ$ boxes centered at each past landing site—Viking Landers 1 and 2, Mars Pathfinder Lander, and the Mars Exploration Rover sites at Gusev and Meridiani, MER-A and MER-B. The site for Fig. 4.9f is a $20^\circ \times 7^\circ$ box centered at the specified location which represents "Region B" wherein the 2007 Phoenix landing site is presently being considered (Arvidson et al. 2006). The best-fit two-component models are all layered cases, with duricrust-over-dust model types at the Viking, Pathfinder, and Meridiani sites. The fit between the TES data and the interpolated model results (dash-dotted lines) for the Viking and Pathfinder sites is relatively good, with broadly similar seasonal variations in apparent thermal inertia and a similar relationship between the nightside and dayside behaviors. The presence of duricrust at the Viking and Pathfinder sites is well-documented (Moore et al. 1987, Moore and Jakosky 1989, Moore et al. 1999). Estimates of areal coverage by cemented and crusted soils

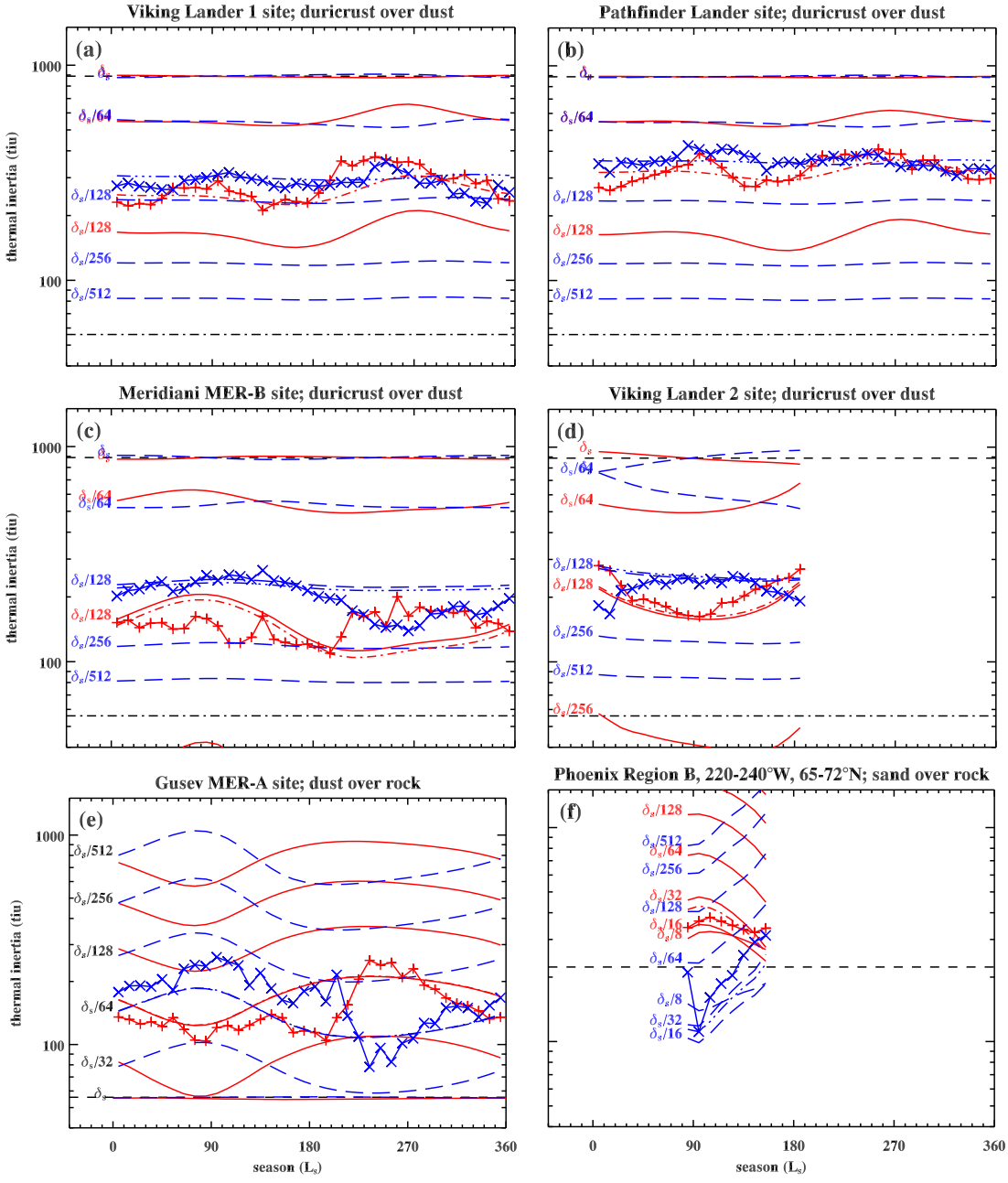

Figure 4.9 (see caption on following page)

Figure 4.9 (previous page). Comparison of apparent thermal inertia for nightside (blue) and dayside (red), showing results extracted from TES seasonal maps (×,+ symbols) and best-fitting results from two-component models (02:00 dashed, 14:00 solid) in regions surrounding five previous and one proposed (Phoenix) landing sites on Mars. Previous landing site regions are $5\,^\circ \times 5\,^\circ$ boxes centered on each site. All sites match best with the layered models shown. Colored dash-dotted curves are linearly interpolated between the bounding modeled seasonal curves to the median of the seasonal TES results. Black horizontal dashed and dash-dotted lines denote thermal inertia of model upper-layer and substrate, respectively. Model thicknesses were varied by powers of 2 relative to the seasonal skin depth, δ_S, of the upper layer. See Table 4.2 for δ_S values. The seasonal ranges for the Viking Lander 2 and Phoenix sites are restricted due to the occurrence of seasonal CO_2 frost. See text for discussion.

range as high as 86% (Moore and Jakosky 1989). Thus, it is not surprising that the thermal behavior in the regions surrounding these sites appears to be dominated by layering with duricrust-like properties. Duricrust-like materials do not appear to dominate at the Meridiani MER-B site, but similar thermal behavior may occur for the rover-observed layered surface, which contains fine sand (50–150 μm) interspersed with mm-sized hematite spherules that become concentrated at the surface (Soderblom et al. 2004). However, the best-fit match between data and model shown in Fig. 4.9c is not particularly close, deviating substantially for seasons after $L_S = 200$. If the thermal behavior seen in the data reflects surface properties, either none of the component material properties used in the modeling are appropriate, or it may be that this region is not well-represented by simple two-component material models. Similarly, nightside TES results for the Viking Lander 2 region (Fig. 4.9d) deviate significantly from the model curves and may require a more complex surface model to explain (see later discussion of slope effects). For the region surrounding the Gusev MER-A site, a layered model with dust over rock provides the best-fit to the TES data (Fig. 4.9e). This result is consistent with orbiter and rover image data, such as dark-toned dust-devil tracks, drift deposits, and dust-coated surfaces, which suggest a widespread but thin sur-

face dust layer (Golombek et al. 2006). However, there are substantial deviations between the data and model results, particularly for L_S = 70–270, and it seems unlikely that a simple two-component model will fully characterize the thermal behavior in the Gusev region.

The best-fit heterogeneous model for Phoenix Region B is nominally a sand layer over rock (Fig. 4.9f). However, ground ice would be thermally indistinguishable from rock. Such an interpretation is consistent with the analysis of Mars Odyssey Neutron Spectrometer data by Feldman et al. (2004), which suggests that near-surface ground ice is likely to be abundant in this region. Numerical modeling of ground ice stability (Mellon and Jakosky 1993, Mellon et al. 2004) suggests that such ground ice should be buried beneath a thin ($\sim$ few cm) veneer of ice-free soil, consistent with our estimate of sand thickness above the putative ground ice of $\delta_S/23$ (31 mm; see Table 4.4) as well as that of Titus et al. (2006), who found a best-fit model with a 58-mm-thick layer of sand-like material (I = 216 tiu) over a substrate with high thermal inertia (700 tiu).

Note in Fig. 4.9f how the modeled seasonal curves for $\delta_S/8$ cross those for thinner layers. In this case, a minimum nightside seasonal apparent thermal inertia occurs for $\delta_S/16$, with values that are below the layer's true thermal inertia (223 tiu). With increasing upper-layer thickness beyond this minimum, the nightside and dayside modeled seasonal curves flatten, converging much more toward the component value in earlier than in later seasons, with the dayside curves actually diverging slightly at later seasons. This behavior, which is typical for layer thicknesses between a diurnal and a seasonal skin depth, has the potential to yield non-unique solutions when estimating the upper layer thickness based on apparent thermal inertia. The match shown here is broadly representative of the north polar regions and shows a qualitatively good fit that is readily distinguishable from other model types. However, values of the RMS of differences (see Table 4.4) for

Table 4.4. Landing site best-fit layered models

Site	Location °W	°N	#	Fig.	Model Class	Type	Thickness δ_S	mm	RMS diff.† AM	PM
Viking 1	48.2	22.5	1	4.9a	layered	duricrust/dust	$\delta_S/105$	23	33	41
Pathfinder	33.5	19.1	3	4.9b	layered	duricrust/dust	$\delta_S/91$	27	30	34
Meridiani	5.5	-2.0	5	4.9c	layered	duricrust/dust	$\delta_S/133$	18	36	41
Viking 2	226.0	47.7	2	4.9d	layered	duricrust/dust	$\delta_S/126$	19	42	30
Gusev	184.5	-14.6	4	4.9e	layered	dust/rock	$\delta_S/64$	3	44	39
Phoenix	230.0	68.5	6	4.9f	layered	sand/rock(ice)	$\delta_S/23$	31	67	49

- label for location on maps in Figs. 4.13 and 4.14.

†02:00 and 14:00 RMS difference between data and model seasonal thermal inertia in tiu.

the Phoenix location—and large portions of the polar regions in general—are large enough to exceed the empirically chosen threshold for heterogeneity mapping (see Section 4.3.3).

We now consider six additional sites which have relatively close matches in apparent thermal inertia between TES data and the best-fitting two-component modeled values. The Acidalia region, near 45 °W, 55 °N, exhibits high apparent thermal inertia that varies greatly over the available seasons, resulting in the streakiness of the region as seen on the median maps in Fig. 4.6. This seasonal variation in the TES data is also evident in Fig. 4.10a and well-matched by a layered model with duricrust over dust, especially for the dayside data. At a similar latitude, the Utopia Rupes region (Fig. 4.10b) shows much less seasonal variation, with a best-fit layered model of duricrust over sand. Locations in the southern mid-latitudes at Daedalia Planum (Fig. 4.10c) and Tyrrhena Terra (Fig. 4.10d) are well-modeled by layered two-component models with dust over rock and sand over rock, respectively. For Tyrrhena Terra, the variations are much smaller, and both the data and the modeled seasonal curves oscillate around the sand thermal inertia. The latter behavior is indicative of a relatively thick sand layer, with thickness between a diurnal and seasonal skin depth. Similarly to the seasonally limited case discussed above for the Phoenix landing site, there is a potential for non-unique solutions when estimating the upper layer thickness, with the modeled apparent thermal inertia reaching a minimum near a thickness of $\delta_S/16$. At a higher latitude in the southern hemisphere, Hellas Planitia (Fig. 4.10e) shows a large ($\sim$ 150 tiu) diurnal difference in apparent thermal inertia, with a good fit using a layered duricrust-over-dust model. Slightly further south, the Icaria region (Fig. 4.10f) shows a lesser diurnal difference and is better matched with a layered duricrust-over-sand model.

In many cases, the matching algorithm may find either similar quality fits

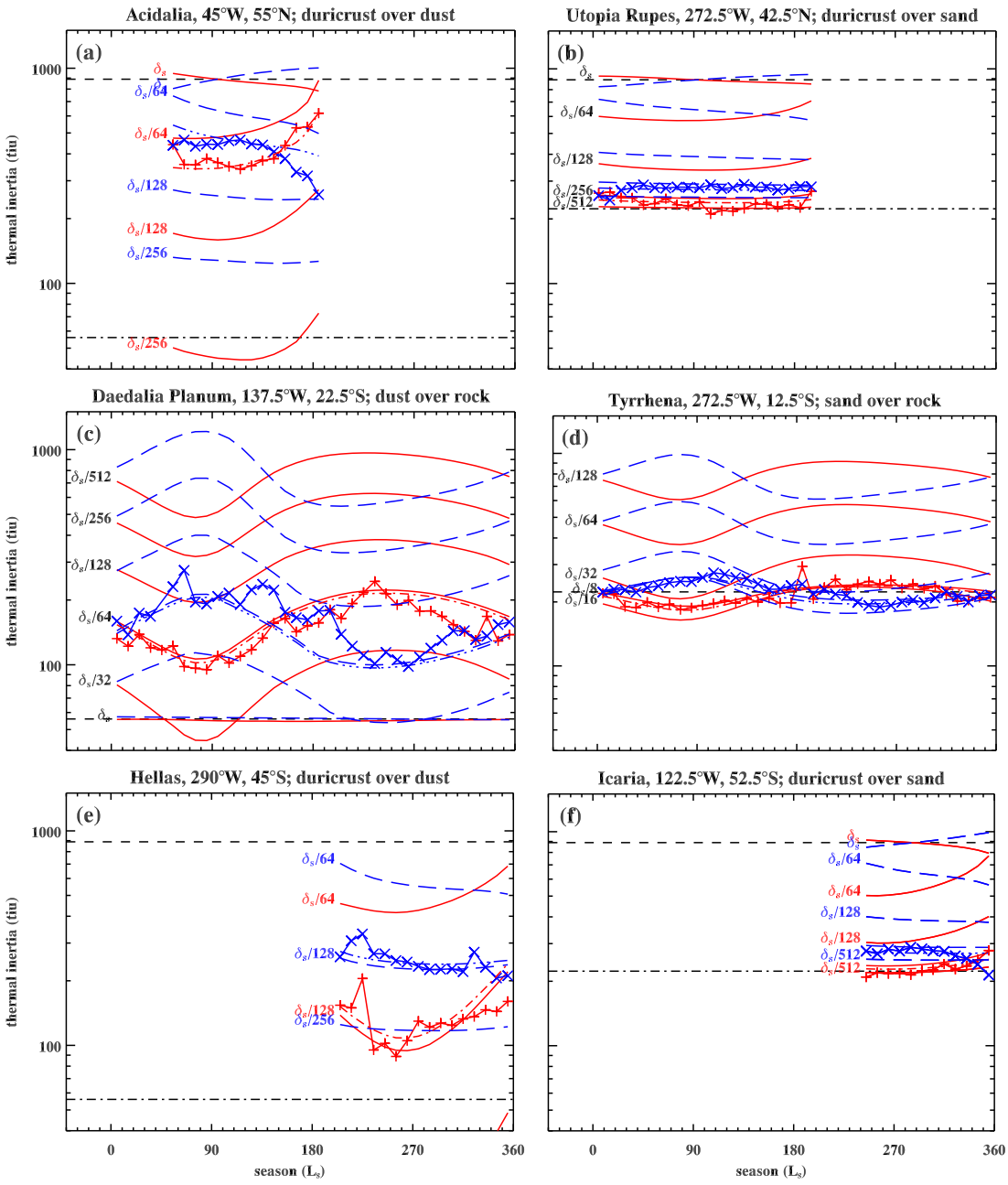

Figure 4.10 Comparison of apparent thermal inertia extracted from TES seasonal maps and best-fitting results from two-component models in six 5°×5° study regions centered on the specified locations. The seasonal ranges for Acidalia, Utopia Rupes, Hellas, and Icaria are restricted due to the occurrence of seasonal CO_2 frost. Colors and symbols as in Fig. 4.9. See text for discussion.

Table 4.5. Local best-fit layered models

Site	Location °W	°N	#	Fig.	Model Class	Type	Thickness δ_S	mm	RMS diff.† AM	PM
Acidalia	45.0	55.0	A	4.10a	layered	duricrust/dust	$\delta_S/81$	30	65	37
Utopia	272.5	42.5	U	4.10b	layered	duricrust/sand	$\delta_S/329$	7	12	14
Daedalia	137.5	-22.5	D	4.10c	layered	dust/rock	$\delta_S/60$	4	36	25
Tyrrhena	272.5	-12.5	T	4.10d	layered	sand/rock	$\delta_S/9$	78	16	16
Hellas	290.0	-45.0	H	4.10e	layered	duricrust/dust	$\delta_S/123$	20	29	36
Icaria	122.5	-52.5	I	4.10f	layered	duricrust/sand	$\delta_S/333$	7	20	12

- label for location on maps in Figs. 4.13 and 4.14.

†02:00 and 14:00 RMS difference between data and model seasonal thermal inertia in tiu.

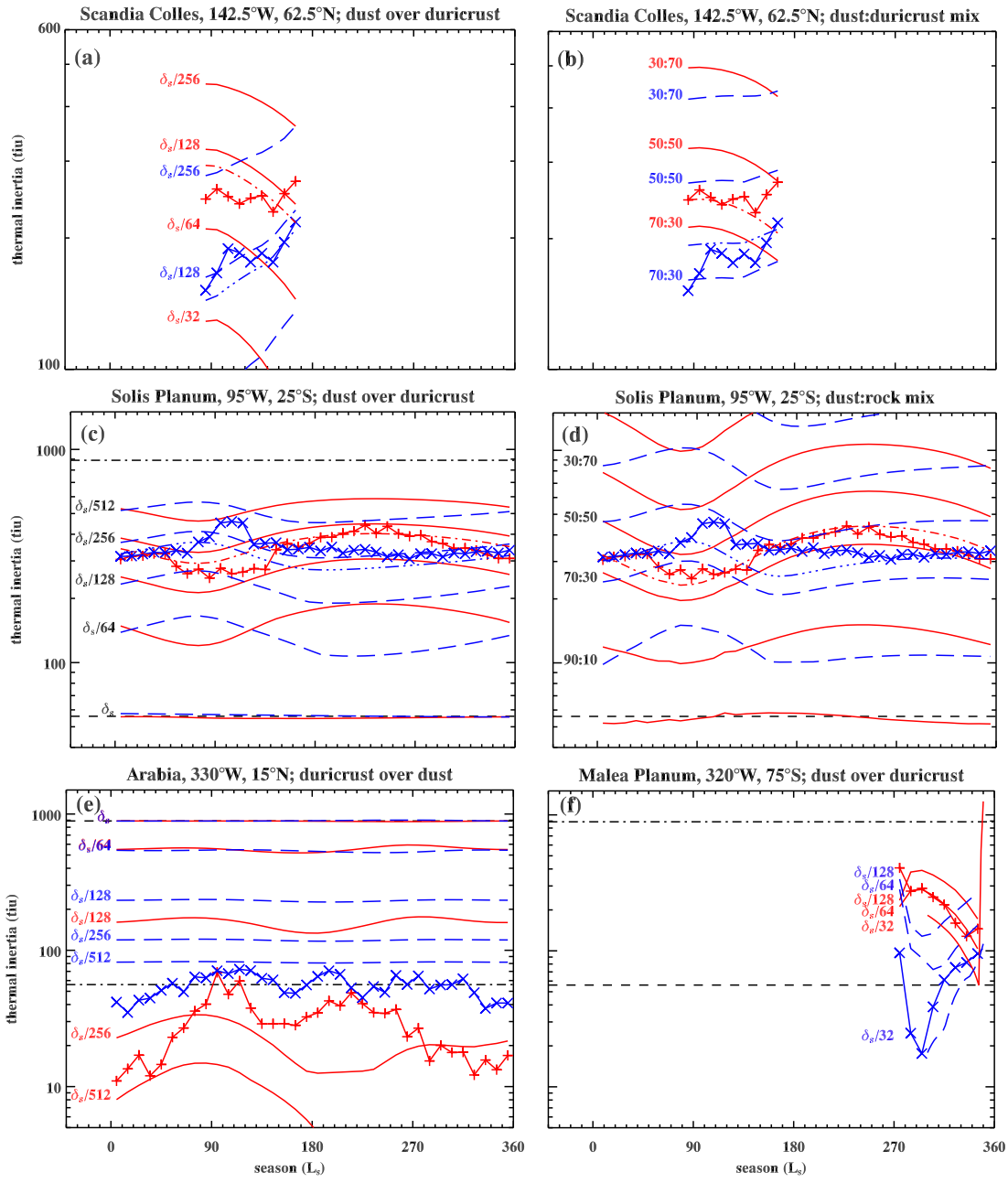

Figure 4.11 Comparison of apparent thermal inertia extracted from TES seasonal maps with ambiguous fits to two-component model results in four 5°×5° study regions centered on the specified locations. The seasonal ranges for Scandia Colles and Malea Planum are restricted due to the occurrence of seasonal CO_2 frost. Colors and symbols as in Fig. 4.9. See text for discussion.

Table 4.6. Local ambiguously fit heterogeneity models

Site	Location °W	°N	#	Fig.	Model Class	Type	Mix % or δ_S	mm	RMS diff.† AM	PM
Scandia	142.5	62.5	C	4.11a	layered	dust/duricrust	δ_S/103	2	17	33
Scandia	142.5	62.5	C	4.11b	mixed	dust:duricrust	64:36	–	21	26
Solis	95.0	-25.0	S	4.11c	layered	dust/duricrust	δ_S/194	1	52	32
Solis	95.0	-25.0	S	4.11d	mixed	dust:rock	64:36	–	53	35
Arabia	330.0	15.0	B	4.11e	layered	duricrust/dust	$\sim\delta_S$/512	5	–	–
Malea	320.0	-75.0	M	4.11f	layered	dust/duricrust	$\sim\delta_S$/56	4	–	–

#- label for location on maps in Figs. 4.13 and 4.14.

†02:00 and 14:00 RMS difference between data and model seasonal thermal inertia in tiu.

to different classes or types of model, or fail to find any match to the available two-component model results. Most of the ambiguous multiple matches are to horizontally mixed surface models and two-layer models with upper layers of lower thermal inertia. The seasonal curves for these two model classes often show similar variations and the same sign of the diurnal difference. Two-layer models with upper layers of higher thermal inertia tend to have the opposite sense of variation and difference relative to these other two model classes and are thus more readily distinguishable. Examples of this ambiguity are shown for regions in Scandia Colles (Figs. 4.11a and 4.11b) and Solis Planum (Figs. 4.11c and 4.11d). Neither model fits particularly well in either case, with the dayside generally providing a better fit to one model and the nightside to the other.

The remaining sites in this set, Arabia and Malea Planum (Fig. 4.11e and 4.11f), did not yield a match for any of the two-component models considered by our matching algorithm. Nevertheless, some insight into the nature of the surface materials may be obtained by examining such results. Arabia Terra is a continent-sized region of low thermal inertia centered near 330 °W, 15 °N (see Fig. 4.6). The seasonal TES apparent thermal inertia shown in Fig. 4.11e is representative of many portions of this and other regions of low thermal inertia that span the equator. While the layered model results shown in the figure for a duricrust-over-dust model do not provide a good quantitative fit to the data, they do demonstrate some similarities. In particular, the extremely low dayside values of apparent thermal inertia for the thinnest model cases and their relationship to their corresponding nightside values is qualitatively similar to that of the TES data. A different choice of model component thermal inertia, such as a lower dust value, clearly would improve the fit. Note that a model with an upper layer of lower thermal inertia—such as dust over duricrust as suggested by Ditteon (1982)—is not consistent with the TES results for these regions. For

such a model, nightside is lower than dayside apparent thermal inertia for the majority of seasons, whereas the TES data shows the opposite behavior. The fact that greater higher-order variability is generally present in the data and that the duricrust-over-dust layered model only provides a qualitative fit lends support to the argument of Jakosky and Christensen (1986) who proposed that a combination of factors are responsible for the thermal anomalies observed in these regions. In any event, the high albedo of these areas (see Fig. 4.2) will likely require a thin coating of bright dust atop the duricrust if such is present.

At high latitudes in both hemispheres, appropriate conditions for determining the apparent thermal inertia of the surface become very seasonally limited. At the same time, the values that can be derived show large seasonal changes. These effects can make it difficult to obtain good model fits in these regions. Despite these limitations, examination of model and data seasonal trends shows remarkably consistent behavior and a qualitatively good correspondence between the data and two-component models with upper layers of lower thermal inertia. The behavior seen for the Phoenix landing site (Fig. 4.9f) is representative of the north polar region. An example at a slightly higher latitude in the south from Malea Planum (Fig. 4.11f) shows similar characteristics in the TES data. However, the model predicts nightside CO_2-frost temperature for surface thicknesses greater than about $\delta_S/32$, especially in the earlier seasons when extremely low nightside values occur in the TES data, and no modeled values of apparent thermal inertia are obtained. This site is within the region of low thermal inertia and low albedo defined as Unit D in Fig. 2.6, which was interpreted as a region with a low-density mantle, probably overlying ice-cemented materials at depth. Although the model presented in Fig. 4.11f is for a dust-over-duricrust model, a low-density residue overlying ground ice might be expected to exhibit similar variation in apparent thermal inertia.

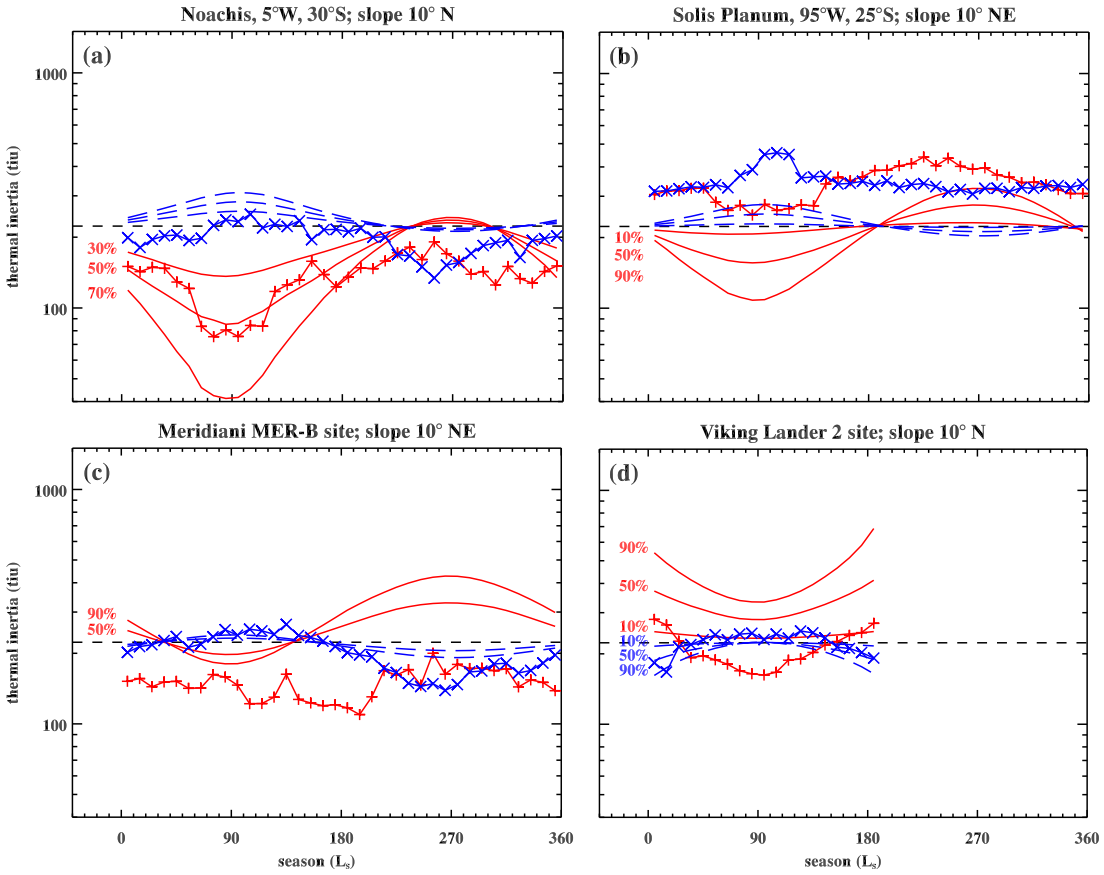

Figure 4.12 Comparison of apparent thermal inertia extracted from TES seasonal maps and results from models of partially sloped surfaces in four 5°×5° study regions centered on the specified locations. Modeled seasonal curves are labeled with sloped-area percentages. The seasonal range for Viking Lander 2 is restricted due to the occurrence of seasonal CO_2 frost. Colors and symbols as in Fig. 4.9. Horizontal dashed line denotes the thermal inertia (233 tiu) of the model material. See text for discussion.

As discussed in the previous section, sub-pixel slope variations can have substantial effects on apparent thermal inertia. Our slope modeling was limited to a single surface material ($I = 223$ tiu), five angles and five azimuths, and one uniformly sloping component and one level component per model. Thus, the quantitative methods used for matching models of heterogeneous materials to the data are not particularly useful here and we restrict our analysis of partially sloped surfaces to qualitative comparisons. Four examples are presented in Fig. 4.12.

Table 4.7. Local slope heterogeneity models

site	location °W	°N	#	fig.	model class	type
Noachis	5.0	-30.0	N	4.12a	sloped	10 °N
Solis	95.0	-25.0	S	4.12b	sloped	10 °NE
Meridiani	5.5	-2.0	5	4.12c	sloped	10 °NE
Viking 2	226.0	47.7	2	4.12d	sloped	10 °N

- label for location on maps in Figs. 4.13 and 4.14.

The one for Noachis Terra (Fig. 4.12a) shows a good match between the TES data and a model with 30–50% of the terrain sloped at 10 ° to the north. A better fit could be achieved with a lower surface-material thermal inertia of about 160 tiu. The Solis Planum location, which shows an ambiguous match to multiple-material models as discussed above (see Figs. 4.11c and 4.11d), also shows a correlation with a model of a partially sloped surface, with 10 ° slopes in a northeasterly direction (Fig. 4.12b). In this case, an increase of the surface material thermal inertia to about 350 tiu would improve the fit. Where some individual models provide only partial fits to the data, a combination of models might serve to more fully explain the observed behavior.

As shown in Fig. 4.9c, the MER-B Meridiani site is not well matched by a simple duricrust-over-dust layered model. In particular, the model mismatches are greatest near the equinoxes (L_S = 90 and 270). A model in which 50% of the region has 10 ° slopes to the northeast (Fig. 4.12c) produces diurnal difference extrema at these same seasons. If these slope effects were combined with the layered model effects, a better fit to the observed seasonal behavior at Meridiani might be expected. While the average slope in the Meridiani region makes it one of the flattest locations on the planet, widespread duneforms have been observed

and traversed by the rover—thus, regional sub-pixel slopes on the order of 10 ° are not unreasonable. At the Viking Lander 2 site, a fairly good dayside fit was found using a duricrust-over-dust model, but large deviations in the nightside data at early and late seasons were observed (see Fig. 4.9d). A model for this location using partial northward slopes of 10 ° (Fig. 4.12d) shows similar early- and late-season deviations but does not itself characterize the relationship between the nightside and dayside mean apparent thermal inertia. Here again, a combination of the layered and sloped models might result in a better overall fit to the data. However, interpretations such any these should be made cautiously, since the effects on apparent thermal inertia of different two-component models do not mix linearly (Chapter 3).

4.3.3 Global heterogeneity maps

We applied our simultaneous curve-matching algorithm globally at 5 ° intervals of longitude and latitude to produce maps of surface heterogeneity. Given the potential for ambiguous results as described above, we applied the matching algorithm separately for horizontally-mixed and layered models. No sloped-surface models were considered. The restriction of matches to those with RMS differences less than 40 tiu and 5% of the model thermal contrast was chosen by trial and error to remove spurious matches. Maps of matches for models of horizontally mixed materials, showing model type and areal percentage of the component with higher thermal inertia, are shown in Fig. 4.13. Similar maps in Fig. 4.14 portray matches for layered models, showing model type and upper-layer thickness relative to the seasonal skin depth. The layered models tend to dominate, with duricrust-over-dust and duricrust-over-sand layering predominately at mid-northern latitudes (20 °N – 60 °N), and layering with finer materials (dust or sand) overlying coarser materials (duricrust or rock) predominately poleward of 60 ° and near the equa-

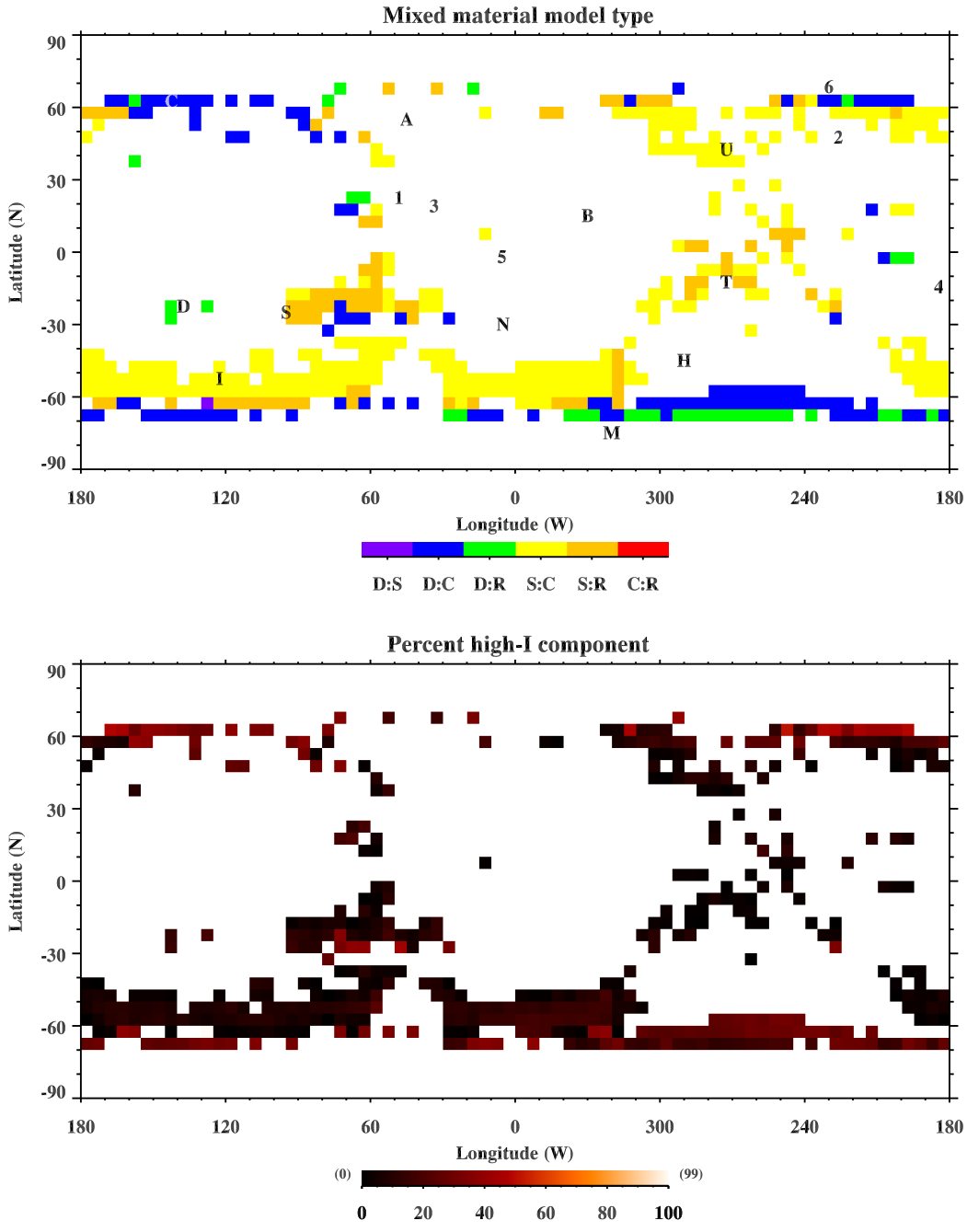

Figure 4.13 (see caption on following page)

Figure 4.13 (previous page). Global maps at 5 ° per pixel for two-component mixed materials showing model type (top) and the areal percentage of the component with higher thermal inertia (bottom) for models which correspond best to the TES seasonal and diurnal mapping results. Model components are D: dust; S: sand; C: duricrust; and R: rock. Matches are found for the model with the minimum sum of the nightside and dayside RMS of differences between data and model results. For matching purposes, a linear interpolation of the modeled seasonal curves bounding the TES data results is performed. Matches are restricted to models where the RMS differences are simultaneously less than 40 tiu and less than 5% of the difference between the component values of thermal inertia. White areas denote locations where no model meets the match criteria. Locations for landers and study sites in Figs. 4.9–4.12 are shown as 1: Viking Lander 1; 2: Viking Lander 2; 3: Mars Pathfinder Lander; 4: MER-A (Gusev); 5: MER-B (Meridiani); 6: Phoenix Lander Region B; A: Acidalia; B: Arabia Terra; C: Scandia Colles; D: Daedalia Planum; H: Hellas Planitia; I: Icaria; M: Melas Planum; N: Noachis Terra; S: Solis Planum; T: Tyrrhena Terra; and U: Utopia Rupes. See text for discussion.

tor (30 °S – 20 °N). Where they occur, horizontally mixed dust-and-duricrust and dust-and-rock model results generally show good matches to the data.

In some cases, there is ambiguity between the horizontally mixed models and the layered models of dust over duricrust, dust over rocks, or sand over rocks. Matches for horizontally mixed sand-and-duricrust and sand-and-rocks models, whether isolated or co-located with layered duricrust-over-dust or duricrust-over-sand matches, are typically consistent with either sand-dominated surfaces or thin duricrust layers ($< \sim \delta_S/200$), showing relatively little seasonal or diurnal variation. Where ambiguities occur, the layered model results usually provide a slightly better fit to the data (see Fig. 4.11 and Table 4.6). Large, contiguous swaths of mixed sand-and-duricrust and sand-and-rock matches between 40 °S and 65 °S show nearly 100% sand. Actual data variations there are better fit by layered models with a relatively thin duricrust over sand (e.g., Fig. 4.10f) or relatively thick sand over rock. In the white areas of the heterogeneity maps, no match was found that met the selection criteria. However, these locations exhibit thermal inertia behavior that is indicative of a heterogeneous surface of one type or

another. As shown earlier in Fig. 4.5, all locations show variable apparent thermal inertia at $\frac{1}{2}^\circ$ resolution, and thus unmatched locations on the heterogeneity maps (Figs. 4.13 and 4.14) should not generally be construed as representing homogeneous surfaces. Some locations in these areas may still provide reasonable matches to two-component models either quantitatively (e.g., Acidalia and Malea Planum) or qualitatively (e.g., Arabia Terra), or they may not be well represented by the single two-component models considered here (e.g., Meridiani). Some surfaces may require models with three or more components, potentially including divergent slopes, to characterize their thermal behavior. Each additional component adds another layer of complexity and increases the likelihood of ambiguous multiple solutions (Chapter 3). For particular locations, other sources of data, such as observations from landed spacecraft, may constrain modeling parameters and help to discriminate between the possible solutions.

Christensen (1986b) produced a map of rock abundance for 40 °S–60 °N using a spectral differencing technique applied to Viking IRTM observations.[5] A general correspondence is observed when comparing his map to our maps of horizontally mixed model matches (Fig. 4.13). Regions showing good agreement between the TES data thermal inertia behavior and that of horizontally mixed models typically exhibit high rock abundance on the Christensen (1986b) map (e.g., mixed dust-and-duricrust regions near Scandia Colles and mixed sand-and-rock regions near Solis Planum in Fig. 4.13), but there are some locations showing agreement that exhibit lower rock abundance (e.g., mixed dust-and-rock regions between 30 °S and 30 °N in Fig. 4.13) and there are many locations of high rock abundance that do not display matches (e.g., regions surrounding Acidalia and the Viking and Pathfinder lander sites). Our mixed-surface heterogeneity maps show regions with thermal behavior which may be dominated by horizontally

[5] See Fig. A.5 in the Appendix.

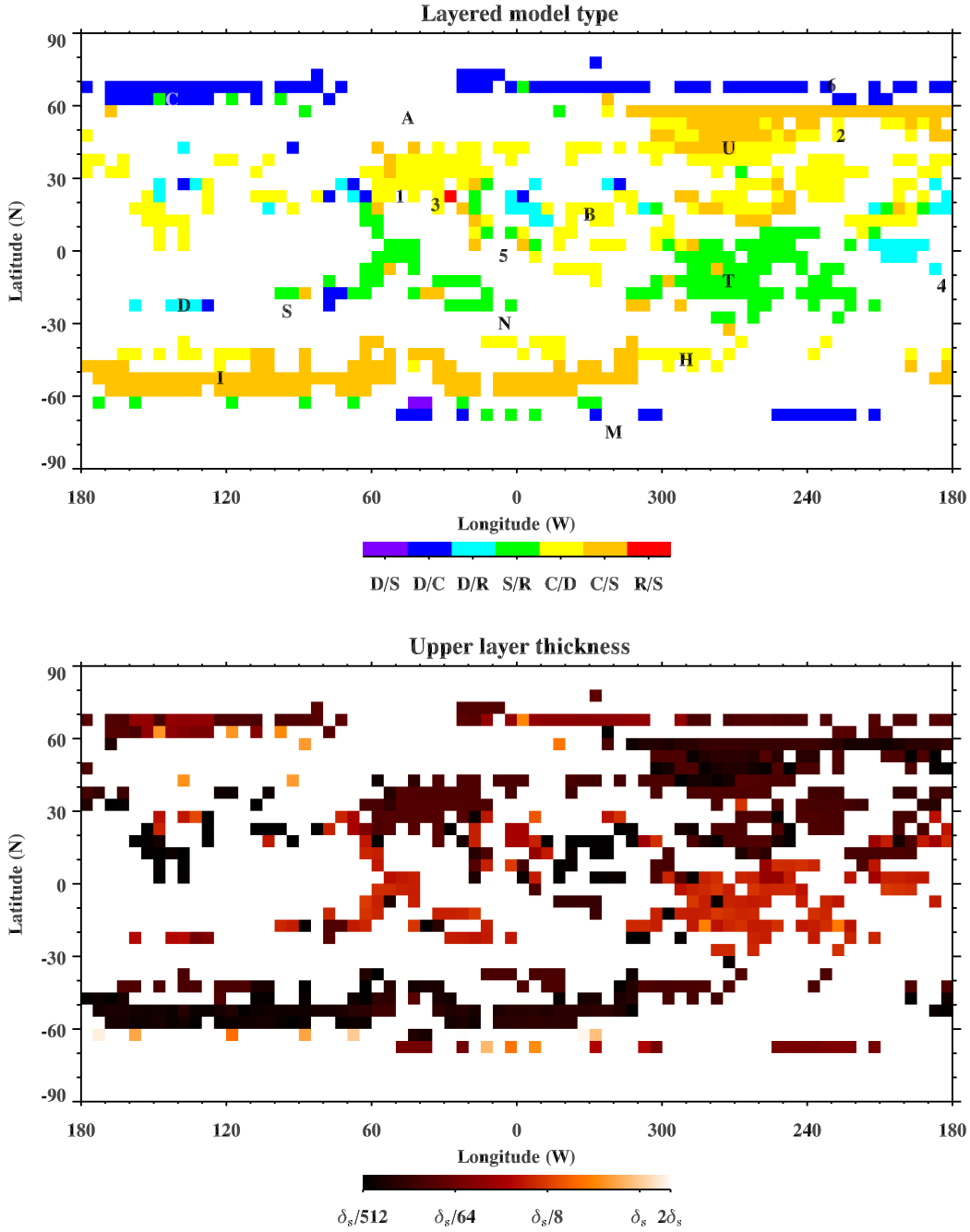

Figure 4.14 Global maps at 5° per pixel for two-component layered materials showing model type (top) and thickness of the upper layer in units of seasonal skin depth (bottom) for the models which correspond best to the TES seasonal and diurnal mapping results. Model components are D: dust; S: sand; C: duricrust; and R: rock. Matching criteria and locations are the same as in Fig. 4.13. See See Table 4.2 for material δ_S values and text for discussion.

mixed materials, regardless of the component grain sizes. In contrast, locations with high rock abundance on the Christensen (1986b) map do not necessarily have thermal characteristics which are dominated by horizontal mixtures. In fact, Christensen (1986b) himself concluded that the surface bulk thermal inertia is generally driven by the finer components and not by the rock abundance. His conclusion is consistent with our assertion that subsurface layering—rather than horizontal mixing—is the primary cause of the variations in apparent thermal inertia seen in the TES data.

In another analysis of Viking IRTM observations, Ditteon (1982) mapped differences between temperatures computed from a thermal model with homogeneous material properties and those observed in the Viking 20-μm band. He found large, anomalous differences over broad regions that correspond closely to the equatorial low-thermal-inertia, high-albedo regions (i.e., Unit A in Fig. 2.5). Ditteon (1982) used a two-layer thermal model to fit the observed diurnal temperatures, assuming a constant thermal inertia of 1250 tiu for the lower layer and allowing the upper layer thermal inertia and albedo to vary. He concluded that the anomalous temperatures in these regions could generally be explained by a layered surface with about one diurnal skin depth ($\sim$1 cm) of dust overlying a duricrust. His conclusion is somewhat in conflict with our interpretation of a layer of duricrust overlying dust in Arabia Terra (see previous discussion in Section 4.3.2 and the area around location B in Fig. 4.14). However, there are other regions in Fig. 4.14 that correspond to different portions of the anomalous regions mapped by Ditteon (1982), where TES data is matched by models with dust overlying duricrust or rocks. It appears that layering with high-over-low thermal inertia was not considered in Ditteon's analysis, and it is unclear how the diurnal temperature effects of such layers might differ from those of layering with low-over-high thermal inertia that he did consider. While his attributing of the

scatter in residual diurnal temperatures to spatial variations of thermal inertia and albedo within his study regions is plausible, it is possible that seasonal variations due to other forms of surface heterogeneity may be a significant contributing factor. Ditteon (1982) did not include a separate analysis of seasonal variability, which can provide a means of distinguishing between potentially ambiguous models (Chapter 3, Mellon and Putzig 2006). In general, our results indicate a wider range of layering types in these regions of low thermal inertia than that suggested by Ditteon (1982). As noted earlier, these regions do pervasively exhibit high albedo, which is a likely indicator of a widespread coating of bright dust. Nevertheless, our results suggest that any such dust coating is probably much thinner than a diurnal skin depth where high-over-low thermal inertia layering appears to dominate the thermal behavior.

4.4 Summary and implications

We enhanced the thermal model and thermal inertia derivation algorithm originally developed by Mellon et al. (2000) for processing TES observations of bolometric brightness temperatures on Mars. Our enhancements included an expansion of the modeled ranges of thermal inertia and surface pressure, incorporation of measured dust opacity, an approximate correction for slope, and improvements in temporal and spatial resolution for albedo and other ancillary data. Using this new algorithm, we reprocessed three Mars years of TES observations and then mapped the results to produce seasonal nightside and dayside maps of apparent thermal inertia at $\frac{1}{20}^\circ$ per pixel. These maps show systematic diurnal and seasonal variations in apparent thermal inertia that we attribute to surface heterogeneities at horizontal scales less than the TES instrument resolution ($\sim$3 km) and at vertical scales less than a seasonal skin depth below the surface. Maps of the amplitude of these nightside and dayside seasonal variations (Fig. 4.5) demon-

strate the ubiquitous nature of surface heterogeneity at TES scales.

To evaluate the potential for surface material and slope heterogeneity as an explanation for the diurnal and seasonal variability seen in the TES results, we used modified versions of the thermal model (Chapter 3 Mellon and Putzig 2006) to generate apparent thermal inertia for idealized two-component surfaces with horizontally mixed materials, partially sloped surfaces, and layered materials. The amplitude and frequency of diurnal and seasonal variability in the heterogeneous-surface model results corresponds quite closely with similar variations observed in TES-derived thermal inertia. In many locations, close matches can be found between individual models and the TES data, which suggests that, while the surface itself is likely to be more complex than a simple two-component model, in many cases the thermal behavior of the surface may be dominated by the spatial relationships of one or two types of material. The horizontally-mixed and layered model classes may be divided into four distinct subclasses, namely material mixtures, slope mixtures, two-layer models with upper layers of lower thermal inertia, and two-layer models with upper layers of higher thermal inertia. The material mixtures and two-layer models with upper layers of lower thermal inertia tend to exhibit similar behavior which can lead to ambiguous matches with the TES data. In comparison, the two-layer models with upper layers of higher thermal inertia generally show the opposite behavior, lending a higher level of confidence to any correlation found with these models. Slope mixtures exhibit a third style of behavior that is highly variable with azimuth (Fig. 3.8), making them something of a wild card. In regions where a single two-component model does not fully characterize the thermal behavior, inclusion of a second model may improve the fit. However, such multiple-model fits are highly speculative and likely to be non-unique, given the potential for ambiguity between different types and classes of models. The partially sloped model behavior is of particular concern, given

its high degree of variability and the fact that, apart from a few very-localized observations made from landed spacecraft, we have virtually no 'ground truth' for sub-pixel slope variability. More realistic slope modeling, perhaps based on detailed observations from landed spacecraft, would help address this concern.

An automated matching scheme was developed to produce 5° maps of material heterogeneity for horizontal mixtures and layers (Fig. 4.14 and 4.13). Given the aforementioned limitations and the poorly constrained uncertainties discussed in Section 4.2.4, the heterogeneity mapping results should be interpreted in the broadest sense. Rather than focusing on individual results, one might consider, for example, dark (purple to green) areas in Fig. 4.14 as likely representing surfaces dominated by layering with an upper layer of lower thermal inertia, and light (yellow to red) areas as surfaces dominated by layering with an upper layer of higher thermal inertia.

As mentioned earlier, the multi-point derivation technique used previously to process Viking observations derives values of both thermal inertia and a "thermally derived" albedo (Palluconi and Kieffer 1981). Separate albedo determinations were also made from broadband visible-spectrum observations and large differences between the derived and observed albedo were found. This discrepancy has never been fully explained (Hayashi et al. 1995). Because the multi-point method forces a single thermal inertia and a single albedo value from multiple observations, any deviation from constant material properties, such as would occur for heterogeneous surfaces, will result in errors in both thermal inertia and albedo. A re-examination of Viking results to determine whether surface heterogeneity actually explains the Viking albedo discrepancy may be warranted.

The variations in apparent thermal inertia derived from TES observations and their correspondence to heterogeneous-surface modeling results have important implications for a broad range of Mars exploration activities. Nearly all

studies to-date which have employed thermal inertia use fixed values for any given location obtained from annually averaged mapping results. Use of these fixed values to infer surface geological characteristics, such as grain size, rock abundance, and the presence of duricrusts or bedrock may yield erroneous results. Studies which focus on temporally variable phenomena—such as the exchange of volatiles with the subsurface, condensation of volatiles on the surface, past and present climate modeling, and atmospheric circulation and dust storms—may be greatly affected by seasonal and diurnal variations in apparent thermal inertia. For these purposes, it is unlikely that fixed annually averaged values are sufficient to fully characterize the surface layer, whether or not they represent the annual mean behavior. The process of landing-site selection draws on these and other studies for the purposes of evaluating the scientific potential of a site and assessing hazards to landing safety and trafficability, such as rocks, dust cover, and slopes. Climate conditions such as winds and temperature extremes may also affect both landing safety and the life of the power supply. Accurate thermal inertia is particularly important to evaluating local temperature variations. The skew in fixed values of thermal inertia due to averaging may be somewhat alleviated by the use of a median operator, but the seasonal and diurnal variations in the apparent thermal inertia are of greater importance to a better understanding of the surface properties. While relating these variations to the physical characteristics which cause them is not straightforward, the results presented here show great promise for the use of relatively simple models in constraining the nature of surface heterogeneity at particular locations on the martian surface.

Chapter 5

Discussion

> I do not know what I may appear to the world, but to myself I seem to have been only like a boy playing on the sea-shore, and diverting myself in now and then finding a smoother pebble or a prettier shell than ordinary, whilst the great ocean of truth lay all undiscovered before me.
>
> — Isaac Newton

In this closing chapter, I discuss the broader implications of the pebbles and shells overturned in the preceding chapters, beginning with a synthesis of the major conclusions reached in Chapters 2–4. Of primary importance are the diurnal and seasonal variations of apparent thermal inertia as derived from heterogeneous-surface models and TES[1] observations of Mars, which were described in Chapters 3 and 4. The analysis of these variations represents a departure from past methods of assessing thermal inertia, wherein a single value was assigned to each mapped location. Following the central chapters review, I outline general interpretation techniques for time-variable apparent thermal inertia. Orbital restrictions of recent missions preclude a full characterization of the diurnal variation in apparent thermal inertia, and I discuss some considerations for future missions regarding this issue. I conclude with suggestions for prioritizing the direct incorporation of surface heterogeneity models into algorithms designed to derive apparent thermal inertia.

[1] The Thermal Emission Spectrometer on the Mars Global Surveyor (MGS) spacecraft.

5.1 Synthesis of central chapters

The map of TES nighttime bolometric thermal inertia (Fig. 2.1), originally presented at the 2002 Lunar and Planetary Science Conference (Mellon et al. 2002), is the first global map of thermal inertia produced from TES observations spanning an entire Mars year (the MGS primary mission). This map, its early-mission predecessors (Jakosky et al. 2000, Mellon et al. 2000), and the process of their construction yielded several interesting discoveries, including new, detailed correlations with albedo and elevation, and the first realization that large diurnal differences and significant seasonal variability were present in the derived values of thermal inertia.

Modifications to the thermal model and lookup-table interpolation algorithm were undertaken, aimed at filling holes in the nighttime TES map—attributed to extremes of thermal inertia and elevation—and reducing the seasonally variable effects of atmospheric- and surface-dust cycles. Broader ranges of thermal inertia and pressure and the use of measured atmospheric opacity and annual albedo maps were included. With an additional two Mars years of observations, we obtained sufficient coverage to map nightside and dayside seasonal apparent thermal inertia (Figs. 4.3 and 4.4) at the highest possible TES resolution.

While broadly consistent with previous maps of thermal inertia from Viking IRTM[2] data (Kieffer et al. 1977, Palluconi and Kieffer 1981, Christensen and Malin 1988, Christensen and Moore 1992, Paige et al. 1994, Paige and Keegan 1994, Hayashi et al. 1995), the TES maps provides much higher spatial resolution and more complete seasonal and geographic coverage. High continuity of values within each of the seasonal maps demonstrates the ability of our method to minimize spatially variable dust-related effects and implies that inter-annual

[2] the Infrared Thermal Mapper on the Viking Orbiter spacecraft.

variations of apparent thermal inertia are small. In separate annual mappings of global thermal inertia over the included three Mars years, I found that year-to-year differences are typically less than ~ 50 tiu for most locations. In general, the apparent thermal inertia, its geographical distribution, and its seasonal behavior are highly repeatable from year to year. Geographically widespread, systematic season-to-season variations remain, with nightside and dayside variations seasonally delayed from each other. With the magnitude of both seasonal variations and day–night differences reaching several 100 tiu, well above estimates of uncertainty in the derived thermal inertia (Mellon et al. 2000, Section 4.2.4), we are confident that the temporal variations seen in the data are a true representation of the surface thermal behavior.

With each TES map, major surface units and trends found earlier in the correspondence of thermal inertia to albedo and elevation were confirmed, and new geographic units with distinct properties were identified and mapped (Mellon et al. 2000, Chapter 2; see also Fig. A.3). An anomalous region surrounding the south pole—with low nightside thermal inertia, low albedo, and a mantled appearance—is strongly suggestive of a desiccated surface layer in which very low density causes a reduction in conductivity and in thermal inertia. Similar conclusions had previously been made by others, based on lower-resolution Viking data (Paige and Keegan 1994, Vasavada et al. 2000) and images from MOC[3] and THEMIS[4] (Mustard 2003). The curious disappearance of the low thermal inertia anomaly upon the crossing of MGS over to the dayside (see Fig. 4.7) had not been anticipated, but lends support to our interpretation by suggesting the presence of a substrate with higher thermal inertia, which is likely to be shallow ground ice (see Fig. 4.11f). Another minor unit defined by high thermal inertia (Unit F

[3] The Mars Orbiter Camera on the MGS spacecraft.
[4] The Thermal Imaging System on the Mars Odyssey spacecraft.

in Fig. 2.5) contains surfaces that we expect to be dominated by rocks, bedrock outcrops, duricrusts, or exposed polar ice. In Chapter 2, portions of Unit F poleward of about 65 °N that are not associated with perennial polar ice were attributed to artifacts of processing. In our later analysis incorporating dayside observations (Chapter 4), we discovered that these high values actually result from seasonal variations in apparent thermal inertia, which are likely due to the presence of ground ice in the near subsurface (see also Section 5.2).

Chapter 2 closed with an analysis of the properties at the Viking and Pathfinder landing sites. We found that the TES thermal inertia of the regions surrounding these landers did not correlate well with the rock abundance as observed from the landers. In accordance with similar conclusions based on earlier TES and Viking results (Christensen 1986b, Jakosky and Christensen 1986, Jakosky and Mellon 2001), we suggested that other spatial variations in surface material properties, such as duricrust layers, are playing a more important role in controlling the thermal characteristics of these sites. Subsequent analysis in Chapter 4 of the seasonal variations at these sites lends further support to this conclusion.

With the TES data showing strong indications that surface heterogeneity is playing a major role in the apparent thermal inertia of Mars, we launched numerical-modeling investigations with the goal of more fully characterizing the thermal behavior of horizontal mixtures (Chapter 3) and layered surfaces (Mellon and Putzig 2006). In our horizontal-heterogeneity study—focused on mixtures of idealized materials and partially sloped surfaces—we found diurnal and seasonal variations in apparent thermal inertia up to several 100 tiu, with the amplitude of variation increasing with thermal contrast of the components and with slope angle. Extrema occur diurnally near dawn and dusk, and seasonally near the solstices, or at the earliest and latest available seasons for material mixtures in the polar regions where the usable seasonal range is limited. The nighttime and

daytime seasons of extrema typically differ by 90–180 ° of L_S, which varies with the component properties, the mixing ratio of components, and their latitude. The layered-surfaces study employed a thermal model and thermal inertia derivation algorithm modified to allow a two-layer subsurface (Mellon et al. 2004, Mellon and Putzig 2006).

Overall, the thermal behavior of modeled surfaces demonstrates that individual values of apparent thermal inertia derived from single observations of Mars are likely to have highly non-unique interpretations. Moreover, single values of thermal inertia derived from multiple observations that are sparsely sampled in time may alias the diurnal or seasonal variations and not be representative of the true surface properties. This consideration argues strongly for the use of the single-point derivation method, where the apparent thermal inertia obtained from each observation of any given location is allowed to vary with season and time of day. These variations may then be related to similar behavior seen in surface heterogeneity models, and any correlation can be used to constrain the surface properties.

For comparison to the TES data, we modeled nightside and dayside apparent thermal inertia for two-component horizontal mixtures and layers with material properties representing dust, sand, duricrust, and rocks. We found a general correspondence of temporal variations in modeled apparent thermal inertia to the TES-data behavior, confirming surface heterogeneity as the dominant driver. The modeling results made it clear that both the seasonal and the diurnal variation of apparent thermal inertia are important to distinguishing between different types of surface heterogeneity. Since the TES data are essentially limited to two times of day, any effort to discriminate between potentially corresponding models by comparing their thermal behavior to that of the TES data requires a simultaneous examination of nightside and dayside seasonal behavior. To quan-

tify the fit between modeled and TES-data results, we developed a simultaneous curve-matching algorithm wherein the values of seasonal apparent thermal inertia from each model are interpolated to match their annual-median value to that of the TES data prior to applying standard curve analysis techniques. We then mapped the best-fitting model results globally at 5° resolution. Because of a potential for ambiguity between horizontally mixed surfaces and layered surfaces with upper layers of lower thermal inertia, we mapped the matches to mixed and layered surfaces separately.

Layered surfaces appear to be the dominate heterogeneous structure in most regions, both when examining the correspondence of TES data and modeled values for particular locations, and when globally mapping best-fit models using our automated matching algorithm. The thermal characteristics of the surface at mid-latitudes is generally best fit by layered surfaces with upper layers of higher thermal inertia, such as a duricrust over dust or sand, which is in keeping with earlier suggestions of widespread duricrusts based on a comparison of Viking thermal inertia and Earth-based radar data (Christensen 1986b, Jakosky and Christensen 1986). The polar regions exhibit temporal variations that are well matched by layered surfaces with upper layers of lower thermal inertia, consistent with a veneer of dry materials over shallow ground ice as suggested by earlier numerical modeling and Mars Odyssey Neutron Spectrometer data (e.g., Mellon et al. 2004, Feldman et al. 2004). Our analysis of apparent thermal inertia at specific locations found behavior remarkably consistent with simple two-component models at some locations, and indicative of more complex surfaces at others.

5.2 General interpretation of time-variable thermal inertia

In light of the results presented in Chapters 3 and 4, it is evident that the past practice of neglecting the time dimension of apparent thermal inertia—either

through considering observations from limited time periods or through averaging of results over many seasons—discards valuable information and may lead to the misrepresentation of actual surface properties. The assumption, inherent to the derivation of thermal inertia, of uniform material properties on the scale of observing-instrument resolution and within a thermal skin depth of the surface is clearly inadequate for characterizing much of the martian surface using individual observations. Nevertheless, the limitations of available computational resources compel this assumption in the absence of any independent knowledge of the surface heterogeneity. One may proceed with the uniform-properties assumption in calculating apparent thermal inertia from individual observations, and then examine the temporal variations in the values of thermal inertia thus-derived together with those from forward modeling to constrain the surface heterogeneity.

The analysis of variations in apparent thermal inertia presented in Chapters 3 and 4 presumes that the near-surface materials themselves are not in fact changing over time. The lack of large inter-annual differences discussed earlier lends some support to this assumption—in suggesting that any secular changes are small—but phenomena with seasonal or diurnal cycles may have effects which could be misconstrued as temporally invariant heterogeneity. For instance, the condensation and sublimation of CO_2 ice on the surface involves the exchange of latent heat (e.g., third term on the right in Eq. 4.1). Also, ground ice, which increases soil conductivity by the emplacement of interstitial ice around grain contacts, may be redistributed seasonally in the subsurface. To address the effects of CO_2 ice when mapping thermal inertia, we rejected data that have surface temperatures consistent with CO_2 frost and cropped regions from seasonal maps that showed signs of sub-pixel CO_2 frost effects (see Chapters 2 and 4). No attempt was made to account for possible variations in near-surface ground ice. Modeling of ground ice (e.g., Tokano 2003, Mellon et al. 2004) suggests that seasonal

redistributions in subsurface ice content are expected to occur. However, Mellon et al. (2004) found that seasonal oscillations of the depth to the ice table are insignificant when the ice table is deeper than about 7 mm, and their map of ice table depth indicates that ice stability at shallower depths is extremely limited geographically. With the exception of a few high-latitude regions, temporal variability in true near-surface thermal inertia is not likely to be a major complication for the interpretation of apparent thermal inertia.

Our analysis has shown that different classes of heterogeneity have distinct seasonal and diurnal thermal behavior, and TES apparent thermal inertia generally exhibits similar patterns of variation. Thus, a qualitative assessment of heterogeneity is relatively straightforward for much of the martian surface. Quantitative analysis of heterogeneity is more challenging, being encumbered by the possibility of non-unique solutions and highly dependent on the choice of model complexity and specific component properties. By incorporating other sources of information, such as albedo, surface roughness from radar observations, composition from spectral analysis, and visible images from orbiters and landers, the suite of possible models may be narrowed. The incorporation of such supplementary data is likely to be critical to evaluating more complex thermal behavior that is not well modeled by simple two-component surface models (e.g., at the Meridiani site in Fig. 4.9c).

An example of the misrepresentation of surface properties in earlier mapping results is the high TES nighttime thermal inertia seen in the north polar region in Fig. 2.1. In Chapter 2, we had suggested that either unresolved atmospheric phenomena or lookup-table interpolation errors might be responsible for these high values where they do not coincide with polar ice. Upon examining the seasonal and diurnal behavior, it appears that these high values are from late-summer observations when the Sun is below the horizon–and hence are selected

for nighttime mapping—but include observations with local times near 14:00 (i.e., from the 'dayside') . With the inclusion of observations from the daytime (near both 02:00 and 14:00) and the mapping separation by local time rather than by solar incidence, we now see that "nightside" (but daylit) values begin low and increase steadily, while dayside values begin high and decrease to a lesser degree, during the summer months at these latitudes. Thus, the prior nighttime mapping does not well represent the thermal properties of the near-surface in these regions, and in fact no single season or median of seasons does. It is only by examining the seasonal and diurnal patterns of variation in apparent thermal inertia and comparing them to model results that we are able to conclude with some confidence that we are observing a surface with a layer of low thermal inertia overlying a substrate of high thermal inertia. Through examining other data (i.e., the detection of subsurface hydrogen by the Mars Odyssey neutron spectrometer), we may then infer that the substrate is most likely to be ice-cemented soil.

The landing sites provide other examples of how seasonal and diurnal changes in apparent thermal inertia may be interpreted. As discussed in Chapter 4, the Viking and Pathfinder landing sites were fairly well fit by two-component layered-surface models whereas the behavior at the MER landing sites was seen to be more complex, and no good match with the two-component modeling results could be found. Despite the limitation to four types of idealized materials, we believe that our modeling results are qualitatively representative of the thermal behavior of surfaces dominated by two-component mixtures of real geological materials. Thus, we infer that the surfaces at the MER sites are not thermally dominated by two components and that characterization of these surfaces will require a more complex model. For these sites, there is a wealth of available information from the rovers and from high-resolution orbiting instruments (e.g, MOC and THEMIS), and thus the development of complex models which capture the thermal behavior

of these sites may be achievable with an acceptable level of confidence.

In recent years, methods for obtaining 100-m resolution thermal inertia from THEMIS images have been developed (Fergason and Christensen 2003, Putzig et al. 2004, Jakosky et al. 2006). As described by Putzig et al. (2004), the method used for images included here was modified from that of Mellon et al. (2000) and incorporated seasonal variations in atmospheric dust opacity, estimated from concurrent TES observations over the regions of interest. For mapping (Hynek 2004, Martínez-Alonso et al. 2005, Jakosky et al. 2006, Murphy et al. 2006), multiple nighttime THEMIS images were mosaicked together. At THEMIS resolution, horizontal surface heterogeneity is likely to still be important, and of course any thermal effects of layering will continue to be controlled by the thermal skin depth of surface materials. The orbit of the Mars Odyssey spacecraft drifts over a wider range of local times, so diurnal variations in apparent thermal inertia should nominally be better-resolved than for TES data. Large differences in thermal inertia between overlapping images with similar local times have been observed but have never been adequately explained (Putzig et al. 2004). If these differences are the result of surface heterogeneity, then they ought to correlate with the TES temporal variations to the extent that the heterogeneity is of a layered nature or occurs at horizontal scales below the THEMIS resolution.

I examined thermal inertia derived from TES observations and from a few dozen THEMIS images at two sites in the Isidis and Gusev basins (Putzig et al. 2004, Murphy et al. 2005, Martínez-Alonso et al. 2005, Jakosky et al. 2006), where large differences between overlapping THEMIS images occur (see Fig. 5.1). Upon comparing the seasonal variation of the results from each instrument, I found a rather poor correlation between their nightside seasonal variations (Fig. 5.2). The seasonal variation of TES thermal inertia for each region shows some correspondence to layered-model results (duricrust over dust for Isidis and dust over rock for

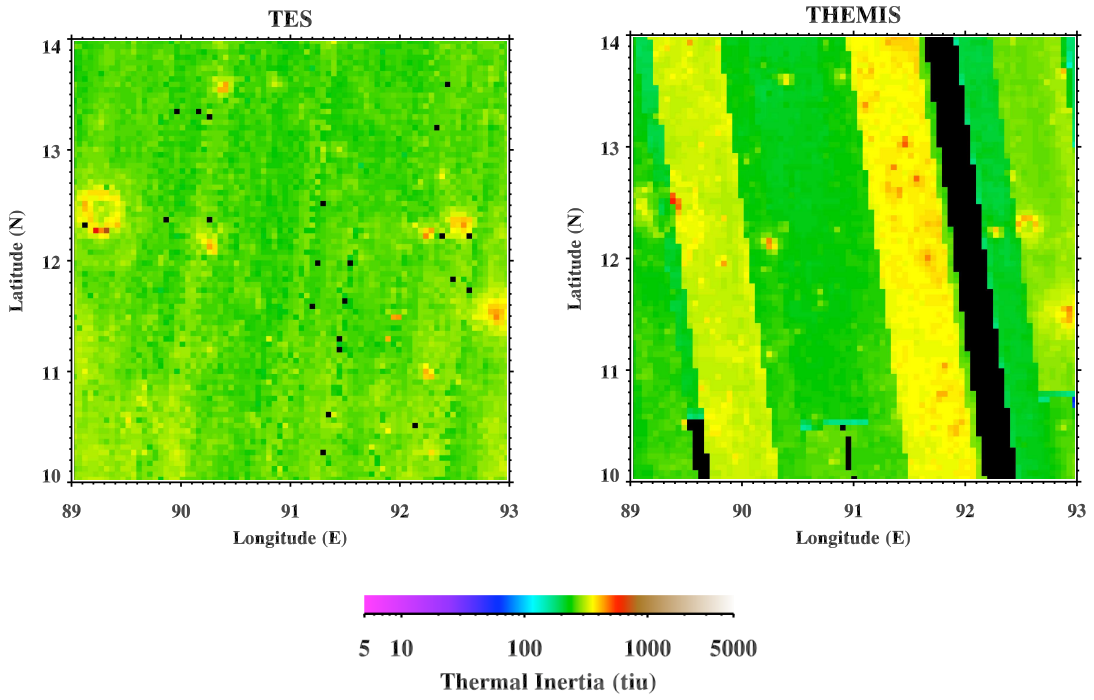

Figure 5.1 Maps of thermal inertia derived from TES and THEMIS observations for a $4\,^{\circ}\times 4\,^{\circ}$ region in Isidis Basin. The TES map is extracted from the nightside (02:00 local time) median map of apparent thermal inertia in Fig. 4.6. Portions of 20 THEMIS thermal inertia images were binned to the TES map resolution ($\frac{1}{20}\,^{\circ}$ per pixel) and are from locals times 03:10–05:20 and L_S = 10–254 (see Fig. 5.2). Large differences between overlapping images are evident in the THEMIS map.

Gusev), which suggests that effects of heterogeneity as seen by TES and THEMIS should correlate, but the correspondence between the TES and layered-model results isn't strong enough to fully support such a conclusion. Apart from a few outliers in this small sampling of THEMIS thermal inertia images, the amplitude and seasonal frequency of image-to-image temporal variations are generally of similar order to those observed in the TES and surface heterogeneity modeling results. Thus, the possibility remains that some type of surface heterogeneity may explain the differences between THEMIS images. Only a limited set of THEMIS thermal inertia images are presently available and they are generally over locations where TES results indicate complex surfaces (e.g., Isidis Basin, Meridiani

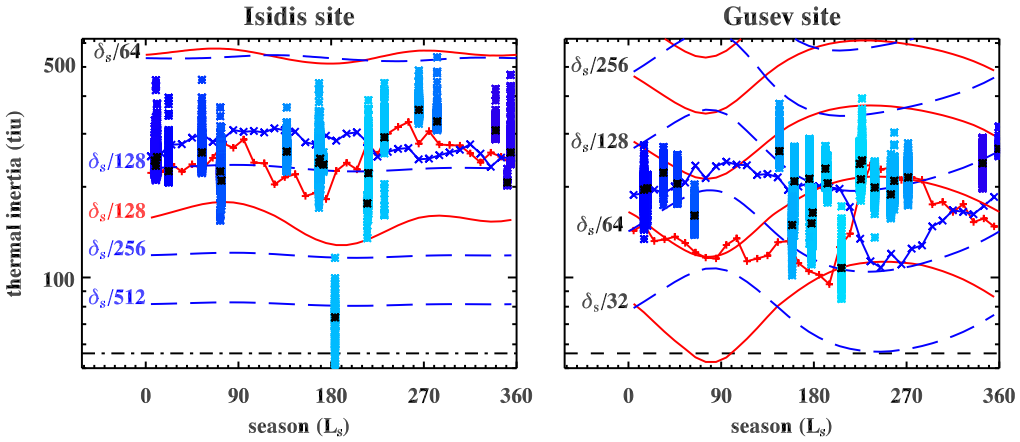

Figure 5.2 Apparent thermal inertia from THEMIS, TES, and layered models for $4\,^\circ \times 4\,^\circ$ regions in Isidis and Gusev basins. THEMIS thermal inertia images were binned to TES resolution ($\sim$3 km) and are displayed in asterisks color-coded to local time of day (darkest blue is 03:00, lightest blue is 05:30). Black asterisks are median values for each image. TES data are median values extracted from the seasonal maps (Figs. 4.3 and 4.4), with nightside values shown with a blue $\times$ and dayside with a red $+$. Best-fit layered-model curves (smooth dashed-blue and solid-red curves) for Isidis are from a duricrust-over-dust model and for Gusev are from a dust-over-rock model. Curves are labeled with upper-layer thickness relative to a seasonal skin depth (see Table 4.2). Nightside correlation between THEMIS and TES median values is poor, suggesting that the observed THEMIS image-to-image variability may not be driven primarily by seasonal variations in apparent thermal inertia.

Planum, and Gusev Crater). Processing of a suite of THEMIS images over an area where the TES temporal variations indicate a simpler layered-surface model (e.g., at the VL-1 and MPF sites) may resolve this question.

5.3 Considerations for future mission design

Orbiting spacecraft typically carry a suite of instruments with a diverse set of scientific objectives. Often there are conflicts between the optimal observing conditions and geometries for the various instruments. Thus, mission planning becomes an exercise in compromise, aimed at finding an optimal orbit that meets the requirements of each experiment without achieving the ideal conditions for any.

Recent missions (MGS, Mars Odyssey) have employed orbits with nearly fixed local times, and this restriction was a major impetus behind the development of the single-point thermal inertia derivation technique (Jakosky et al. 2000, Mellon et al. 2000). However, fixed-local-time orbits severely restrict diurnal sampling of thermal behavior that may be critical to distinguishing classes of surface heterogeneity, particularly where ambiguity between classes is a problem (i.e., horizontal material mixtures and layered surfaces with upper layers of lower thermal inertia).

General understanding of the physical properties of the near-surface would clearly benefit from frequent diurnal sampling in a long-duration mission covering many annual periods at the highest spatial resolution possible. Such a mission plan may be in conflict with that of other instruments, or even with other objectives of the same spectral instrument (e.g., TES spectral analysis of surface mineralogy, which works best in a limited range of local times Christensen et al. 1992). Over time, Mars missions have become progressively more sophisticated, with an expanding variety of instruments of ever-increasing resolution. As this trend continues, finding compromises in mission planning objectives between various instruments will become more and more challenging. For Mars, this situation may have already reached the point where it is generally more desirable to deploy several smaller spacecraft with fewer instruments rather than one large spacecraft with many instruments.

5.4 Suggestions for heterogeneous-surface derivation algorithms

Modifications to the TES thermal model (Mellon et al. 2000) have already been made to allow forward modeling of sloped surfaces and two-layered subsurfaces (see Chapters 3 and 4, Mellon et al. 2004, Mellon and Putzig 2006). By adding lookup-table dimensions of slope angle, slope azimuth, upper-layer thickness, and lower-layer thermal inertia, the effects of these parameters could be

readily incorporated into a modified derivation algorithm. Horizontal mixtures of both fixed-property components and layered-surface components could also be represented by using the technique of area-weighted mixing of temperature as described in Chapter 3. Special care would need to be taken to either accommodate or avoid situations where temperatures may have non-unique solutions for apparent thermal inertia and classes of heterogeneity.

In conjunction with slope and layered-surface modifications, the inclusion of horizontal mixtures would rapidly expand the size of the lookup table to a potentially impractical size, at least with present-day computational capabilities. For example, the current lookup table contains 4-byte values of surface and brightness temperatures for seven dimensions—84 nodes of season, 24 of time of day, 37 of latitude, 3 of dust opacity, 5 of pressure, 3 of albedo, and 21 of thermal inertia (see Tables 4.1 and 5.1). This yields a lookup-table size of 540 megabytes. Adding slope as investigated in Chapters 3 and 4 would require additional nodes of at least 6 in slope angle and 8 in slope azimuth, increasing the lookup-table size to 25 gigabytes. Including a layered subsurface with 11 nodes of upper-layer thickness (as in Chapter 4) and 21 of lower-layer thermal inertia would further increase the lookup-table size to 5.7 terabytes. Horizontal mixtures, using the seven mixing percentages employed in Chapters 3 and 4, would require a seven-fold increase in the size of the lookup table for each additional component (e.g., further increases to 40 terabytes for two-component mixtures, 280 for three, etc.).

Although disk storage of such large lookup tables is conceivable at present, the computation and interpolation of the larger all-encompassing slope-and-heterogeneity lookup tables may be impractical for many years to come. A slope-and-layered-surface lookup table is potentially near the practical limit of current resources. Slope effects may be quite large and could become increasingly important as the horizontal resolution of observations increases with future missions.

Table 5.1. Expansion of lookup table for heterogeneity

Algorithm type	Dimension	Nodes	Total size
Constant properties			
	Season	84	
	Hour	24	
	Latitude	37	
	Opacity	3	
	Pressure	5	
	Albedo	3	
	Inertia	21	540 MB
Sloped surfaces			
	Angle	6	
	Azimuth	8	25 GB
Layered surfaces			
	Thickness	11	
	Substrate inertia	21	5.7 TB
Horizontal mixtures			
2^{nd} component	Percent area	7	40 TB
3^{rd} component	Percent area	7	280 TB

Our analysis in Chapter 4 indicates that layering is generally the dominant class of heterogeneity on Mars, at least at TES resolution. Thus, an algorithm to interpolate a slope-and-layered-surface lookup table is of greater importance, and the incorporation of horizontal heterogeneity may need to be implemented either separately (i.e., horizontal-heterogeneity lookup tables without slope or layers) or through comparison with forward-modeling studies using the techniques of Chapters 3 and 4.

Of perhaps more importance than the size of the lookup table is its demand for computational resources within the associated derivation algorithm. As currently configured, lookup tables typically include many more points than are strictly required for large fractions of any given data set. For example, TES local times, with the exception of the polar regions, are nearly all within an hour of 02:00 or 14:00, and yet the current practice is to read binary subsets of the lookup table into memory that contain values for 24 times of day (as well as 84 seasons and 37 latitudes) for interpolation. Should additional dimensions be added to accommodate heterogeneous subsurface models, finer subsets of the lookup table that are more narrowly defined to correspond to the temporal and spatial bounds of each set of observations may be required.

5.5 Final remarks

The contributions to the scientific investigation of Mars summarized in this work represent five years of focused research, centered around the global and regional analysis of thermal observations, with the goal of improving our understanding of the physical properties of the surface. Together with the co-authors of the central chapters, I have wrested new insights into the surface heterogeneity of Mars from a detailed scrutiny of a large volume of data collected over a six-year period. Application of our analysis techniques at local scales promises to yield

further advancements in understanding surface geological processes, climate history, and landing-site characteristics. Studies of atmospheric circulation, volatile exchange between the atmosphere and the subsurface, and climate modeling also stand to benefit from the incorporation of time-variant apparent thermal inertia.

In thermal observations alone, a wealth of information about the surface properties of Mars is made available. When combined with other remote sensing observations—high-resolution visible imagery, narrow-band thermal spectra, neutron and gamma-ray spectra, laser altimetry, magnetometry, surface and subsurface radar soundings—the sheer volume of data overwhelms our capacity to analyze it. The press of ongoing and future missions compounds the surfeit of data and ensures that a host of discoveries await in a trove of past, present, and future observations which remain largely unexamined. A strong data analysis program will ensure many years of scientific return on the investments made in Mars exploration.

Bibliography

Adiutori, E.F., 2005. Fourier – the Father of Modern Engineering. Mech. Eng. Online, August, http://www.memagazine.org/contents/current/webonly/wex80905.html.

Arvidson, R.E., Barge, L.M., Barnes, J., Boynton, W.V., Friedson, J., Golombek, M.P., Guinn, J., Kass, D.M., Kirk, R., Malin, M., Mellon, M., Michaels, T., Paige, D., Parker, T.J., Rafkin, S., Seelos, K., Smith, M.D., Smith, P.H., Tamppari, L., Tyler, D., 2006. Overview of Mars Exploration Program 2007 Phoenix Mission Landing Site Selection. Lunar Planet. Sci. XXXVII, 1328 (abstract).

Arvidson, R.E., Guinness, E.A., Dale-Bannister, M.A., Adams, J., Smith, M., Christensen, P.R., Singer, R.B., 1989. Nature and distribution of surficial deposits in Chryse Planitia and vicinity, Mars. J. Geophys. Res. 94, 1573–1587.

Baker, V.R., Carr, M.H., Gulick, V.C., Williams, C.R., Marley, M.S., 1992. Channels and valley networks. In: Kieffer, H.H., Jakosky, B.M., Snyder, C.W., Matthews, M.S. (Eds.), Mars. Univ. of Arizona Press, Tucson, pp. 493–522.

Bandfield, J.L., 2002. Global mineral distributions on Mars. J. Geophys. Res. 107 (E6), 5042, doi: 10.1029/2001JE001510, 20 pp.

Bell III, J.F., McSween Jr., H.Y., Crisp, J.A., Morris, R.V., Murchie, S.L., Bridges, N.T., Johnson, J.R., Britt, D.T., Golombek, M.P., Moore, H.J., Ghosh, A., Bishop, J.L., Anderson, R.C., Brückner, J., Economou, T., Greenwood, J.P., Gunnlaugsson, H.P., Hargraves, R.M., Hviid, S., Knudsen, J.M., Madsen, M.B., Reid, R., Rieder, R., Soderblom, L., 2000. Mineralogic and compositional properties of martian soil and dust: Results from Mars Pathfinder. J. Geophys. Res. 105, 1721–1755.

Binder, A.B., Arvidson, R.E., Guinness, E.A., Jones, K.L., Morris, E.C., Mutch, T.A., Pieri, D.C., Sagan, C., 1977. The geology of the Viking Lander 1 site. J. Geophys. Res. 82, 4439–4451.

Boynton, W.V., Feldman, W.C., Squyres, S.W., Prettyman, T.H., Brückner, J., Evans, L.G., Reedy, R.C., Starr, R., Arnold, J.R., Drake, D.M., Englert, P.A.J.,

Metzger, A.E., Mitrofanov, I., Trombka, J.I., d'Uston, C., Wänke, H., Gasnault, O., Hamara, D.K., Janes, D.M., Marcialis, R.L., Maurice, S., Mikheeva, I., Taylor, G.J., Tokar, R., Shinohara, C., 2002. Distribution of hydrogen in the near surface of Mars: Evidence for subsurface ice deposits. Science 297, 81–85.

Bridges, N.T., 1994. Elevation-corrected thermal inertia and derived particle size on Mars and implications for the Tharsis Montes. Geoph. Res. Lett. 21, 785–788.

Chamberlain, M.A., Boynton, W.V., 2005. Effect of ground ice on apparent thermal inertia on Mars. Lunar Planet. Sci. XXXVI, 1566 (abstract).

Christensen, P.R., 1982. Martian dust mantling and surface composition: Interpretation of thermophysical properties, Age, and History. J. Geophys. Res. 87, 9985–9998.

Christensen, P.R., 1986a. Regional dust deposits on Mars: Physical properties, Age, and History. J. Geophys. Res. 91, 3533–3545.

Christensen, P.R., 1986b. The spatial distribution of rocks on Mars. Icarus 68, 217–238.

Christensen, P.R., 1988. Global albedo variations on Mars: Implications for active aeolian transport, deposition, and erosion. J. Geophys. Res. 93 (B7), 7611–7624.

Christensen, P.R., Malin, M.C., 1988. High resolution thermal imaging of Mars. Lunar Planet. Sci. XIX, 180–181.

Christensen, P.R., Moore, H.J., 1992. The martian surface layer. In: Kieffer, H.H., Jakosky, B.M., Snyder, C.W., Matthews, M.S. (Eds.), Mars. Univ. of Arizona Press, Tucson, pp. 686–729.

Christensen, P.R., Anderson, D.L., Chase, S.C., Clark, R.N., Kieffer, H.H., Malin, M.C., Pearl, J.C., Carpenter, J., Bandiera, N., Brown, F.G., Silverman, S., 1992. Thermal Emission Spectrometer experiment: Mars Observer Mission. J. Geophys. Res. 97, 7719–7734.

Christensen, P.R., Bandfield, J.L., Hamilton, V.E., Ruff, S.W., Kieffer, H.H., Titus, T.N., Malin, M.C., Morris, R.V., Lane, M.D., Clark, R.L., Jakosky, B.M., Mellon, M.T., Pearl, J.C., Conrath, B.J., Smith, M.D., Clancy, R.T., Kuzmin, R.O., Roush, T., Mehall, G.L., Gorelick, N., Bender, K., Murray, K., Dason, S., Greene, E., Silverman, S., Greenfield, M., 2001. Mars Global Surveyor Thermal Emission Spectrometer experiment: Investigation description and surface science results. J. Geophys. Res. 106, 23823–23871.

Coblentz, W.W., Lampland, C.O., 1924. Radiometric Measurements on Mars. Proc. Astron. Soc. Pacific 36, 272–274.

Colwell, J.E., Jakosky, B.M., 2002. Effects of topography on thermal infrared spectra of planetary surfaces. J. Geophys. Res. 107 (E11), 5106, doi: 10.1029/2001JE001829, 6 pp.

Ditteon, R., 1982. Daily temperature variations on Mars. J. Geophys. Res. 87 (B12), 10197–10214.

Feldman, W.C., Prettyman, T.H., Maurice, S., Plaut, J.J., Bish, D.L., Vaniman, D.T., Mellon, M.T., Metzger, A.E., Squyres, S.W., Karunatillake, S., Boynton, W.V., Elphic, R.C., Funsten, H.O., Lawrence, D.J., Tokar, R.L., 2004. Global distribution of near-surface hydrogen on Mars. J. Geophys. Res. 109 (E18), 9006, doi = 10.1029/2003JE002160.

Fergason, R.L., Christensen, P.R., 2003. Thermal inertia using THEMIS infrared data. Lunar Planet. Sci. XXXIV, 1785 (abstract).

Fergason, R.L., Christensen, P.R., Kieffer, H.H., 2006. High resolution thermal inertia derivation from THEMIS: Thermal model and applications. J. Geophys. Res., in press.

Fountain, J.A., West, E.A., 1970. Thermal conductivity of particulate basalt as a function of density in simulated lunar and martian environments. J. Geophys. Res. 75, 4063–4069.

Fourier, J.B.J., 1822. Théorie analytique de la chaleur (Analytical Theory of Heat). Republication of 1878 English tranlation by A. Freeman, Dover Publications, Inc., New York, 1955.

Geissler, P.E., 2005. Three decades of Martian surface changes. J. Geophys. Res. 110 (E2), EO2001, doi = 10.1029/2004JE002345.

Golombek, M., Rapp, D., 1997. Size-frequency distributions of rocks on Mars and Earth analog sites: Implications for future landed missions. J. Geophys. Res. 102, 4117–4129.

Golombek, M.P., Arvidson, R.E., Bell III, J.F., Christensen, P.R., Crisp, J.A., Crumpler, L.S., Ehlmann, B.L., Fergason, R.L., Grant, J.A., Greeley, R., Haldemann, A.F.C., Kass, D.M., Parker, T.J., Schofield, J.T., Squyres, S.W., Zurek, R.W., 2005. Assessment of Mars Exploration Rover landing site predictions. Nature 436, 44–48.

Golombek, M.P., Crumpler, L.S., Grant, J.A., Greeley, R., Cabrol, N.A., Parker, T.J., Rice Jr., J.W., Ward, J.G., Arvidson, R.E., Moersch, J.E., Fergason, R.L., Christensen, P.R., Castaño, A., Haldemann, A.F.C., Li, R., Bell III, J.F., Squyres, S.W., 2006. Geology of the Gusev cratered plains from the Spirit rover traverse. J. Geophys. Res. 111 (E02S07), doi: 10.1029/2005JE002503, 27 pp.

Golombek, M.P., Bridges, N.T., Moore, H.J., Murchie, S.L., Murphy, J.R., Parker, T.J., Rieder, R., Rivellini, T.P., Schofield, J.T., Seiff, A., Singer, R.B., Smith, P.H., Soderblom, L.A., Spencer, D.A., Stoker, C.R., Sullivan, R., Thomas, N., Thurman, S.W., Tomasko, M.G., Vaughan, R.M., Wänke, H., Ward, A.W., Wilson, G.R., 1999. Overview of the Mars Pathfinder mission: Launch through landing, surface operations, data sets, and science results. J. Geophys. Res. 104, 8523–8553.

Golombek, M.P., Haldemann, A.F.C., Forsberg-Taylor, N.K., DiMaggio, E.N., Schroeder, R.D., Jakosky, B.M., Mellon, M.T., Matijevic, J.R., 2003. Rock size-frequency distributions on Mars and implications for Mars Exploration Rover landing safety and operations. J. Geophys. Res. 108 (E12), 8086, doi: 10.1029/2002JE002035, 23 pp.

Golombek, M.P., Moore, H.J., Haldemann, A.F.C., Parker, T.J., Schofield, J.T., 1999. Assessment of Mars Pathfinder landing site predictions. J. Geophys. Res. 104, 8585–8594.

Haberle, R.M., Jakosky, B.M., 1991. Atmospheric effects on the remote determination of thermal inertia on Mars. Icarus 90, 187–204.

Haberle, R.M., Pollack, J.B., Barnes, J.R., Zurek, R.W., Leovy, C.B., Murphy, J.R., Lee, H., Schaeffer, J., 1993. Mars atmospheric dynamics as simulated by the NASA Ames general-circulation model. 1. The zonal-mean circulation. J. Geophys. Res. 98, 3093–3123.

Hapke, B., 1981. Bidirectional reflectance spectroscopy. 1. Theory. J. Geophys. Res. 86, 3039–3054.

Hapke, B., 1984. Bidirectional reflectance spectroscopy. 3. Correction for macroscopic roughness. Icarus 59, 41–59.

Hapke, B., 1986. Bidirectional reflectance spectroscopy. 4. The extinction coefficient and the opposition effect. Icarus 67, 264–280.

Hapke, B., 1993. Combined theory of reflectance and emittance spectroscopy. In: Pieters, C.M., Englert, P.A.J. (Eds.), Remote Geochemical Analysis: Elemental and Mineralogical Composition. Cambridge Univ. Press, Cambridge, UK, pp. 31–42.

Hapke, B., 2002. Bidirectional reflectance spectroscopy. 5. The coherent backscatter opposition effect and anisotropic scattering. Icarus 157, 523–534.

Hapke, B., Wells, E., 1981. Bidirectional reflectance spectroscopy. 2. Experiments and observations. J. Geophys. Res. 86, 3055–3060.

Hayashi, J.N., Jakosky, B.M., Haberle, R.M., 1995. Atmospheric effects on the mapping of Martian thermal inertia and thermally derived albedo. J. Geophys. Res. 100, 5277–5284.

Hynek, B.M., 2004. Implications for hydrologic processes on Mars from extensive bedrock outcrops throughout Terra Meridiani. Nature 431, 156–159.

Jaeger, J.C., Harper, A. F.A., 1950. Nature of the surface of the Moon. Nature 166, 1026–1028.

Jakosky, B.M., 1979. The effects of nonideal surfaces on the derived thermal properties of Mars. J. Geophys. Res. 84, 8252–8262.

Jakosky, B.M., 1986. On the thermal properties of martian fines. Icarus 66, 117–124.

Jakosky, B.M., Muhleman, D.O., 1981. A comparison of the thermal and radar characteristics of Mars. Icarus 45, 25–38.

Jakosky, B.M., Christensen, P.R., 1986. Global duricrust on Mars: Analysis of remote-sensing data. J. Geophys. Res. 91, 3547–3559.

Jakosky, B.M., Mellon, M.T., 2001. High-resolution thermal inertia mapping of Mars: Sites of exobiological interest. J. Geophys. Res. 106, 23887–23907.

Jakosky, B.M., Mellon, M.T., Kieffer, H.H., Christensen, P.R., Varnes, E.S., Lee, S.W., 2000. The thermal inertia of Mars from the Mars Global Surveyor Thermal Emission Spectrometer. J. Geophys. Res. 105, 9643–9652.

Jakosky, B.M., Hynek, B.M., Pelkey, S.M., Mellon, M.T., Martíinez-Alonso, S., Putzig, N.E., Murphy, N., Christensen, P.R., 2006. Thermophysical properties of the MER and Beagle II landing site regions on Mars. J. Geophys. Res. in press.

Johnson, J.B., Lorenz, R.D., 2000. Thermophysical properties of alaskan loess: An analog material for the martian polar layered terrain? Geoph. Res. Lett. 27, 2769–2772.

Kahn, R.A., Martin, T.Z., Zurek, R.W., Lee, S.W., 1992. The martian dust cycle. In: Kieffer, H.H., Jakosky, B.M., Snyder, C.W., Matthews, M.S. (Eds.), Mars. Univ. of Arizona Press, Tucson, pp. 1017–1053.

Kieffer, H.H., 1976. Soil and surface temperatures at the Viking landing sites. Science 194, 1344–1346.

Kieffer, H.H., Chase, Jr., S.C., Miner, E.D., Münch, G., Neugebauer, G., 1973. Preliminary report on infrared radiometric measurements from the Mariner 9 spacecraft. J. Geophys. Res. 78, 4291–4312.

Kieffer, H.H., Chase, Jr., S.C., Miner, E.D., Palluconi, F.D., Münch, G., Neugebauer, G., Martin, T.Z., 1976. Infrared thermal mapping of the martian surface and atmosphere: First results. Science 193, 780–786.

Kieffer, H.H., Christensen, P.R., Martin, T.Z., Miner, E.D., Palluconi, F.D., 1976. Temperatures of the martian surface and atmosphere: Viking observation of diurnal and geometric variations. Science 194, 1346–1351.

Kieffer, H.H., Martin, T.Z., Peterfreund, A.R., Jakosky, B.M., Miner, E.D., Palluconi, F.D., 1977. Thermal and albedo mapping of Mars during the Viking primary mission. J. Geophys. Res. 82, 4249–4291.

Kirk, R.L., Lee, E.M., Sucharski, R.M., Richie, J., Grecu, A., Castro, S.K., 2000. MDIM 2.0: A revised global digital image mosaic of Mars. Lunar Planet. Sci. XXXI, 2011 (abstract).

Lachenbruch, A.H., 1962. Mechanics of thermal contraction cracks and ice-wedge polygons in permafrost. Geol. Soc. Am. Spec. Paper 70, 69 pp.

Leovy, C., 1966. Note on thermal properties of Mars. Icarus 5, 1–6.

Li, R., Archinal, B.A., Arvidson, R.E., Bell III, J.F., Christensen, P., Crumpler, L., Des Marais, D.J., Di, K., Duxbury, T., Golombek, M., Grant, J., Greeley, R., Guinn, J., Johnson, A., Kirk, R.L., Maimone, M., Matthies, L.H., Malin, M., Parker, T., Sims, M., Thompson, S., Squyres, S.W., Soderblom, L.A., 2006. Spirit rover localization and topographic mapping at the landing site of Gusev crater, Mars. Journal of Geophysical Research (Planets) 111 (E10), E02S06, doi: 10.1029/2005JE002483.

Martínez-Alonso, S., Jakosky, B.M., Mellon, M.T., Putzig, N.E., 2005. A volcanic interpretation of Gusev Crater surface materials from thermophysical, spectral, and morphological evidence. J. Geophys. Res. 110 (E9), 1003, doi: 10.1029/2004JE002327.

Masamune, S., Smith, J.M., 1963. Thermal conductivity of beds of spherical particles. I & EC Fundamentals 2 (2), 136–143.

Mellon, M.T., 1997. Small-scale polygonal features on Mars: Seasonal thermal contraction cracks in permafrost. J. Geophys. Res. 102, 25617–25628.

Mellon, M.T., Jakosky, B.M., 1993. Geographic variations in the thermal and diffusive stability of ground ice on Mars. J. Geophys. Res. 98, 3345–3364.

Mellon, M.T., Jakosky, B.M., 1995. The distribution and behavior of Martian ground ice during past and present epochs. J. Geophys. Res. 100, 11781–11799.

Mellon, M.T., Putzig, N.E., 2006. Thermal behavior of layered surfaces on Mars. Manuscript in preparation.

Mellon, M.T., Jakosky, B.M., Postawko, S.E., 1997. The persistence of equatorial ground ice on mars. J. Geophys. Res. 102, 19357–19369.

Mellon, M.T., Jakosky, B.M., Kieffer, H.H., Christensen, P.R., 2000. High-resolution thermal inertia mapping from the Mars Global Surveyor Thermal Emission Spectrometer. Icarus 148, 437–455.

Mellon, M.T., Kretke, K.A., Smith, M.D., Pelkey, S.M., 2002. A global map of thermal inertia from Mars Global Surveyor mapping-mission data. Lunar Planet. Sci. XXXIII, 1416 (abstract).

Mellon, M.T., Feldman, W.C., Prettyman, T.H., 2004. The presence and stability of ground ice in the southern hemisphere of Mars. Icarus 169, 324–340.

Minnaert, M., 1941. The reciprocity principle in lunar photometry. Astrophys. J. 93, 403–410.

Mitrofanov, I.G., Litvak, M.L., Kozyrev, A.S., Sanin, A.B., Tret'yakov, V.I., Boynton, W., Hamara, D., Shinohara, C., Saunders, R.S., Drake, D., 2003. Global distribution of shallow water on Mars: Neutron mapping of summer-time surface by HEND/Odyssey. Lunar Planet. Sci. XXXIV, 1104 (abstract).

Moore, H.J., Jakosky, B.M., 1989. Viking landing sites, remote-sensing observations, and physical properties of martian surface materials. Icarus 81, 164–184.

Moore, H.J., Keller, J.M., 1990. Surface-material maps of Viking landing sites on Mars. Reports of Planetary Geology and Geophysics Program — 1989, NASA Tech. Mem. 4210, 533–535 (abstract).

Moore, H.J., Keller, J.M., 1991. Surface-material maps of Viking landing sites on Mars. Reports of Planetary Geology and Geophysics Program — 1990, NASA Tech. Mem. 4300, 160–162 (abstract).

Moore, H.J., Hutton, R.E., Scott, R.F., Spitzer, C.R., Shorthill, R.W., 1977. Surface materials of the Viking landing sites. J. Geophys. Res. 82, 4497–4523.

Moore, H.J., Hutton, R.E., Clow, G.D., Spitzer, C.R., 1987. Physical properties of the surface materials at the Viking landing sites on Mars. U.S. Geol. Surv. Prof. Pap. 1389.

Moore, H.J., Bickler, D.B., Crisp, J.A., Eisen, H.J., Gensler, J.A., Haldemann, A.F.C., Matijevic, J.R., Reid, L.K., Pavlics, F., 1999. Soil-like deposits observed by Sojourner, the Pathfinder rover. J. Geophys. Res. 104, 8729–8746.

Morrison, D., Sagan, C., Pollack, J.B., 1969. Martian temperatures and thermal properties. Icarus 11, 36–45.

Murphy, N.W., Jakosky, B.M., Rafkin, S.C., Larsen, K.W., Putzig, N.E., Mellon, M.T., 2006. Thermophysical properties of the Isidis Basin, Mars. J. Geophys. Res. in revision.

Murphy, N.W., Jakosky, B.M., Rafkin, S.C.R., Larsen, K., Mellon, M.T., Putzig, N.E., 2005. Surface properties of the Isidis Basin, Mars. Eos Trans. AGU 86 (47), Fall Meet. Suppl., Abstract P17–5430.

Mustard, J.F., 2003. First look at the thermophysical properties of the dissected mantle. Lunar Planet. Sci. XXXIV, 2005 (abstract).

Mustard, J.F., Cooper, C.D., Rifkin, M.K., 2001. Evidence for recent climate change on Mars from the identification of youthful near-surface ground ice. Nature 412, 411–414.

Mutch, T.A., Arvidson, R.E., Binder, A.B., Guinness, E.A., Morris, E.C., 1977. The geology of the Viking Lander 2 site. J. Geophys. Res. 82, 4452–4467.

Neugebauer, G., Münch, G., Kieffer, H., Chase, Jr., S.C., Miner, E., 1971. Mariner 1969 infrared radiometer results: Temperature and thermal properties of the martian surface. Astron. J. 76 (8), 719–728.

Paige, D.A., 1992. The thermal stability of near-surface ground ice on Mars. Nature 356, 43–45.

Paige, D.A., Keegan, K.D., 1994. Thermal and albedo mapping of the polar regions of Mars using Viking thermal mapper observations. 2. South polar region. J. Geophys. Res. 99, 25993–26013.

Paige, D.A., Bachman, J.E., Keegan, K.D., 1994. Thermal and albedo mapping of the polar regions of Mars using Viking thermal mapper observations. 1. North polar region. J. Geophys. Res. 99, 25959–25991.

Palluconi, F.D., Kieffer, H.H., 1981. Thermal inertia mapping of Mars from 60°S to 60°N. Icarus 45, 415–426.

Pelkey, S.M., Jakosky, B.M., 2002. Surficial geologic surveys of Gale Crater and Melas Chasma, Mars: Integration of remote-sensing data. Icarus 160, 228–257.

Pelkey, S.M., Jakosky, B.M., Mellon, M.T., 2001. Thermal inertia of crater-related wind streaks on Mars. J. Geophys. Res. 106, 23909–23920.

Pettit, E., Nicholson, S.B., 1924. Radiation Measures on the Planet Mars. Proc. Astron. Soc. Pacific 36, 269–272.

Pickett, J.P., et al., 2000. The American Heritage Dictionary of the English Language (4th ed.). Houghton Mifflin Co., Boston, MA.

Pleskot, L.K., Miner, E.D., 1981. Time variability of martian bolometric albedo. Icarus 45, 179–201.

Pollack, J.B., Haberle, R.M., Schaeffer, J., Lee, H., 1990. Simulations of the general circulation of the martian atmosphere: 1. Polar processes. J. Geophys. Res. 95, 1447–1473.

Presley, M.A., Christensen, P.R., 1997a. Thermal conductivity measurements of particulate materials. 1. A review. J. Geophys. Res. 102, 6535–6549.

Presley, M.A., Christensen, P.R., 1997b. Thermal conductivity measurements of particulate materials. 2. Results. J. Geophys. Res. 102, 6551–6566.

Presley, M.A., Christensen, P.R., 1997c. The effect of bulk density and particle size sorting on the thermal conductivity of particulate materials under martian atmospheric pressures. J. Geophys. Res. 102, 9221–9229.

Presley, M.A., Craddock, R.A., 2006. Thermal conductivity measurements of particulate materials. 3. Natural samples and mixtures of particle sizes. J. Geophys. Res., submitted.

Putzig, N.E., Mellon, M.T., 2006a. Thermal behavior of horizontally mixed surfaces on Mars. Icarus, submitted.

Putzig, N.E., Mellon, M.T., 2006b. Apparent thermal inertia and the surface heterogeneity of Mars. Icarus, submitted.

Putzig, N.E., Mellon, M.T., Jakosky, B.M., Pelkey, S.M., Martínez-Alonso, S., Hynek, B.M., Murphy, N.W., 2004. Mars thermal inertia from THEMIS data. Lunar Planet. Sci. XXXV, 1863 (abstract).

Putzig, N.E., Mellon, M.T., Arvidson, R.E., Kretke, K.A., 2005. Global thermal inertia and surface properties of Mars from the MGS mapping mission. Icarus 173, 325–341.

Ruff, S.W., Christensen, P.R., 2002. Bright and dark regions on Mars: Particle size and mineralogical characteristics based on Thermal Emission Spectrometer data. J. Geophys. Res. 107 (E12), 5127, doi: 10.1029/2001JE001580, 22 pp.

Rybicki, G.B., Lightman, A.P., 1979. Radiative Processes in Astrophysics. John Wiley & Sons, New York, NY.

Schotte, W., 1960. Thermal conductivity of packed beds. AIChE J. 16 (1), 63–67.

Sinton, W.M., Strong, J., 1960. Radiometric observations of Mars. Astrophys. J. 131, 459–469.

Smith, D.E., Zuber, M.T., Frey, H.V., Garvin, J.B., Head, J.W., Muhleman, D.O., Pettengill, G.H., Phillips, R.J., Solomon, S.C., Zwally, H.J., Banerdt, W.B., Duxbury, T.C., Golombek, M.P., Lemoine, F.G., Neumann, G.A., Rowlands, D.D., Aharonson, O., Ford, P.G., Ivanov, A.B., Johnson, C.L., McGovern, P.J., Abshire, J.B., Afzal, R.S., Sun, X., 2001a. Mars Orbiter Laser Altimeter: Experiment summary after the first year of global mapping of Mars. J. Geophys. Res. 106, 23689–23722.

Smith, M.D., 2004. Interannual variability in TES atmospheric observations of Mars during 1999–2003. Icarus 167, 148–165.

Smith, M.D., Pearl, J.C., Conrath, B.J., Christensen, P.R., 2001b. Thermal Emission Spectrometer results: Mars atmospheric thermal structure and aerosol distribution. J. Geophys. Res. 106, 23929–23945.

Smith, P.H., Bell III, J.F., Bridges, N.T., Britt, D.T., Gaddis, L., Greeley, R., Keller, H.U., Herkenhoff, K.E., Jaumann, R., Johnson, J.R., Kirk, R.L., Lemmon, M., Maki, J.N., Malin, M.C., Murchie, S.L., Oberst, J., Parker, T.J., Reid, R.J., Sablotny, R., Soderblom, L.A., Stoker, C., Sullivan, R., Thomas, N., Tomasko, M.G., Ward, W., Wegryn, E., 1997. Results from the Mars Pathfinder Camera. Science 278, 1758–1764.

Soderblom, L.A., Anderson, R.C., Arvidson, R.E., Bell III, J.F., Cabrol, N.A., Calvin, W., Christensen, P.R., Clark, B.C., Economou, T., Ehlmann, B.L., Farrand, W.H., Fike, D., Gellert, R., Glotch, T.D., Golombek, M.P., Greeley, R., Grotzinger, J.P., Herkenhoff, K.E., Jerolmack, D.J., Johnson, J.R., Jolliff, B., Klingelhöfer, G., Knoll, A.H., Learner, Z.A., Li, R., Malin, M.C., McLennan, S.M., McSween, H.Y., Ming, D.W., Morris, R.V., Rice Jr., J.W., Richter, L., Rieder, R., Rodionov, D., Schröder, C., Seelos IV, F.P., Soderblom, J.M., Squyres, S.W., Sullivan, R., Watters, W.A., Weitz, C.M., Wyatt, M.B., Yen, A., Zipfel, J., 2004. Soils of Eagle Crater and Meridiani Planum at the Opportunity Rover landing site. Science 306 (5702), 1723–1726.

Spencer, J.R., 1990. A rough-surface thermophysical model for airless planets. Icarus 83, 27–38.

Squyres, S.W., Veverka, J., 1982. Variation of albedo with solar incidence angle on planetary surfaces. Icarus 50, 115–122.

Storrs, A.D., Fanale, F.P., Saunders, R.S., Stephens, J.B., 1988. The formation of filamentary sublimate residues (FSR) from mineral grains. Icarus 76, 493–512.

Tanaka, K.L., Scott, D.H., 1987. Geologic map of the polar regions of Mars. U.S. Geological Survey. Map I-1802-C.

Titus, T.N., Prettyman, T.H., Colaprete, A., 2006. Thermal characterization of the three proposed Phoenix landing sites. Lunar Planet. Sci. XXXVII, 2161 (abstract).

Tokano, T., 2003. Spatial inhomogeneity of the martian subsurface water distribution: implication from a global water cycle model. Icarus 164, 50–78.

Touloukian, Y.S., Judd, W.R., Roy, R.F. (Eds.), 1989. Physical properties of rocks and minerals. Hemisphere Pub. Corp., New York, NY.

Turcotte, D.L., Schubert, G., 2002. Geodynamics (2nd ed.). Cambridge Univ. Press, Cambridge, UK.

U.S. Dept. of Commerce, 1996. Federal Standard 1037C: Glossary of Telecommunication Terms. NTIA, National Communications System Technology & Standards Division.

Vasavada, A.R., Williams, J.P., Paige, D.A., Herkenhoff, K.E., Bridges, N.T., Greeley, R., Murray, B.C., Bass, D.S., McBride, K.S., 2000. Surface properties of Mars' polar layered deposits and polar landing sites. J. Geophys. Res. 105, 6961–6969.

Ward, A.W., Gaddis, L.R., Kirk, R.L., Soderblom, L.A., Tanaka, K.L., Golombek, M.P., Parker, T.J., Greeley, R., Kuzmin, R.O., 1999. General geology and geomorphology of the Mars Pathfinder landing site. J. Geophys. Res. 104, 8555–8571.

Warren, S.G., Wiscombe, W.J., Firestone, J.F., 1990. Spectral albedo of CO_2 in martian polar caps: Model results. J. Geophys. Res. 95, 14717–14741.

Wechsler, A.E., Glaser, P.E., 1965. Pressure effects on postulated lunar materials. Icarus 4, 335–352.

Wechsler, A.E., Glaser, P.E., Little, A.D., Fountain, J.A., 1972. Thermal properties of granulated materials. In: Lucas, J.W. (Ed.), Thermal characteristics of the Moon. MIT Press, Cambridge, MA, pp. 215–241.

Wesselink, A.J., 1948. Heat conductivity and nature of the lunar surface material. Bull. Astron. Inst. Netherlands X (390), 351–363.

Woodside, W., Messmer, J.H., 1961. Thermal conductivity of porous media, I, Unconsolidated sands. J. Appl. Phys. 32 (9), 1688–1699.

Zeitler, W., Oberst, J., 1999. The Mars Pathfinder landing site and the Viking control point network. J. Geophys. Res. 104, 8935–8941.

Zurek, R.W., Barnes, J.R., Haberle, R.M., Pollack, J.B., Tillman, J.E., Leovy, C.B., 1992. Dynamics of the atmosphere of Mars. In: Kieffer, H.H., Jakosky, B.M., Snyder, C.W., Matthews, M.S. (Eds.), Mars. Univ. of Arizona Press, Tucson, pp. 835–933.

Appendix A

Ancillary data and maps

I'm moving to Mars next week, so if you have any boxes...

— Steven Wright

This appendix includes ancillary materials relevant to the enhancements of the derivation algorithm for thermal inertia but not included in Chapters 3 and 4. Figure A.1 shows rock-property data compiled to guide the selection of the upper bound for apparent thermal inertia. Mellon et al. (2000) produced a figure using their lookup-table nodes that shows the dependence of surface temperature on thermal inertia, albedo, atmospheric pressure, and dust opacity, and I provide in Fig. A.2 an updated version of their figure using the expanded lookup table. Figure A.3 shows updated versions of the surface-unit histograms and the thermal inertia–albedo unit map originally presented in Chapter 2, here using the TES median map of nightside thermal inertia and the albedo map for Mars Year 26. Maps of effective change in latitude and longitude used for the approximate slope correction that was applied in the most recent derivation of TES thermal inertia (Chapter 4) are shown in Fig. A.4. A map of rock abundance as derived by Christensen (1986b) is provided in Fig. A.5 for comparison to the thermal inertia and heterogeneity maps in Chapters 2 and 4 (Figs. 2.1, 4.5, 4.6, 4.13, and 4.14).

Rock Properties Table assembled 2001-09-18 by N.E. Putzig

Estimated min/max Thermal Inertias from sqrt(kρc) for various rocks at T=200-500 K
Computed from Thermal Conductivity (K), Specific Gravity (S), and Specific Heat (C)
K, S, and C values taken from graphs in Touloukian et al (1989)
Exceptions:

rock salt and gypsum densities from internet
andesite SG from Touloukian pg 36 equation
sandstone C values - used quartz values

Rock	Kmin	Kmax	Smin	Smax	Cmin	Cmax	Imin	Imax
basalt	2.00	2.50	2.00	3.10	700	1000	1673	2784
calcite	0.25	0.35	2.70	2.90	500	1000	581	1007
granite	2.00	3.00	2.30	3.00	900	1000	2035	3000
olivine	2.00	4.00	3.20	4.40	600	1100	1960	4400
pyroxene	3.00	7.00	3.00	4.00	800	1300	2683	6033
limestone	0.30	0.90	1.20	2.90	900	1100	569	1694
marble	2.00	3.00	2.50	3.20	900	1100	2121	3250
fused qtz	1.00	2.00	2.65	2.65	800	1000	1456	2302
quartzite	3.00	8.00	2.30	4.10	850	1000	2422	5727
rock salt	4.00	9.00	2.10	2.20	750	950	2510	4337
gypsum	0.30	3.90	2.30	2.30	860	1160	770	3226
andesite	1.08	1.12	2.87	2.87	450	600	1181	1389
sandstone	1.25	4.00	1.40	2.90	800	1000	1183	3406
andesite	1.08	1.12	2.87	2.87	450.00	600	1181	1389
sandstone	1.25	4.00	1.40	2.90	800.00	1000	1183	3406

Figure A.1 Data on rock properties assembled in the early stages of investigating lookup-table expansion. Selection of the upper bound for thermal inertia (5000 tiu) was based on this data, which was primarily sourced from Touloukian et al. (1989).

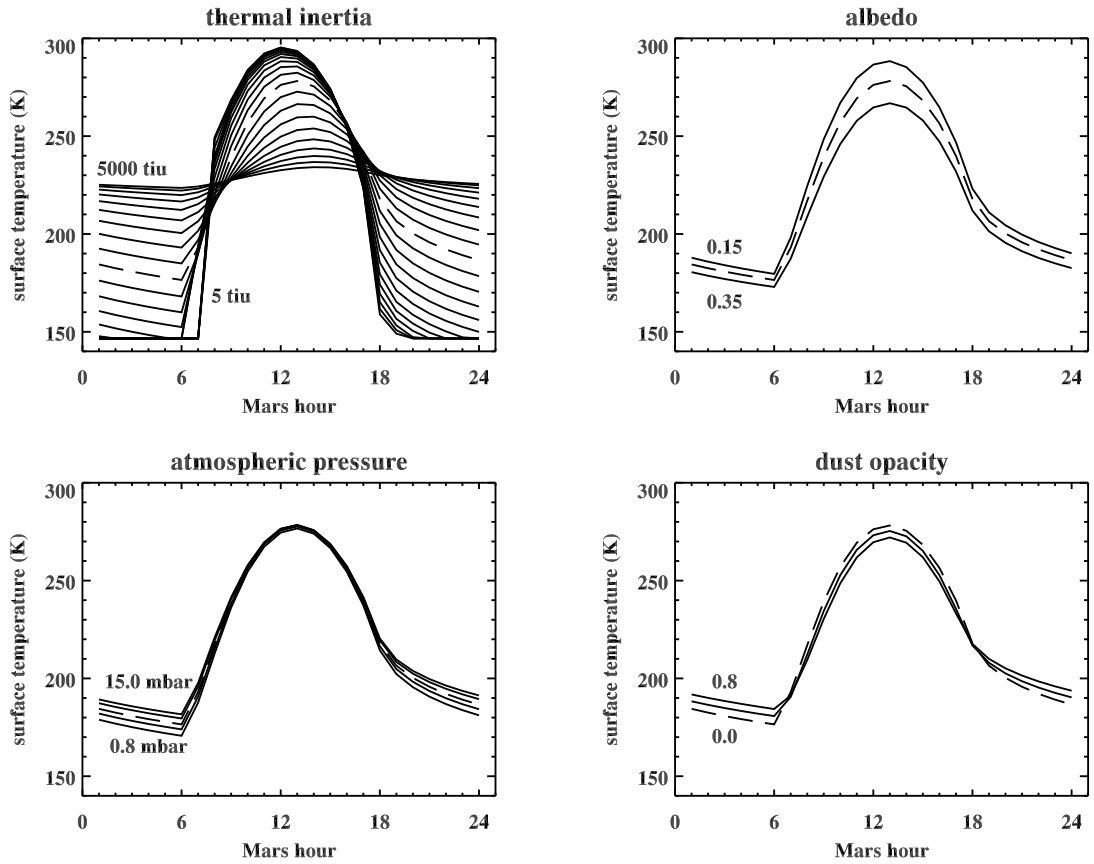

Figure A.2 Update of Fig. 1 of Mellon et al. (2000), using node values from the lookup table created for reprocessing of TES observations as described in Chapters 3 and 4 (Putzig and Mellon 2006a,b). Dashed curves are for values held constant when examining other parameters ($I = 223$ tiu, $A = 0.25$, $P = 5$ mbar, $\tau_{\mathrm{D}} = 0.0$). See Table 4.1 for other node values.

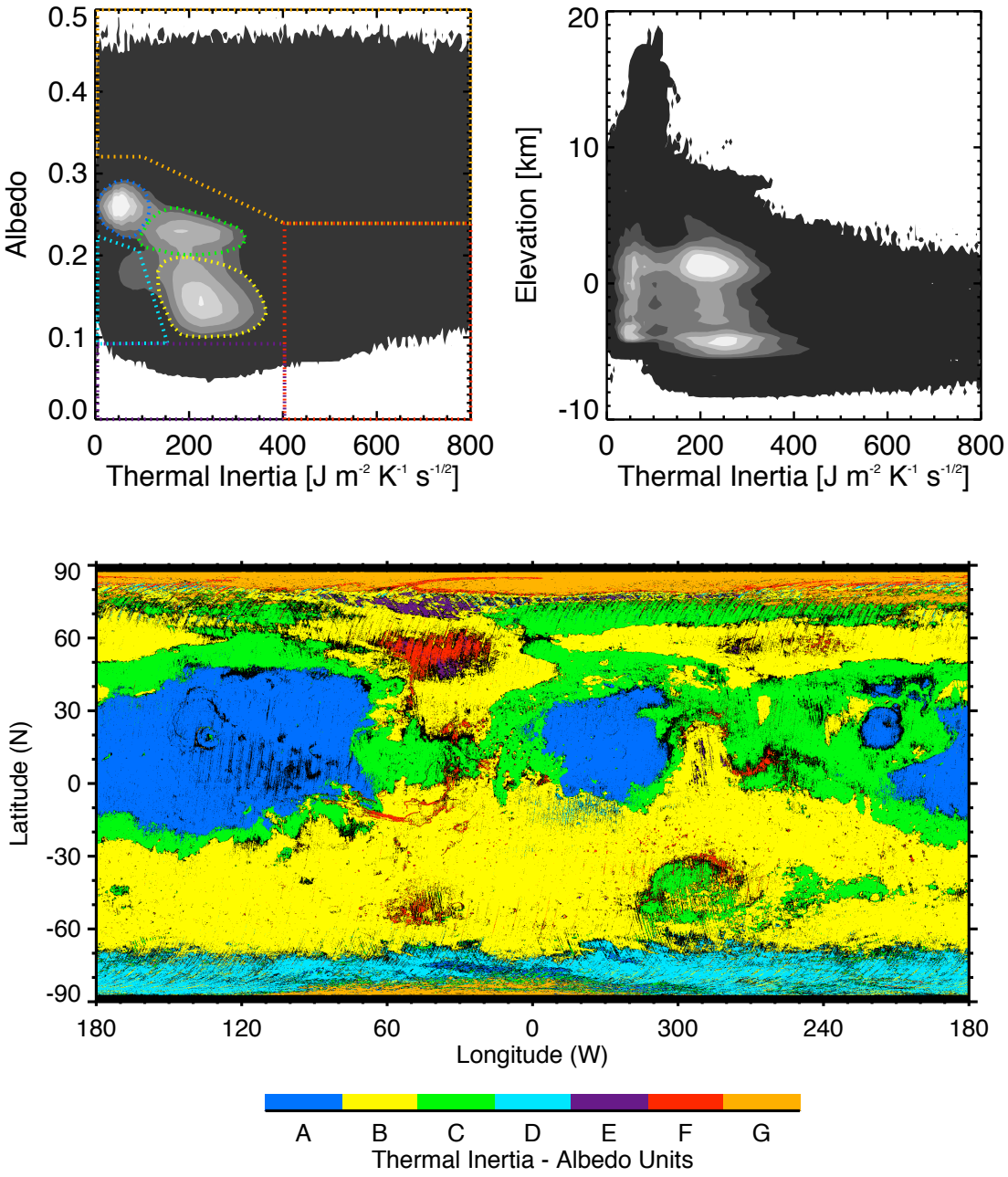

Figure A.3 Update of Figs. 2.4 (top left), 2.10 (top right), and 2.5, using the TES median map of nightside apparent thermal inertia (see Fig. 4.6) and the TES albedo map for Mars Year 26 (see Fig. 4.2). Units were redefined to correspond to new contours and to include points with high albedo and high thermal inertia within Unit G (intended to separate exposed polar ice from Unit F). Units F and G include thermal inertia up to 5000 tiu.

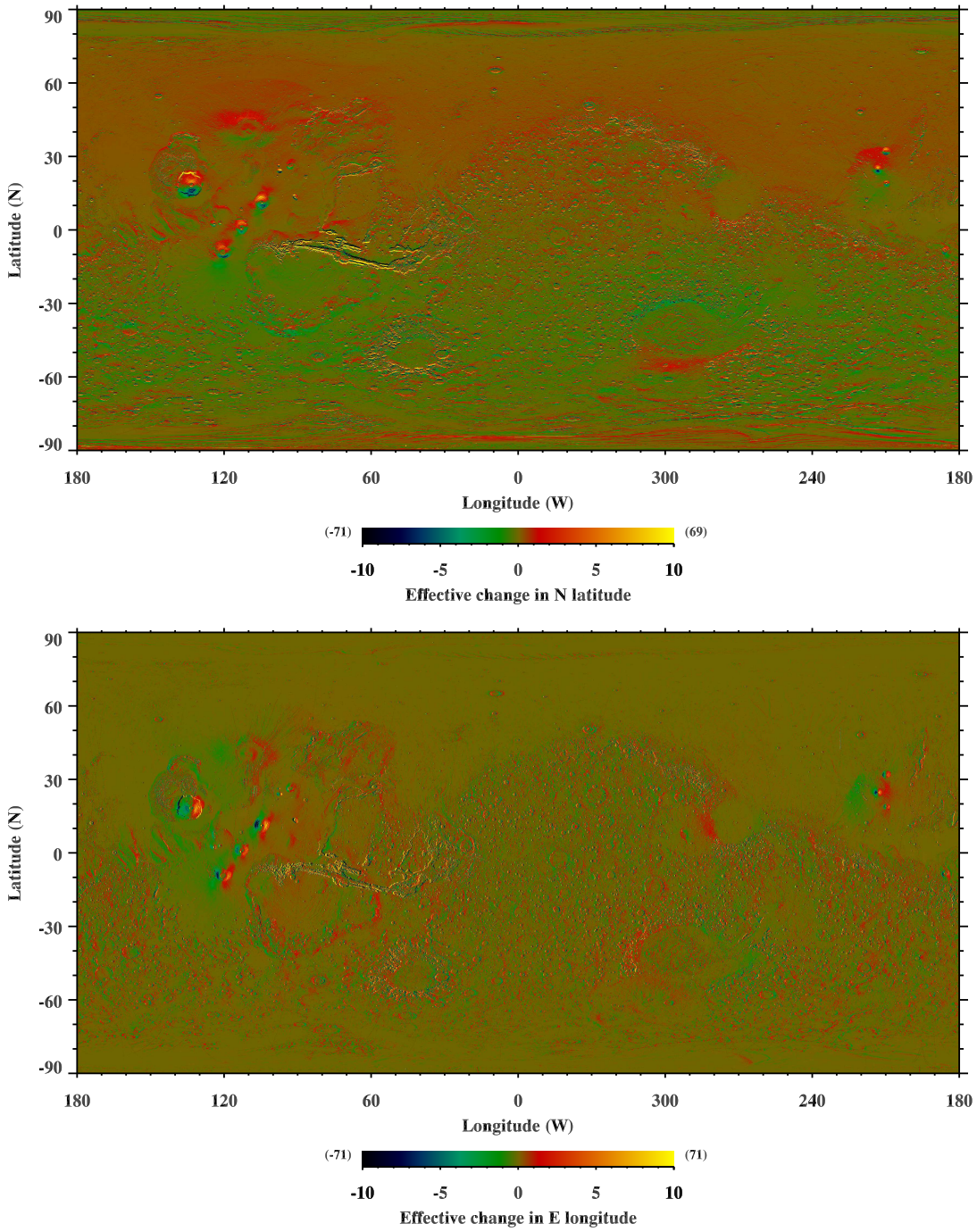

Figure A.4 Slope maps for N–S (top) and E–W (bottom) azimuths, in terms of the effective change in latitude and longitude based on MOLA radii data (see Chapter 4). Hemispherical poleward slopes are evident in the northern and southern hemispheres, and many surface topographic features seen in MOLA elevation maps (e.g., Smith et al. 2001a) are identifiable.

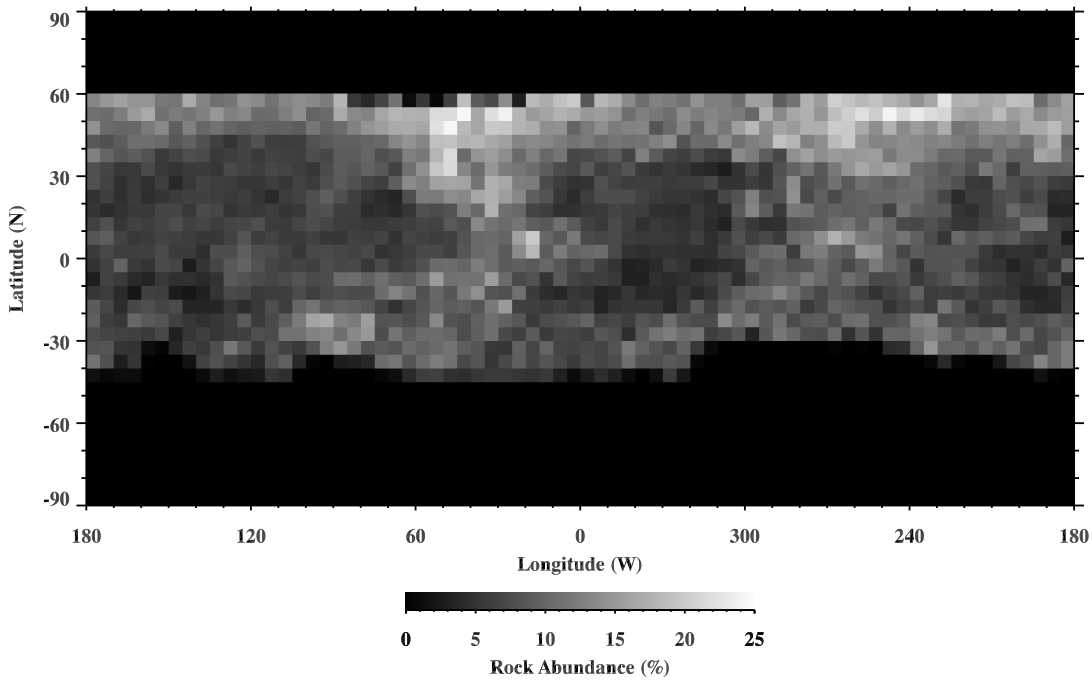

Figure A.5 Rock abundance as derived by Christensen (1986b) using a spectral differencing technique. The map has been rebinned to 5×5 degree pixels to facilitate comparison to heterogeneity maps in Figs. 4.13 and 4.14. Compare also to thermal inertia maps (Figs. 2.1 and 4.6) and the seasonal amplitude map (Fig. 4.5).